STUDY OF DYNAMICS ON THE INTERFACES OF CARBON-BASED NANOMATERIALS AND NANOBIOSENSOR

A Dissertation Presented to

the Faculty of the Department Physics

University of Houston

In Partial Fulfillment

of the Requirements for the Degree

Doctor of Philosophy

By

Jianfa Chen

August 2017

STUDY OF DYNAMICS ON THE INTERFACES OF CARBON-BASED NANOMATERIALS AND NANOBIOSENSOR

Jianfa Chen

APPROVED:

Dr. Dong Cai, Chairman
Department of Physics

Dr. Zhifeng Ren
Department of Physics and TcSUH

Dr. Gemunu Gunaratne
Department of Physics

Dr. Wu-Pei Su
Department of Physics and TcSUH

Dr. Sanghyuk Chung
Department of Biology and Biochemistry

Dean, College of Natural Sciences and Mathematics

ACKNOWLEDGEMENTS

My special thanks to Dr. Dong Cai, for his guidance and support throughout this endeavor. I feel extremely lucky of getting the chance to work with him. In the past years, I learned a lot from him.

I would like to thank Dr. Zhifeng Ren, Dr. Shuo Chen, Dr. Margaret Cheung, Dr. Gemunu Gunaratne, Dr. Wu-Pei Su, and Dr. Sanghyuk Chung for their supports in these years.

I would like to thank my current and former colleagues. Thanks to the following for sharing their valuable ideas and suggestions: Dr. Pengzhi Zhang, Dr. Naihao Lu, Dr. Zhen Yang, Dr. Guoxiong Su, Dr. Ran He, Dr. Qian Wang, Dr. Dirar Homouz, Dr. Balamurugan Desinghu, Dr. Lu Tang, Dr. Yuan Liu, Dr. Jing Shuai, Dr. Hangtian Zhu, Dr. Feng Wang, Shaowei Song, Dan Luo, Ishwar Mishra, Jun Mao, Cale Lewis, Levi Walker, and Mohammadmehdi Ezzatabadipour. I am not able to complete my doctoral degree without their companions.

I also would like to thank the supporting from Department of Physics and University of Housotn. I acknowledge the use of the Maxwell/Opuntia Cluster and the advanced support from the Center of Advanced Computing and Data Systems at the University of Houston to carry out the research presented here. This work also used the Extreme Science and Engineering Discovery Environment (XSEDE), which is supported by National Science Foundation grant.

Finally I owe my deepest gratitude to my family. Thanks for their endless encouragement and support to help me through ups and downs in my life.

Jianfa Chen

August 2017

STUDY OF DYNAMICS ON THE INTERFACES OF CARBON-BASED NANOMATERIALS AND NANOBIOSENSOR

An Abstract of a Dissertation

Presented to

the Faculty of the Department Physics

University of Houston

In Partial Fulfillment

of the Requirements for the Degree

Doctor of Philosophy

By

Jianfa Chen

August 2017

Abstract

Carbon-based nanomaterials have promising applications spanning areas from the oil industry to healthcare due to their special attributes to interface with molecules in their local environments. The investigation on nano-interfaces can open in-depth visions of chemical, physical and biological mechanisms that mediate the functions of the nanodevices designed for drug delivery and biodetection. To study properties of the surface at nanoscales poses challenges to current detection techniques, such as infrared absorption spectroscopy (IR) and transmission electron microscopy (TEM). They are either not appropriate for detecting materials in aqueous environments or lack of ability to resolve dynamics at the interface with a sufficient temporal recording rate. The computation technology fueled by the latest progress in software and hardware has shown capabilities to accurately simulate molecular binding processes in biophysics for instance. In this study, we seek the power of molecular dynamics simulation and computational docking to analyze the dynamics at various nano-interfaces including graphene amphiphilic Janus nanosheet (AJN), carbon nanotubes (CNTs), and CNT array biosensor. Rational design of the functional interface is explored by comparison of experimental results and the theoretical predictions. In the study of AJN, we discovered (1) a facile, cheap, and scalable synthesis method of AJN with graphene oxide and tapioca starch, and (2) an additive poly (sodium 4-styrenesulfonate) (PSS) that improves the stability of AJN in brine. Regarding the study of biocompatibility and biodegradation mechanism of CNTs, we found that immunoglobulin G (IgG) was susceptible to bind with CNTs that could contribute to reduce CNTs' cytotoxicity and accelerate their biodegradation. In the biorecognition study, we identified an array of phenolic oligomers with different polymerization structures could facilitate the interaction with the protein template and self-assemble to form recognition interfaces. By establishing a cascading molecular dynamics and docking analysis, a preliminary protocol of

rational design for protein imprinting was proposed and had shown an efficient screening of a chemical library. This study provides opportunities to understand molecular interactions on the interface in atomistic details, and demonstrates the combination of molecular dynamics simulation and docking is an effective approach for the development of novel nanomaterials and nanosensors.

Table of Content

Abbreviations

VDW: van der Waals

HB: hydrogen bond

CNT: carbon nanotube

SWCNT: single wall carbon nanotube

MI: molecular imprint

MIP: molecular imprint polymer

LOD: limit of detection

MD: molecular dynamics

GO: graphene oxide

AJN: graphene-based amphiphilic Janus nanosheet

SS: sodium 4-styrenesulfonate

PSS: poly (sodium 4-styrenesulfonate)

PME: Particle-Mesh Ewald

LJ: Lennard-Jones

PDB: protein data bank

EOR: Enhanced oil recovery

IgG: immunoglobulin G

BSA: bovine serum albumin

MPO: human myeloperoxidase

HRP: horseradish peroxidase

DTPA: diethylene triamine pentaacetic acid

SOZ: serum-opsonized zymosan

TEM: Transmission electron microscopy

CD: circular dichroism

fMer: functional monomer

pfMer: protein functional monomer

PPn: polyphenol

HPV: human papillomavirus

E7: human ferritin E7 biomarker protein

OLS: *4*-Phenoxyphenol

OSE: *2*-Phenoxyphenol

OET: *3*-Phenoxyphenol

hFtn: human ferritin

EIS: electrochemical impedance spectroscopy

DPV: differential pulse voltammetry

RMSF: Root-mean-squared fluctuation

List of Accomplishments

1. **Chen, J.**, Lewis, C., Balamurugan, D., Yang, Z., Ai, L., & Cai, D. (2016). Theoretical analysis of a high performance protein imprint on a nanosensor. *Sensing and Bio-Sensing Research*, *7*, 12-19.

2. Ding, Y., Tian, R., Yang, Z., **Chen, J.**, & Lu, N. (2016). Binding of human IgG to single-walled carbon nanotubes accelerated myeloperoxidase-mediated degradation in activated neutrophils. Biophysical Chemistry, 218, 36-41.

3. Ding, Y., Tian, R., Yang, Z., **Chen, J.**, & Lu, N. (2017). Effects of serum albumin on the degradation and cytotoxicity of single-walled carbon nanotubes. Biophysical chemistry, 222, 1-6.

4. Ding, Y., Tian, R., Yang, Z., **Chen, J.**, & Lu, N. (2017). NADPH oxidase-dependent degradation of single-walled carbon nanotubes in macrophages. Journal of Materials Science: Materials in Medicine, 28(1), 7.

5. Yang, Z., **Chen, J.**, Willson, R. C., Cai, D., Ren, Z., Improved detection performance by artificially enhanced interface formation in electropolymerized protein imprints (submitted).

6. Luo, D., **Chen, J.**,Wang, F., Wang, D., Willson, R. C., Cai, D., Ren, Z., Stabilization of amphiphilic Janus nanosheets in relatively high salt water with retained inferfacial behavior: experimental and MD study (submitted).

7. Luo, D., Wang, F., Vu, B., **Chen, J.**, Bao, J., Cai, D., Willson, R. C., Ren, Z., Synthesis of graphene-based amphiphilic Janus nanosheet via manipulation of hydrogen bonding (submitted).

8. **Chen, J.**, Lewis, C., Balamurugan, D., Cai, D., A computational study towards the rational design of protein recognition, Affinity 2015, 21st biennial metting of international society for molecular recognition, poster.

Chapter 1 Introduction

1.1 Molecular interactions

Molecular interactions are the attractive and repulsive interactions between two molecules that are not being connected by covalent bonds. Molecular interactions are also known as intermolecular interactions or non-covalent interactions. Compared to covalent interactions, which are on the order of 100 kcal/mol, molecular interactions are much weaker (1-10 kcal/mol); however, they play an essential role in almost all fields, including material sciences, protein folding, protein association, drug design, crystallization, sensor, disease diagnosis, etc. Take H_2O molecules as an example, the bonds between oxygen and hydrogen are covalent (solid lines in Figure 1.1A). It's the molecular interactions that determine which state it will be: water, ice, or steam. Molecular interactions are critical in maintaining the three-dimensional structure of large molecules, such as protein (Figure 1.1B).

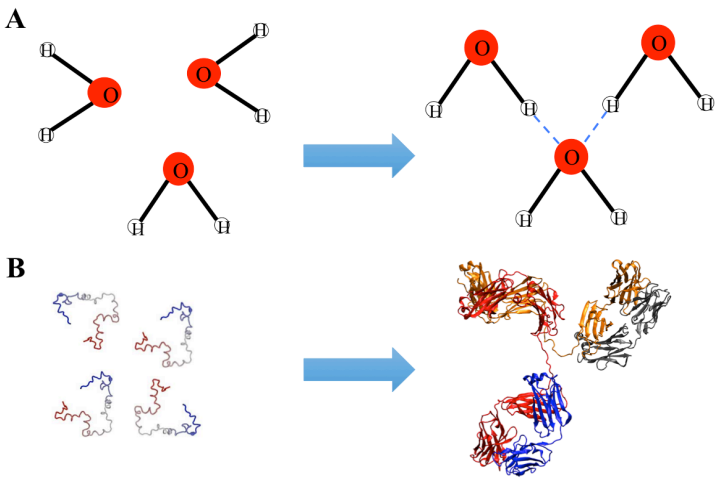

Figure 1.1 Illustration of molecular interactions.
(A) Molecular interactions between H_2O molecules determine which state it is: ice, water, or steam. (B) Molecular interactions determine the three-dimensional structure of proteins. This protein consists of 4 independent chains.

Molecular interactions can be categorized as van der Waals interactions (VDW), electrostatic interactions, hydrogen bonds, and hydrophobic effects.

1.1.1 Van der Waals interaction

Van der Waals interactions are named after Dutch scientist Johannes Diderik van der Waals. Van der Waals interactions arise from the interaction between uncharged atoms, including attraction and repulsion, and they are distance dependent. There are four major contributions to the van der Waals interactions: repulsive interaction, permanent-permanent dipoles interaction (Keesom interaction), permanent-induced dipoles interaction (Debye force), and induced dipole-induced dipoles interaction (London dispersion force). The Lennard-Jones potential is a reasonable approximation for the van der Waals interaction (Figure 1.2).

$$V_{LJ} = 4\varepsilon\left[\left(\frac{\sigma}{r}\right)^{12} - \left(\frac{\sigma}{r}\right)^{6}\right] = \varepsilon\left[\left(\frac{r_m}{r}\right)^{12} - 2\left(\frac{r_m}{r}\right)^{6}\right]$$

Where ε is the depth of the potential well, σ is the finite distance at which the inter-particle potential is 0, r is the distance between the particles, and r_m is the distance at which the potential reaches its minimum.

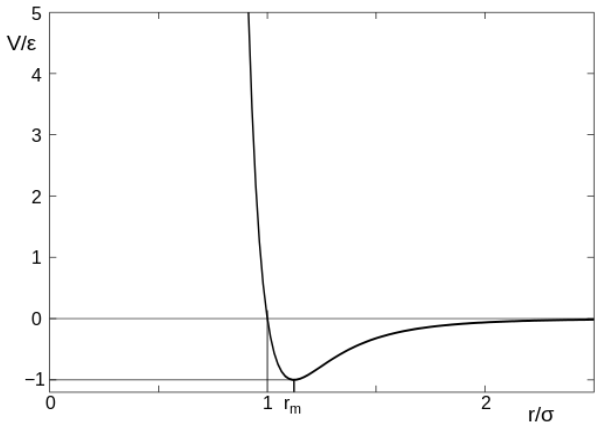

Figure 1.2 Schematics of Lennard-Jones potential.
ε is the depth of the potential well, σ is the finite distance at which the inter-particle potential is 0, r is the distance between the particles, and r_m is the distance at which the potential reaches its minimum.

1.1.2 Electrostatic interaction

Electrostatic interactions are forces between two charged particles. They can be either attractive or repulsive depending on the signs of the charges. The strength of electrostatic interactions can be computed from the Coulomb's law.

$$V_{elec} = \frac{q_i q_j}{4\pi\varepsilon r_{ij}}$$

Where q_i and q_j is the charge on particle i and particle j, respectively. ε is permittivity, and r_{ij} is the distance between particle i and particle j.

1.1.3 Hydrogen bond

Hydrogen bonds (H-bond) are strong electrostatic dipole-dipole interactions, which only have the attractive force between the lone pair of an electronegative atom and a hydrogen atom that is bonded to O, S, N, or Cl (Figure 1.3).

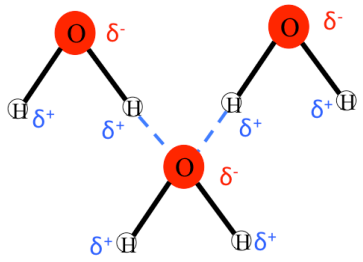

Figure 1.3 Schematics of hydrogen bonds (blue dashed lines) between water molecules.

1.1.4 Hydrophobic effect

The hydrophobic effect is the insolubility of non-polar substance in water. The entropy of the system drives the aggregation of non-polar molecules. It increases when the surface area of

nonpolar molecules to the polar water is minimized. This effect plays a critical role in the folding of large molecules and protein recognition.

1.2 Molecular interface

Molecular interface is the region where molecular contact and molecule interactions take place. In chemical and material science, interfaces have been recognized as a critical part for more than a century. Since the days of J.W. Gibbs, a physical chemist who created statistical mechanics and used it to explain the laws of thermodynamics, researchers have tried to explain the interesting phenomena that happened when different phases met. The interfacial tension has been well explained by the greater attraction of liquid molecules to each other than to the molecules in the air. As shown in Figure 1.4, the net force is zero for the molecule in the bulk of water as each molecule is pulled equally in every direction; however, molecules on the surface don't have the same attraction in all directions, resulting in a non-zero net force.

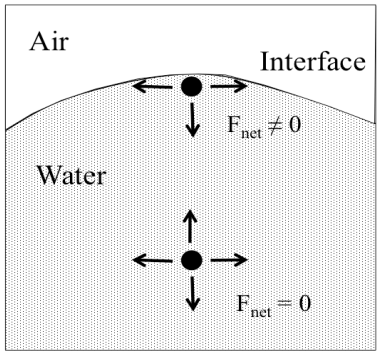

Figure 1.4 Schematics of air-water interfacial tension.
The net force is zero for the molecule in the bulk of water as each molecule is pulled equally in every direction; however, molecules on the surface don't have the same attraction in all directions, resulting in a non-zero net force.

Biomolecule interface has attracted lots of attentions in recent decades. Many biomolecule phenomena, including protein recognition, protein folding, and enzyme catalysis,

cannot be actually understood without dealing with interfacial behavior. It's essential to figure out how biomolecule behavior is affected by the structuring of their interfaces. The probing and modeling biomolecule interface also have a large impact on the development of drug/ligand design.

Water is known to be the matrix of life, and all metabolisms, signal processing, and other biological reactions happen in this matrix. The existence of water has a large impact on the surface of a protein. Water molecules surround the protein, forming a solvation shell, also named as hydration shell (Figure 1.5). The hydration layer around a protein has been found to have dynamics distinct from the bulk water to a distance of 1 nm [1]. The interactions between protein and the hydration layer change the surface property and binding dynamics significantly. Epistructure, the surface structure with hydration layer, is fundamental to the activity of proteins [1].

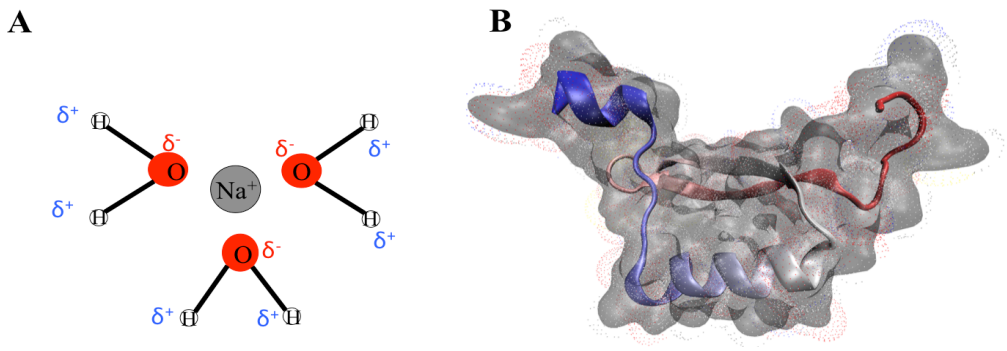

Figure 1.5 Schematics of solvation shell for ions (A) and protein (B).

Molecular interface is not merely the sum of all intermolecular interactions. The natural binding process of protein reminds us of the importance of cooperativity in the assembly of protein structures. Cooperativity is the concurrent participation of different region of the biomolecule to promote and sustain intramolecular or intermolecular interactions [2]. The cooperativity results in an additional contribution to the protein interaction. In other words, the

whole is more than the sum of the parts. For example, the association between an antibody and an antigen is a cooperativity of a myriad of non-covalent interactions between the epitopes – the binding site on the antigen, and the paratopes – the binding site on the antibody [3].

Improving the binding specificity and reducing the side effects are the major imperative in drug design. Drug-based inhibition of target protein's activity may have at least two folds of side effects: (1) the drug may interfere with pathways other than the one of therapeutic relevance because of the manifold roles of the target protein; (2) structurally similar proteins may alternatively associate with the inhibitor [2]. Mastering epistructural targeting of the protein is an imperative to achieve drug specificity [2].

Improving the binding specificity is to exploit characteristics of protein-ligand interactions that are not preserved across paralogs, despite the similarity in structures [4-6]. Many research have been reported to clarify the protein-ligand interactions in recent decades [7]. Various computational methods are provided to predict the protein-ligand interactions, such as free energy analysis [8], docking [9], assessment of packing defects [10], analysis of protein interface geometry [11], molecular dynamics simulation [12], and sequence threading [13].

1.3 Current study methods on the molecular interface

The ability to obtain a molecular-level understanding of the interactions on the molecular interfaces is critical to the development and improvement of many chemical and biological systems [14]. A deep understanding of the molecular interfaces would have a great impact on many fields, such as crude oil recovery, environmental protection, healthcare, material science, and drug design.

Investigating the molecular interfaces at a molecular level is a challenge. The size of molecular interface is much smaller than the size of two involved bulks. The detection of the

interaction at the interface is hampered by the need to distinguish the few atoms at the interface with those in the bulk. A number of detection techniques have been developed in recent decades to overcome this obstacle (Table 1.1), from infrared absorption spectroscopy (IR) to transmission electron microscopy (TEM). Most of the techniques are based on light or other electromagnetic radiation for surface analysis because of less influence by condensed matter [15].

Table 1.1 Experimental techniques for molecular interface investigation.

Detection techniques	Methods	Reference
Infrared absorption spectroscopy (IR)	Attenuated total reflectance (ATR)	[16]
	Reflection-absorption infrared spectroscopy (RAIRS)	[17]
	Transmission	[18]
Other vibrational spectroscopies	Raman scattering spectroscopy	[19]
	Sum frequency generation	[20]
Other UV-vis and acoustic techniques	UV-vis absorption spectroscopy	[21]
	Fluorescence emission spectroscopy	[22]
	Second harmonic generation (SHG)	[23]
	Surface plasmon resonance (SPR)	[24]
	Ellipsometry	[25]
	Quartz crystal microbalance (QCM)	[26]
X-ray and neutron-based techniques	X-ray absorption (XAS) and emission (XES) spectroscopies	[27]
	X-ray reflectivity and scattering	[28]
	X-ray diffraction	[29]
	Neutron scattering and diffraction	[30]

Table 1.1 Experimental techniques for molecular interface investigation (continue).

Detection techniques	Methods	Reference
Other spectroscopies	X-ray photoelectron spectroscopy (XPS)	[31]
	Nuclear magnetic resonance (NMR)	[32]
	Electron spin resonance (ESR, EPR)	[33, 34]
Microscopies - optical	Fluorescence microscopies	[35]
	Raman microscopy	[36]
	Nonlinear optical microscopies	[37]
	Infrared and X-ray microscopies	[38]
Microscopies - scanning	Scanning tunneling microscopy (STM)	[39]
	Scanning electrochemical microscopy (SECM)	[40]
	Atomic force microscopy (AFM)	[41]
Microscopies – optical scanning	Scanning near-field optical microscopy (SNOM)	[42]
Microscopies - electron	Scanning electron microscopy (SEM)	[43]
	Transmission electron microscopy (TEM)	[44]

There are two major deficiencies of the experimental techniques in the investigation of molecular interface: (1) many of these techniques rely on the use of particles, such as electrons, ions, or atoms, which work best under a vacuum environment and are not appropriate for aqueous environments [15]; (2) most techniques can only investigate the interface in bonded state, and lack the ability to monitor the binding dynamics at the interface at atomic level.

As an important complement to the interface research, various computational methods are provided to predict the protein-ligand interactions and binding dynamics, such as free energy analysis [8], docking [9], assessment of packing defects [10], analysis of protein interface geometry [11], molecular dynamics simulation [12], and sequence threading [13]. The first four computational methods depend on the surface property of target protein, and the last one merely relies on the sequence information. Docking and molecular dynamics simulation methods are the most widely used method because of their efficiency and accuracy. The comparison between experimental and theoretical results on interface plays a crucial role in the process of understanding molecular interfaces.

Even though many efforts have been made in this field, the prediction of interface remains a challenge. Only a few study have been implemented to predict the interface of carbon-based nanomaterials and nanosensor. Here we combined computational docking and molelcular dynamics simulation with experimental methods to investigate the dynamics on the interface of carbon based nanomaterials and biosensor.

1.4 Carbon-based nanomaterials

Carbon is the fundamental element of all kinds of living organisms on Earth and is abundant on Earth. It has four valence electrons and relatively small size, which make it flexible to bind with other elements, especially oxygen, hydrogen, and nitrogen. Carbon's unique diversity of forming complex organic molecules led the formation of the first living organism on earth, which evolves into human beings after 4.2 billions of years. All of us, who live on Earth, are carbon-based beings.

Carbon atoms can bond together in many different ways, termed allotropes of carbon. The best known of them are graphite, diamond, and amorphous carbon. In recent decades,

tremendous progress in the material science led to many fascinating findings. In 1985, a team of scientists from Rice University and the University of Sussex discovered a new allotropic form, which is named buckminsterfullerene (C_{60}) [45]. Three of them, Robert Curl Jr., Harold Kroto, and Richard Smalley, were awarded the Nobel Prize in Chemistry in 1996. Later carbon nanotubes (CNTs) were first evidenced by Sumio Iijima in 1991[46]. Followed by Andre Geim and Konstantin Novoselov at the University of Manchester first isolated and characterized graphene in 2004 [47]. They won the Nobel Prize in Physics in 2010 because of this work.

These findings promoted the development of nanotechnology, which has been a hot topic in the past decades. The development of nanotechnology profoundly impacts the electronic industry, battery industry, photovoltaic industry, pharmacy industry, and chemical industry. Everyone benefits from nanomaterial, especially carbon-based nanomaterial. We can achieve more by connecting nanotechnology with biology. Nanomaterial has received considerable attention, because their sizes are comparable to biological molecules, such as DNA, RNA, and protein. Nanomaterial can interplay with single molecule, which implies an attractive prospect: diseases can be diagnosed and treated at molecule level. If every molecule in the cell can be controlled, then whole living beings are under control too. According to the size and shape, nanomaterial can be categorized as nanotube, nanorod, nanowire, nanoparticle, and thin film.

Graphene and carbon nanotubes (CNTs) are the most widely investigated carbon-based nanomaterials in the past decade. Graphene can be thought of as a single layer of graphite, and CNTs can be thought of as the seamless hollow tubes composed of rolling graphite sheet. CNTs can be divided into single-walled carbon nanotubes (SWCNTs) and multi-walled carbon nanotubes (MWCNTs) according to the number of graphite layers.

Graphene is a robust and flexible two-dimension membrane with many exciting properties. It has a large specific surface area (263 m^2g^{-1}) [48], and high Young's modulus(~ 1.0 TPa) [49]. The unique properties make graphene a great platform for the modification or

functionalization of the carbon backbone. Graphene oxide (GO) can be produced on the tone scale at a low cost [50], and is widely used as a precursor for the production of graphene-based material [51]. Graphene oxide is a good surfactant material stabilizing emulsion systems because of its unique surface properties [52]. Both sides of graphene oxide surface are hydrophilic. It is possible to modify the surface properties by functionalizing the carbon backbone [53].

Recently Luo et al. (2016) reported a simple nanofluid of graphene-based amphiphilic Janus nanosheets (AJN) by functionalizing one surface of graphene oxide with alkylamines [53]. The AJN can enhance oil recovery with an efficiency of 15.2%, which means massive amounts of oil can be recovered every year.

CNTs can serve as a drug-delivering vehicle for cancer treatment: the hollow structure is suitable for drug loading, and the large surface is easy to be modified for solubility and targeting ability [54]. Cancer is one of the most challenging problems we face in the 21st century. Currently, the primary treatments for cancer are surgery, radiation therapy, and chemotherapy. All of these treatments are painful and kill healthy cells at the same time. CNTs have the potential to serve as drug delivery vehicles that target specific cancer cells. The targeted delivery drug can efficiently kill cancer cells without damaging healthy cells. However, CNTs are difficult to be degraded because of chemical stability. The accumulation of CNTs would enhance the cytotoxicity. Biopersistence of CNTs is one of the major stumbling blocks on the way of CNTs' broad biomedical applications. We found that CNT would bind with various proteins in vivo, especially IgG. The binding of IgG reduces CNTs' cytotoxicity and accelerates biodegradation of CNTs.

Beyond serving as a drug-delivering vehicle, CNTs are also perfect material as an electrode because of its high chemical stability, high electrical conductivity, and fast heterogeneous charge transfer. Compared to other electrodes, CNT electrodes have several

benefits: high sensitivity, small overpotential, and low resistance, and exhibit a lower limit of detection (LOD).

The excellent properties of CNTs are attributed to the curvature of the carbon graphene sheet in the nanotube. As shown in Figure 1.6, the surface electrons are uniformly distributed on both sides of C-C backbone in graphene; however, the uniformly distributed electron clouds are distorted in carbon nanotube because of the curvature surface. Many more π-electrons conjugate on the outside surface rather than inside, which makes carbon nanotube electrochemically active [55].

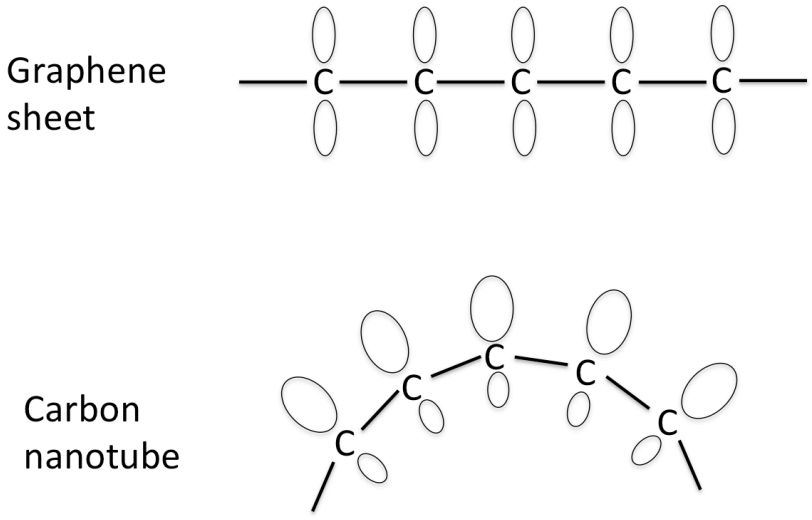

Figure 1.6 Schematic diagram of the surface-electron distribution along a graphene sheet and a carbon nanotube (CNT).
For graphene sheet, the surface electrons are uniformly distributed on both sides of the C-C backbone. The uniformly distributed electron clouds are distorted in carbon nanotube because of the curvature surface. Much more π-electrons conjugate in the outside surface than inside, which makes carbon nanotube electrochemically active.

Compton and his colleagues performed an experiment to address the question why CNTs possess such unique catalytic properties [56]. Their experiments suggest that edge plane-like sites, which in CNTs occur at the ends and along the tube axis, are responsible for the fast

heterogeneous charge transfer. It also explains why CNTs have been widely reported as "electrocatalytic". According to Compton's research, bamboo-like CNTs and herringbone CNTs have faster heterogeneous charge transfer than hollow tube CNTs, because they have a higher proportion of edge plane sites [57]. The schematic diagram is shown in Figure 1.7.

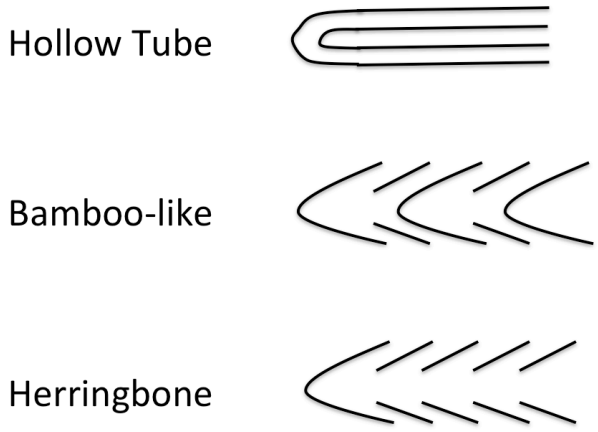

Figure 1.7 Schematic diagram of three different structured carbon nanotube. In both the bamboo-like and herringbone CNTs, graphene plane has an angle to the axis of the tube, and more edge plane sites are on the surface; therefore, they have faster heterogeneous charge transfer than hollow tube CNTs.

1.5 Electrochemical biosensor

A biosensor is a device that detects biochemical compounds by electrical, thermal, or optical signals. Those who rely on electrochemical redox reaction and detect the signals by electrical properties, namely current (I), potential (V), or resistance (R), are called electrochemical biosensors. The advantage of electrochemical biosensor over the others is (1) its ability to monitor localized events taking place at the interface between sensing surface and the living system under investigation, (2) its ability to collect continuous, on-line information, and monitor the whole reaction process.

An electrochemical biosensor consists of three parts: (1) recognition element, which recognizes analyte, (2) electrode (so-called transducer), which translates the recognition information into appropriate electrical signals: potential, current, or impedance, (3) electrochemical workstation that measures electrochemical signals, and supply reaction driving potentials or currents, and display recording charts. Figure 1.8 shows the schematic diagram of principal components of an electrochemical biosensor with immunorecognition enhanced specificity.

Analytes are the target chemical or biochemical compounds whose concentration we are interested in quantitatively monitoring. Usually, analytes that are detected by electrochemical biosensors either take part in a catalyzed-redox reaction (catalytic biosensors) or inhibit a redox reaction (inhibition biosensors), which results in an electrical signal.

The recognition process is implemented by the host-guest interaction, where the host is the recognition component in biosensor and guest is the analyte. The most common-use recognition element is enzyme, antibody, and mimic antibody. The dominant interaction of the host-guest interaction can be hydrogen bond, electrostatic interaction, hydrophobic interaction, or any combination.

The recognition event happening in the recognition element is translated into an appropriate signal through a transducer. The signal must be an electrical signal for electrochemical biosensor. Currently, potential (V) and resistance (R) are the main parameters for decoding the recognition stimulus, because usually the amplitude of current (I) is very small. Based on the measured parameters, electrochemical biosensors are categorized as potentiometric, impedometric, and amperometric.

Two main factors determine the limit of detection (LOD) of a biosensor: (1) the specific recognition ability of recognition element, and (2) the efficiency of translating recognition stimulus into a measurable signal. Carbon nanotubes (CNT) possess high mechanical strength,

high chemical stability, high electrical conductivity, and fast heterogeneous charge transfer, which make it an excellent transducer for biosensors.

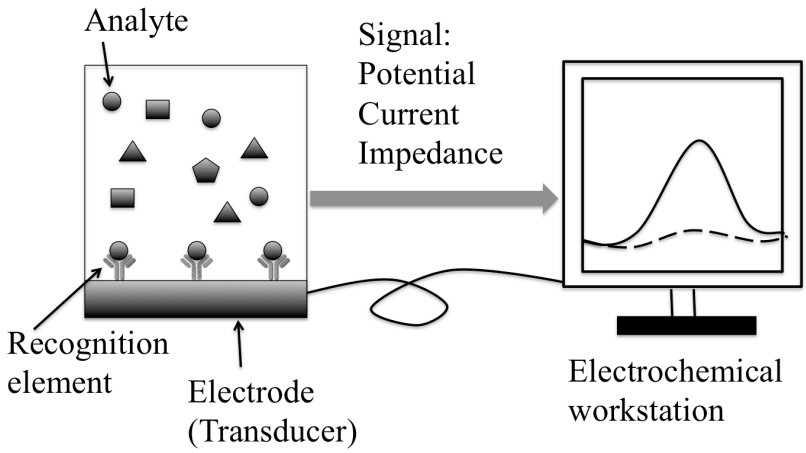

Figure 1.8 Schematic diagram of electrochemical biosensor.
An electrochemical biosensor consists of three parts: (1) recognition element, which recognizes analyte; (2) Electrode (so-called transducer), which translates the recognition information into electrical signal: potential, current, or impedance; (3) electrochemical workstation that measure electrochemical signals, and supply reaction driving potentials or currents, and display recording charts.

1.6 Molecular imprint polymer (MIP)

As we mentioned in the previous section, the limit of detection (LOD) of a biosensor is restricted by two primary factors: (1) the specific recognition ability of recognition element, and (2) the efficiency of translating recognition stimulus into a measurable signal. The traditional recognition elements are natural biomolecules, such as antibodies, enzymes, and DNA [58-60]; however, there are many limits in the application of these recognition elements due to their biological origin. Most antibodies and enzymes denature at 40 ^{o}C. Every biomolecule requires a particular operational environment (pH, temperature, ions concentration, and substrate) to keep recognition ability [61]. In addition to the instability, biomolecules are expensive and difficult to

prepare. Synthetic recognition receptor, therefore, is a promising alternative for the use of biomolecules [62]. The most generic and cost-effective technology for biomimic receptors is molecular imprinting (MI) [63].

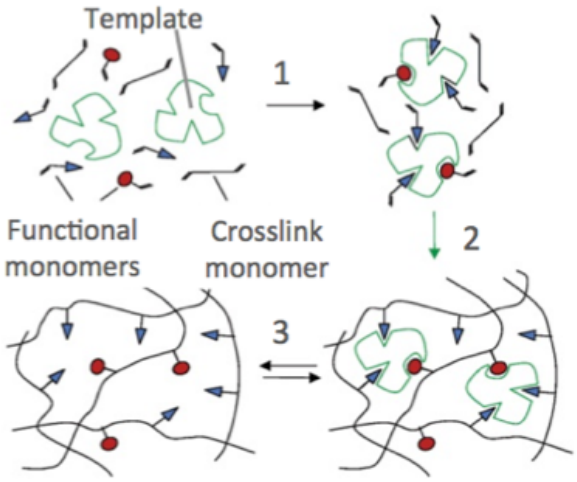

Figure 1.9 Molecular imprint (MI) fabrication and molecular recognition. The template molecule forms a complex with the functional monomers (Step 1), is trapped by polymerized crosslink monomers (Step 2), and then is removed from the scaffold. The functional monomers, which are complexed into the polymerized "mold," are now ready for specific rebinding with a template target (Step 3).

Molecular-imprinting technology can be utilized to produce the molecular "mold", i.e. the imprint, by using a target molecule as the template during the polymerization of scaffold monomers [64]. Thanks to the pre-complexation between the functional monomer and the template, the pocket-like imprint cavity can carry out not only morphological matching but also physicochemical coupling with the target molecule (Figure 1.9). It can recognize small molecule targets for chemical detection, purification, and separation [65].

Compared to biomolecules, molecular imprint polymer (MIP) based biosensors have many merits, such as stability, cost-efficiency, ease of operation, etc. The comparison of natural biomolecules and MIP is listed in Table 1.2.

Table 1.2 Comparison of natural biomolecules used in sensors and MIPs [61]

Natural biomolecules	MIPs
Unstable	Stable to a large range of pH and temperature
Expensive	Cheap
Require unique operational environment	Adaptive to different operational environment
Available for limited analytes	Can be prepared for any analyte

The research related to molecular imprint polymer (MIP) is blooming since 1991 (Figure 1.10); however, the design and synthesis methods of imprinting are unsatisfactory when the templates are macromolecules. Even though more than 1,000 papers were published related to MIP in 2016 (Figure 1.10), only 56 articles focus on protein imprinting (Figure 1.11).

In the case of biomarker proteins, the prediction of pre-complexation has to consider the interaction interface formed after the protein structural folding. The interaction with the interface is evaluated to screen for the appropriate functional monomers out of chemical databases. The multitude polymer compounds, protein surface groups, and structural variables have to be examined. It makes computational tools indispensable. The available software, servers, and databases enable us to unprecedentedly conduct quantitative prediction of the interface, binding energy, optimal functional monomer, and appropriate polymerization chemistry, for designing the imprinting.

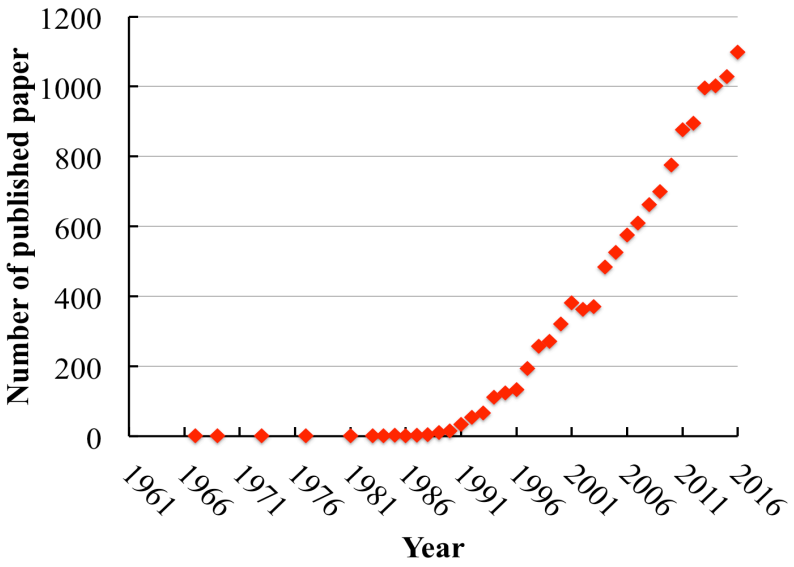

Figure 1.10 Number of published paper related to molecular imprinting technology from 1961 to 2016.
Query result from the web of knowledge with key word "molecule imprint" or "molecular imprint".

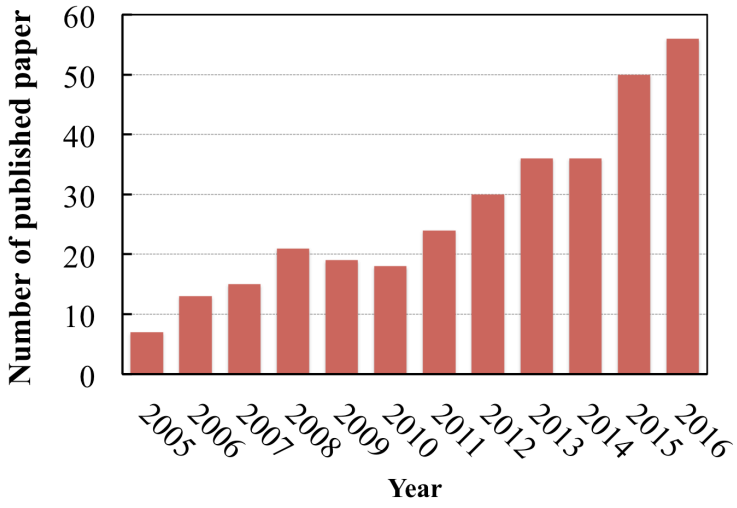

Figure 1.11 Number of published paper in protein imprinting from 2005 to 2016.

Protein biomarkers disseminated by cancer cells can be used for early diagnosis of cancers. The detection relies on biomarker recognition primarily provided by antibodies. At the early stage of cancer, the biomarkers have extremely low concentrations in biological samples [66], at which the biorecognition becomes incapable to capture the biomarker targets. A higher affinity of the antibody to the corresponding biomarker is required [67]. In fact, the highest binding affinity among all discovered natural binding moieties is discovered in the interaction between biotin-avidin [68]. The avidin as the biotin receptor offers a deep pocket that matches the biotin molecule. The physical confinement and the physiochemical interaction support the binding and underlie the mechanism of the most robust biorecognition. We propose to mimic the avidin structure to design with computational assistant and fabricate a polymeric biorecognition to provide binding affinity with the biomarker superior to the existing binding moieties. It can, therefore, facilitate early cancer detection.

1.7 Computational methods

1.7.1 Molecular dynamics simulation (MD)

As we mentioned in previous sections, the mode of physical movement and interactions between two molecules, which is an N-body problem, is essential for the design of novel material and biosensor. Molecular dynamics (MD) simulation is a universal computational method for N-body simulation. It was first developed for theoretical physics in 1959 [69], and soon expended to the other fields, such as chemical physics, materials science, and biology.

For an N-body problem with $N > 3$, it's impossible to get an analytical solution. Molecular dynamics simulation approximates the solution by using numerical methods. It's widely used to understand and predict the properties of target molecules on an atomic scale. According to statistical mechanics, the experimental values of physical quantities (macroscopic

properties) are ensemble average over a representative statistical ensemble for both equilibrium systems and non-equilibrium systems. For the generation of a representative equilibrium ensemble, both molecular dynamics simulation and Monte Carlo simulation are available; however, for the generation of a representative of a non-equilibrium ensemble, only the MD simulation is appropriate.

MD simulation solves Newton's equations of motion for a system of N interacting atoms:

$$m_i \frac{\partial^2 r_i}{\partial t^2} = F_i, i = 1, 2, \cdots, N$$

The forces are the negative derivatives of a potential function V(r_1, r_2, $\cdots$,r_N):

$$F_i = -\frac{\partial V}{\partial r_i}$$

Where the potential function V is computed from the inter-atoms potential in a specific force field.

Usually, the size of the simulated system is much smaller than the one in the real world because of the computation ability. Periodic boundary conditions (PBC) are applied to approximate an infinite system from a small system. As shown in Figure 1.12, the central box is the simulated system and particles in solid black are real particles. The other boxes are virtual boxes and the dashed gray particles are virtual particles. Each particle interacts not only with every other particle in the system but also with all other particles in the copies of the system. The arrows show the interaction between a real particle and the nearest copies of the other particles in the system.

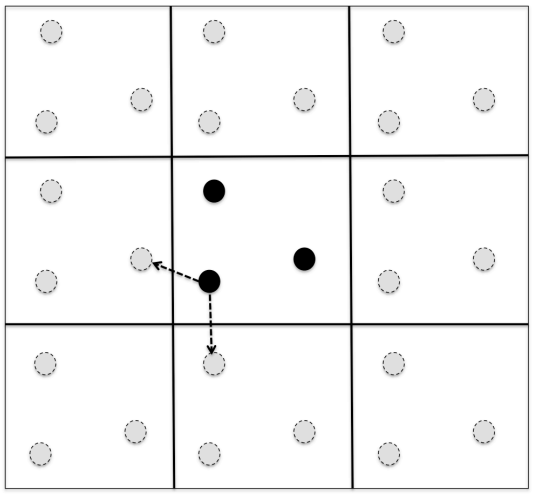

Figure 1.12 Schematics of periodic boundary conditions for molecular dynamics. The central box is the simulated system and particles in solid black are real particles. The other boxes are virtual boxes and the dashed gray particles are virtual particles. Each particle interacts not only with every other particle in the system but also with all other particles in the copies of the system. The arrows show the interaction between the real particle and the nearest copies of the other particles in the system.

The equations are solved simultaneously in small time steps to make the approximation accurate. The system also takes care that temperature and pressure remain at the required values. Information of atoms, such as velocities and coordinates, are recorded at regular intervals. The coordinates as a function of time represent a trajectory of the system. After initial changes, the system will usually reach an equilibrium state. By averaging over an equilibrium trajectory, for systems which obey ergodic hypothesis, many macroscopic properties can be extracted from the recorded information [70].

After fifty-years development, there are many excellent engine softwares, such as GROMACS [71], NAMD [72], AMBER [73], CHARMM [74], GROMOS [75], and many force fields, such as OPLS force fields [76], AMBER force fields [77], CHARMM force fields [78], GROMOS force fields [79], are available for molecular dynamics simulation. Among them,

GROMACS and NAMD are the most widely used software for MD simulation, and GROMACS has the highest computational efficiency.

1.7.2 Computational docking

Docking is another computational method used to predict the preferred orientation and binding site of one molecule to another [80]. The docking problem can be thought as a "lock-and-key" fitting problem, as Figure 1.13 shown. Targeted protein is the rigid "lock" and ligand is the flexible "key". "Key" is initially placed randomly in a place far away from the "lock" and search for the best binding site and orientation under an algorithm. If we dock several "keys" to the same "lock", some of them must be more likely to open the "lock" than the others. Binding affinity is used to calibrate the ability for a "key" to open a "lock". The predicted binding affinity and the consistency of results are combined to identify the best binding.

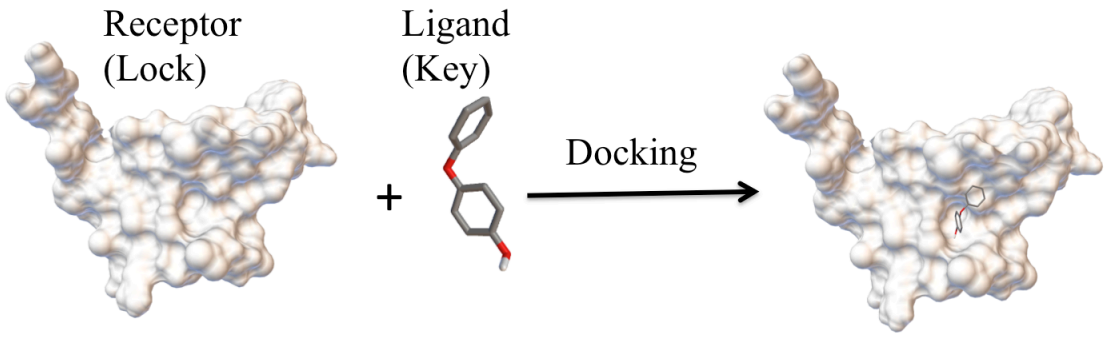

Figure 1.13 Schematics of protein-ligand docking.
"Key" is initially placed randomly in a place far away from the "lock" and search for the best binding site and orientation under an algorithm. If we dock several "keys" to the same "lock", some of them must be more likely to open the "lock" than the others. Binding affinity is used to calibrate the ability for a "key" to open a "lock". The best binding pose has the largest binding affinity.

Compared to molecular dynamics simulation, docking has a much higher efficiency in predicting the binding site and orientation with the penalty of accuracy. The large receptor is treated as a rigid body, and its position is fixed. The computing of interactions between receptor

and ligand is also simplified. The high efficiency of docking makes it an attractive method for screening a library of candidates in rational design.

There are many protein-ligand docking software available and free on line, such as AutoDock [81], AutoDock Vina [82], AADS [83], BetaDock [84], etc. Among them, AutoDock is the most cited docking software, and AutoDock Vina is the improved version of AutoDock.

The binding affinity of AutoDock includes six pair-wise evaluated potential (V) and an estimate of the conformational entropy loss upon binding (ΔS_{conf}):

$$\Delta G = \left(V_{bound}^{L-L} - V_{unbound}^{L-L}\right) + \left(V_{bound}^{P-P} - V_{unbound}^{P-P}\right) + \left(V_{bound}^{P-L} - V_{unbound}^{P-L} + \Delta S_{conf}\right)$$

Where L refers to the ligand and P refers to the protein.

Each of the evaluated potential V includes van der Waals interaction, hydrogen bonding, electrostatics, and desolvation.

$$V = W_{vds}\sum_{i,j}\left(\frac{A_{ij}}{r_{ij}^{12}} - \frac{B_{ij}}{r_{ij}^{6}}\right) + W_{hbond}\sum_{i,j}E(t)\left(\frac{C_{ij}}{r_{ij}^{12}} - \frac{D_{ij}}{r_{ij}^{10}}\right) + W_{elec}\sum_{i,j}\frac{q_i q_j}{4\pi\varepsilon r_{ij}}$$

$$+ W_{sol}\sum_{i,j}(S_i V_j + S_j V_i)e^{-r_{ij}^2/2\sigma^2}$$

Where W is the weighting constant for each term. E(t) provides directionality based on the angle t from ideal H-bonding geometry. S is solvation parameter, and $\sigma = 3.5$ Å.

1.8 Outline of the dissertation

A complete understanding of the interaction dynamics on the interface is crucial for the development of carbon-based nanomaterials with unique functions. This study provides an approach to investigate the dynamics on the interface with molecular dynamics simulation and computational docking, and subsequently utilize the theoretical results for the development of novel carbon-based nanomaterials.

In Chapter 2, the dynamics on the interface of graphene, graphene oxide, and graphene amphiphilic Janus nanosheet (AJN) with poly (sodium 4-styrenesulfonate) (PSS) was studied. We demonstrated that PSS could improve the stability of AJN in brine without damaging its amphiphilic property in both experiment and simulation. A scalable and efficient method for the AJN synthesis with graphene oxide and tapioca starch was also investigated.

In Chapter 3, we studied the binding dynamics on the interface of CNT with three proteins. We found that immunoglobulin G (IgG) is apt to bind with CNTs. The binding of IgG to SWCNTs would enhance cellular uptake of nanotubes, and stimulate human myeloperoxidase (MPO) release and OCl^- formation in neutrophils, thereby facilitating their degradation process.

In Chapter 4 and Chapter 5, the mechanism of a CNT array ultra-sensitive biosensor was revealed. Self-assembly is a novel perspective to understand the formation of the recognition. This research further suggested a new approach to design and synthesized the protein imprint. A theoretical approach utilizing molecular dynamics and docking analysis was proposed to efficiently examine the imprinting compounds from a chemical library by the computation of molecular interactions.

1.9 References

1. Zhang, L., L. Wang, Y.-T. Kao, W. Qiu, Y. Yang, O. Okobiah, and D. Zhong, *Mapping Hydration Dynamics around a Protein Surface.* Proceedings of the National Academy of Sciences, 2007. **104**(47): p. 18461-18466.

2. Stigliano, A.F., *Biomolecular Interfaces: Interactions, Functions and Drug Design*. 2015: Springer.

3. Sela-Culang, I., V. Kunik, and Y. Ofran, *The Structural Basis of Antibody-Antigen Recognition.* Frontiers in Immunology. **4**: p. 302. 2013.

4. Fernández, A., R. Scott, and R.S. Berry, *The Nonconserved Wrapping of Conserved Protein Folds Reveals a Trend toward Increasing Connectivity in Proteomic Networks.*

Proceedings of the National Academy of Sciences of the United States of America, 2004. **101**(9): p. 2823-2827.

5. Fernández, A. and R.S. Berry, *Molecular Dimension Explored in Evolution to Promote Proteomic Complexity.* Proceedings of the National Academy of Sciences of the United States of America, 2004. **101**(37): p. 13460-13465.

6. Fernández, A., *Incomplete Protein Packing as a Selectivity Filter in Drug Design.* Structure, 2005. **13**(12): p. 1829-1836.

7. Deremble, C. and R. Lavery, *Macromolecular Recognition.* Current Opinion in Structural Biology, 2005. **15**(2): p. 171-175.

8. Kortemme, T. and D. Baker, *Computational Design of Protein–Protein Interactions.* Current Opinion in Chemical Biology, 2004. **8**(1): p. 91-97.

9. Adesokan, A.A., V.A. Roberts, K.W. Lee, R.D. Lins, and J.M. Briggs, *Prediction of Hiv-1 Integrase/Viral DNA Interactions in the Catalytic Domain by Fast Molecular Docking.* Journal of Medicinal Chemistry, 2004. **47**(4): p. 821-828.

10. Fernández, A. and H.A. Scheraga, *Insufficiently Dehydrated Hydrogen Bonds as Determinants of Protein Interactions.* Proceedings of the National Academy of Sciences, 2003. **100**(1): p. 113-118.

11. Ban, Y.-E.A., H. Edelsbrunner, and J. Rudolph, *Interface Surfaces for Protein-Protein Complexes.* Journal of the Association for Computing Machinery(JACM), 2006. **53**(3): p. 361-378.

12. Kortvelyesi, T., M. Silberstein, S. Dennis, and S. Vajda, *Improved Mapping of Protein Binding Sites.* Journal of Computer-Aided Molecular Design, 2003. **17**(2): p. 173-186.

13. Lu, L., H. Lu, and J. Skolnick, *Multiprospector: An Algorithm for the Prediction of Protein–Protein Interactions by Multimeric Threading.* Proteins: Structure, Function, and Bioinformatics, 2002. **49**(3): p. 350-364.

14. Zaera, F., *Surface Chemistry at the Liquid/Solid Interface.* Surface Science, 2011. **605**(13): p. 1141-1145.

15. Zaera, F., *Probing Liquid/Solid Interfaces at the Molecular Level.* Chemical Reviews, 2012. **112**(5): p. 2920-2986.

16. Hind, A.R., S.K. Bhargava, and A. McKinnon, *At the Solid/Liquid Interface: Ftir/Atr—the Tool of Choice.* Advances in Colloid and Interface Science, 2001. **93**(1): p. 91-114.

17. Greenler, R.G., *Infrared Study of Adsorbed Molecules on Metal Surfaces by Reflection Techniques.* The Journal of Chemical Physics, 1966. **44**(1): p. 310-315.

18. Krejčik, M., M. Daněk, and F. Hartl, *Simple Construction of an Infrared Optically Transparent Thin-Layer Electrochemical Cell: Applications to the Redox Reactions of*

Ferrocene, Mn2 (Co) 10 and Mn (Co) 3 (3, 5-Di-T-Butyl-Catecholate)−. Journal of Electroanalytical Chemistry and Interfacial Electrochemistry, 1991. **317**(1-2): p. 179-187.

19. Gao, P. and M.J. Weaver, *Surface-Enhanced Raman Spectroscopy as a Probe of Adsorbate-Surface Bonding: Benzene and Monosubstituted Benzenes Adsorbed at Gold Electrodes.* The Journal of Physical Chemistry, 1985. **89**(23): p. 5040-5046.

20. Bain, C.D., *Studies of Adsorption at Interfaces by Optical Techniques: Ellipsometry, Second Harmonic Generation and Sum-Frequency Generation.* Current Opinion in Colloid & Interface Science, 1998. **3**(3): p. 287-292.

21. Decher, G., J.D. Hong, and J. Schmitt, *Buildup of Ultrathin Multilayer Films by a Self-Assembly Process: Iii. Consecutively Alternating Adsorption of Anionic and Cationic Polyelectrolytes on Charged Surfaces.* Thin Solid Films, 1992. **210**: p. 831-835.

22. Serrano, A.G., E.J. Cabré, J.M. Oviedo, A. Cruz, B. González, A. Palacios, P. Estrada, and J. Pérez-Gil, *Production in Escherichia Coli of a Recombinant C-Terminal Truncated Precursor of Surfactant Protein B (Rprosp-B Δc). Structure and Interaction with Lipid Interfaces.* Biochimica et Biophysica Acta (BBA)-Biomembranes, 2006. **1758**(10): p. 1621-1632.

23. Williams, C.T. and D.A. Beattie, *Probing Buried Interfaces with Non-Linear Optical Spectroscopy.* Surface Science, 2002. **500**(1): p. 545-576.

24. Phillips, K.S. and Q. Cheng, *Recent Advances in Surface Plasmon Resonance Based Techniques for Bioanalysis.* Analytical and Bioanalytical Chemistry, 2007. **387**(5): p. 1831-1840.

25. Tengvall, P., I. Lundström, and B. Liedberg, *Protein Adsorption Studies on Model Organic Surfaces: An Ellipsometric and Infrared Spectroscopic Approach.* Biomaterials, 1998. **19**(4): p. 407-422.

26. Martin, S.J., V.E. Granstaff, and G.C. Frye, *Characterization of a Quartz Crystal Microbalance with Simultaneous Mass and Liquid Loading.* Analytical Chemistry, 1991. **63**(20): p. 2272-2281.

27. Koningsberger, D.C. and R. Prins, *X-Ray Absorption: Principles, Applications, Techniques of Exafs, Sexafs, and Xanes.* 1988. Wiley.

28. Renaud, G., R. Lazzari, and F. Leroy, *Probing Surface and Interface Morphology with Grazing Incidence Small Angle X-Ray Scattering.* Surface Science Reports, 2009. **64**(8): p. 255-380.

29. Als-Nielsen, J., D. Jacquemain, K. Kjaer, F. Leveiller, M. Lahav, and L. Leiserowitz, *Principles and Applications of Grazing Incidence X-Ray and Neutron Scattering from Ordered Molecular Monolayers at the Air-Water Interface.* Physics Reports, 1994. **246**(5): p. 251-313.

30. Torikai, N., N.L. Yamada, A. Noro, M. Harada, D. Kawaguchi, A. Takano, and Y. Matsushita, *Neutron Reflectometry on Interfacial Structures of the Thin Films of Polymer and Lipid.* Polymer Journal, 2007. **39**(12): p. 1238.

31. Halka, V. and W. Freyland, *Thermal Stability of Surface Freezing Films in Ga-Based Alloys: An X-Ray Photoelectron Spectroscopy and Scanning Tunneling Microscopy Study.* The Journal of Chemical Physics, 2007. **127**(3): p. 034702.

32. Derome, A.E., *Modern Nmr Techniques for Chemistry Research*. Vol. 6. 2013: Elsevier.

33. Rieger, P., *Electron Spin Resonance: Analysis and Interpretation*. 2007: Royal Society of Chemistry.

34. Lund, A., M. Shiotani, and S. Shimada, *Applications of Quantitative Esr*, in *Principles and Applications of Esr Spectroscopy*. 2011, Springer. p. 409-438.

35. Conchello, J.A. and J.W. Lichtman, *Fluorescence Microscopy.* Nature Methods, 2005. **2**: p. 910-919.

36. Swain, R.J. and M.M. Stevens, *Raman Microspectroscopy for Non-Invasive Biochemical Analysis of Single Cells*. 2007, Portland Press Limited.

37. Campagnola, P.J., A. Lewis, and L.M. Loew, *High-Resolution Nonlinear Optical Imaging of Live Cells by Second Harmonic Generation.* Biophysical journal, 1999. **77**(6): p. 3341-3349.

38. Miller, L.M., G.L. Carr, M. Jackson, P. Dumas, and G.P. Williams, *The Impact of Infrared Synchrotron Radiation in Biology: Past, Present and Future.* Synchrotron Radiation News, 2000. **13**(5): p. 31-38.

39. Foster, J.S. and J.E. Frommer, *Imaging of Liquid Crystals Using a Tunnelling Microscope.* Nature, 1988. **333**(6173): p. 542-545.

40. Bard, A.J., F.R.F. Fan, J. Kwak, and O. Lev, *Scanning Electrochemical Microscopy. Introduction and Principles.* Analytical Chemistry, 1989. **61**(2): p. 132-138.

41. Zhong, Q., D. Inniss, K. Kjoller, and V.B. Elings, *Fractured Polymer/Silica Fiber Surface Studied by Tapping Mode Atomic Force Microscopy.* Surface Science, 1993. **290**(1-2): p. L688-L692.

42. Lewis, A., H. Taha, A. Strinkovski, A. Manevitch, A. Khatchatouriants, R. Dekhter, and E. Ammann, *Near-Field Optics: From Subwavelength Illumination to Nanometric Shadowing.* Nature biotechnology, 2003. **21**(11): p. 1378.

43. Thiberge, S., A. Nechushtan, D. Sprinzak, O. Gileadi, V. Behar, O. Zik, Y. Chowers, S. Michaeli, J. Schlessinger, and E. Moses, *Scanning Electron Microscopy of Cells and Tissues under Fully Hydrated Conditions.* Proceedings of the National Academy of Sciences of the United States of America, 2004. **101**(10): p. 3346-3351.

44. Williamson, M.J., R.M. Tromp, P.M. Vereecken, R. Hull, and F.M. Ross, *Dynamic Microscopy of Nanoscale Cluster Growth at the Solid-Liquid Interface.* Nature Materials, 2003. **2**(8): p. 532.

45. Kroto, H.W., J.R. Heath, S.C. O'Brien, R.F. Curl, and R.E. Smalley, *C 60: Buckminsterfullerene.* Nature, 1985. **318**(6042): p. 162-163.

46. Iijima, S., *Helical Microtubules of Graphitic Carbon.* Nature, 1991. **354**(6348): p. 56.

47. Novoselov, K.S., A.K. Geim, S.V. Morozov, D. Jiang, Y. Zhang, S.V. Dubonos, I.V. Grigorieva, and A.A. Firsov, *Electric Field Effect in Atomically Thin Carbon Films.* Science, 2004. **306**(5696): p. 666-669.

48. Geim, A.K. and K.S. Novoselov, *The Rise of Graphene.* Nature Materials, 2007. **6**(3): p. 183-191.

49. Lee, G.-H., R.C. Cooper, S.J. An, S. Lee, A. van der Zande, N. Petrone, A.G. Hammerberg, C. Lee, B. Crawford, and W. Oliver, *High-Strength Chemical-Vapor–Deposited Graphene and Grain Boundaries.* Science, 2013. **340**(6136): p. 1073-1076.

50. Segal, M., *Selling Graphene by the Ton.* Nature Nanotechnology, 2009. **4**(10): p. 612-614.

51. Park, S. and R.S. Ruoff, *Chemical Methods for the Production of Graphenes.* Nature Nanotechnology, 2009. **4**(4): p. 217-224.

52. Kumar, H.V., S.J. Woltornist, and D.H. Adamson, *Fractionation and Characterization of Graphene Oxide by Oxidation Extent through Emulsion Stabilization.* Carbon, 2016. **98**: p. 491-495.

53. Luo, D., F. Wang, J. Zhu, F. Cao, Y. Liu, X. Li, R.C. Willson, Z. Yang, C.W. Chu, and Z. Ren, *Nanofluid of Graphene-Based Amphiphilic Janus Nanosheets for Tertiary or Enhanced Oil Recovery: High Performance at Low Concentration.* Proceedings of the National Academy of Sciences (PNAS), USA, 2016. **113**(28): p. 7711-6.

54. Srinivasan, C., *Carbon Nanotubes in Cancer Therapy.* Current Science, 2008. **94**(3): p. 300-301.

55. *Nanomaterials for Biosensors*, ed. C. Kumar. 2007: Wiley-VCH.

56. Banks, C.E., R.R. Moore, T.J. Davies, and R.G. Compton, *Investigation of Modified Basal Plane Pyrolytic Graphite Electrodes: Definitive Evidence for the Electrocatalytic Properties of the Ends of Carbon Nanotubes.* Chemical Communications, 2004(16): p. 1804-1805.

57. Banks, C.E. and R.G. Compton, *New Electrodes for Old: From Carbon Nanotubes to Edge Plane Pyrolytic Graphite.* Analyst, 2006. **131**(1): p. 15-21.

58. Tothill, I.E. *Biosensors for Cancer Markers Diagnosis*. in *Seminars in Cell & Developmental Biology*. 2009. Elsevier.

59. Subrahmanyam, S., S.A. Piletsky, and A.P.F. Turner, *Application of Natural Receptors in Sensors and Assays.* Analytical Chemistry, 2002. **74**(16): p. 3942-3951.

60. Borrebaeck, C.A.K. and C. Wingren, *Design of High-Density Antibody Microarrays for Disease Proteomics: Key Technological Issues.* Journal of Proteomics, 2009. **72**(6): p. 928-935.

61. Whitcombe, M.J., I. Chianella, L. Larcombe, S.A. Piletsky, J. Noble, R. Porter, and A. Horgan, *The Rational Development of Molecularly Imprinted Polymer-Based Sensors for Protein Detection.* Chemical Society Reviews, 2011. **40**(3): p. 1547-1571.

62. Turner, A.P.F., B. Chen, and S.A. Piletsky, *In Vitro Diagnostics in Diabetes: Meeting the Challenge.* Clinical Chemistry, 1999. **45**(9): p. 1596-1601.

63. Mayes, A.G. and M.J. Whitcombe, *Synthetic Strategies for the Generation of Molecularly Imprinted Organic Polymers.* Advanced Drug Delivery Reviews, 2005. **57**(12): p. 1742-1778.

64. Yan, M., *Molecularly Imprinted Materials: Science and Technology*. 2004: CRC press.

65. Chen, L., S. Xu, and J. Li, *Recent Advances in Molecular Imprinting Technology: Current Status, Challenges and Highlighted Applications.* Chemical Society Reviews, 2011. **40**(5): p. 2922-2942.

66. Hori, S.S. and S.S. Gambhir, *Mathematical Model Identifies Blood Biomarker–Based Early Cancer Detection Strategies and Limitations.* Science Translational Medicine, 2011. **3**(109): p. 109ra116-109ra116.

67. Arlett, J.L., E.B. Myers, and M.L. Roukes, *Comparative Advantages of Mechanical Biosensors.* Nature Nanotechnology, 2011. **6**(4): p. 203-215.

68. Livnah, O., E.A. Bayer, M. Wilchek, and J.L. Sussman, *Three-Dimensional Structures of Avidin and the Avidin-Biotin Complex.* Proceedings of the National Academy of Sciences, 1993. **90**(11): p. 5076-5080.

69. Alder, B.J. and T.E. Wainwright, *Studies in Molecular Dynamics. I. General Method.* Journal of Chemical Physics, 1959. **31**(2): p. 459-466.

70. M.J. Abraham, D.v.d.S., E. Lindahl, B. Hess, and the GROMACS development team, *Gromacs User Manual Version 5.0.5.* http://www.gromacs.org, 2015.

71. Abraham, M.J., T. Murtola, R. Schulz, S. Páll, J.C. Smith, B. Hess, and E. Lindahl, *Gromacs: High Performance Molecular Simulations through Multi-Level Parallelism from Laptops to Supercomputers.* SoftwareX, 2015. **1**: p. 19-25.

72. Phillips, J.C., R. Braun, W. Wang, J. Gumbart, E. Tajkhorshid, E. Villa, C. Chipot, R.D. Skeel, L. Kale, and K. Schulten, *Scalable Molecular Dynamics with Namd.* Journal of Computational Chemistry, 2005. **26**(16): p. 1781-1802.

73. Case, D.A., T.E. Cheatham, T. Darden, H. Gohlke, R. Luo, K.M. Merz, A. Onufriev, C. Simmerling, B. Wang, and R.J. Woods, *The Amber Biomolecular Simulation Programs.* Journal of Computational Chemistry, 2005. **26**(16): p. 1668-1688.

74. Brooks, B.R., C.L. Brooks, A.D. MacKerell, L. Nilsson, R.J. Petrella, B. Roux, Y. Won, G. Archontis, C. Bartels, and S. Boresch, *Charmm: The Biomolecular Simulation Program.* Journal of Computational Chemistry, 2009. **30**(10): p. 1545-1614.

75. Scott, W.R.P., P.H. Hünenberger, I.G. Tironi, A.E. Mark, S.R. Billeter, J. Fennen, A.E. Torda, T. Huber, P. Krüger, and W.F. van Gunsteren, *The Gromos Biomolecular Simulation Program Package.* The Journal of Physical Chemistry A, 1999. **103**(19): p. 3596-3607.

76. Jorgensen, W.L., D.S. Maxwell, and J. Tirado-Rives, *Development and Testing of the Opls All-Atom Force Field on Conformational Energetics and Properties of Organic Liquids.* Journal of the American Chemical Society (JACS), 1996. **118**(45): p. 11225-11236.

77. Ponder, J.W. and D.A. Case, *Force Fields for Protein Simulations.* Advances in Protein Chemistry, 2003. **66**: p. 27-85.

78. MacKerell Jr, A.D., *Atomistic Models and Force Fields.* Computational Biochemistry and Biophysics, 2001: p. 7-38.

79. Schmid, N., A.P. Eichenberger, A. Choutko, S. Riniker, M. Winger, A.E. Mark, and W.F. van Gunsteren, *Definition and Testing of the Gromos Force-Field Versions 54a7 and 54b7.* European Biophysics Journal, 2011. **40**(7): p. 843-856.

80. Lengauer, T. and M. Rarey, *Computational Methods for Biomolecular Docking.* Current Opinion in Structural Biology, 1996. **6**(3): p. 402-406.

81. Morris, G.M., R. Huey, W. Lindstrom, M.F. Sanner, R.K. Belew, D.S. Goodsell, and A.J. Olson, *Autodock4 and Autodocktools4: Automated Docking with Selective Receptor Flexibility.* Journal of Computational Chemistry, 2009. **30**(16): p. 2785-2791.

82. Trott, O. and A.J. Olson, *Autodock Vina: Improving the Speed and Accuracy of Docking with a New Scoring Function, Efficient Optimization, and Multithreading.* Journal of Computational Chemistry, 2010. **31**(2): p. 455-461.

83. Singh, T., D. Biswas, and B. Jayaram, *Aads-an Automated Active Site Identification, Docking, and Scoring Protocol for Protein Targets Based on Physicochemical Descriptors.* Journal of Chemical Information and Modeling, 2011. **51**(10): p. 2515-2527.

84. Kim, D.-S., C.-M. Kim, C.-I. Won, J.-K. Kim, J. Ryu, Y. Cho, C. Lee, and J. Bhak, *Betadock: Shape-Priority Docking Method Based on Beta-Complex.* Journal of Biomolecular Structure and Dynamics, 2011. **29**(1): p. 219-242.

Chapter 2 Graphene-based amphiphilic Janus nanosheet (AJN)

A part of this chapter contains our unpublished works in the submitted manuscripts:

1. Luo, D., Chen, J.,Wang, F., Wang, D., Willson, R. C., Cai, D., Ren, Z., Stabilization of amphiphilic Janus nanosheets in relatively high salt water with retained inferfacial behavior: experimental and MD study.

2. Luo, D., Wang, F., Vu, B., Chen, J., Bao, J., Cai, D., Willson, R. C., Ren, Z., Synthesis of graphene-based amphiphilic Janus nanosheet via manipulation of hydrogen bonding.

2.1 Introduction

With the decline in oil discoveries, the oil recovery technologies attract more attentions in recent decades. Enhanced oil recovery (EOR) is a kind of technique for increasing the amount of crude oil exaction after primary and secondary recovery. Chemical injection is one of the EOR technique which injects various chemicals, such as polymers, surfactants, and microbial, into the oil wells for oil recovery [1]; however, the application of chemical injection is limited by the high cost, low efficiency, and the harm to the environment. Simple nanofluid (containing only nanoparticles) flooding at low concentration (0.01 wt % or less) is a promising alternative, but the efficiency is below 5% in a saline environment (2 wt % or higher NaCl content). Recently, Dan Luo et al. (2016) reported a simple nanofluid of graphene-based amphiphilic Janus nanosheets (AJN) for enhanced oil recovery with an efficiency of about 15.2%, comparable to chemical methods, which is both economically and environmentally beneficial to the petroleum industry [2]. AJN can increase mobility and reduce the interfacial tension crude oil, and therefore improve the recovery rate.

However, AJN is unstable in brine, which limits its application in the industry (Figure 2.1). Here we investigated the surface properties of graphene, graphene oxide (GO), and graphene AJN, and proposed a strategy to improve the stability of graphene AJN by adding poly (sodium 4-styrenesulfonate) (PSS) polymers.

PSS is a highly negative charged polymer. With both hydrophilic group and hydrophobic carbon backbone, PSSs can attach to the surface of graphene and graphene derivatives. PSSs enclose graphene and graphene derivatives and form particles that have a negatively charged surface. These particles are mutually repulsive and stable in the aqueous dispersion.

With the help of molecular dynamics simulation, we explored how PSSs interact with graphene, graphene oxide, and graphene AJN. Associated with experiments, we also investigated the binding interface of graphene AJN with PSSs in water and brine. Besides, we also examined how PSS-bonded AJN behaved in oil-water biphasic solution. We found that the stability of AJN in both water and brine is improved by adding PSSs without damaging its amphiphilic property.

Figure 2.1 Graphene AJN is unstable in brine.

2.2 PSS binding interface with graphene, graphene oxide, and AJN

2.2.1 Molecular dynamics simulation methods

A 24.9 Å × 25.9 Å mono layer graphene with 238 carbon atoms was used as substrate [3]. A 30% oxidized graphene oxide was constructed by attached 4 carboxyls to the edges, 24 epoxides to the bottom, and 28 hydroxyls to the top and sides of the substrate graphene. 5 alkylamines were appended to the top side of graphene oxide to construct graphene AJN. 6 sodium 4-styrenesulfonate (SS) units were connected as a PSS molecule. All of the construction processes were implemented with PyMOL [4]. The charge distribution of PSS was computed with Atomic Charge Calculator [5]. The topology structures were created with TPPmktop [6].

The molecular dynamics simulation was performed using GROMACS 5.1.4 [7]. OPLS-AA force field was used for the simulation [8]. Three target structures were investigated separately: (1) graphene, (2) graphene oxide, and (3) graphene AJN, as shown in Figure 2.2. 5 PSS molecules were randomly distributed around the target structure, then solvated in TIP3P water, followed by the addition of 30 sodium ions (Na+) to make the system charge neutral. The periodic box size and the number of solvent water were (1) 70 Å × 70 Å × 70 Å and 10920, (2) 70 Å × 70 Å × 70 Å and 10920, and (3) 80 Å × 80 Å × 80 Å and 16569, respectively. The process is shown in Figure 2.3. After an energy minimization, the system underwent a 5 ns equilibration at 300 K (NVT ensemble) and a 5 ns equilibration at 1 bar (NPT ensemble), followed by a 100 ns production. The time step was set to 2 fs. The information of system was recorded every 10 ps. All bond lengths were constrained using the LINCS algorithm. Cut-off of 1.2 nm was used for Lennard-Jones interactions and the real part of the long-range electrostatic interactions, which were calculated using the Particle-Mesh Ewald (PME) method. 0.16 nm grid spacing was used for PME.

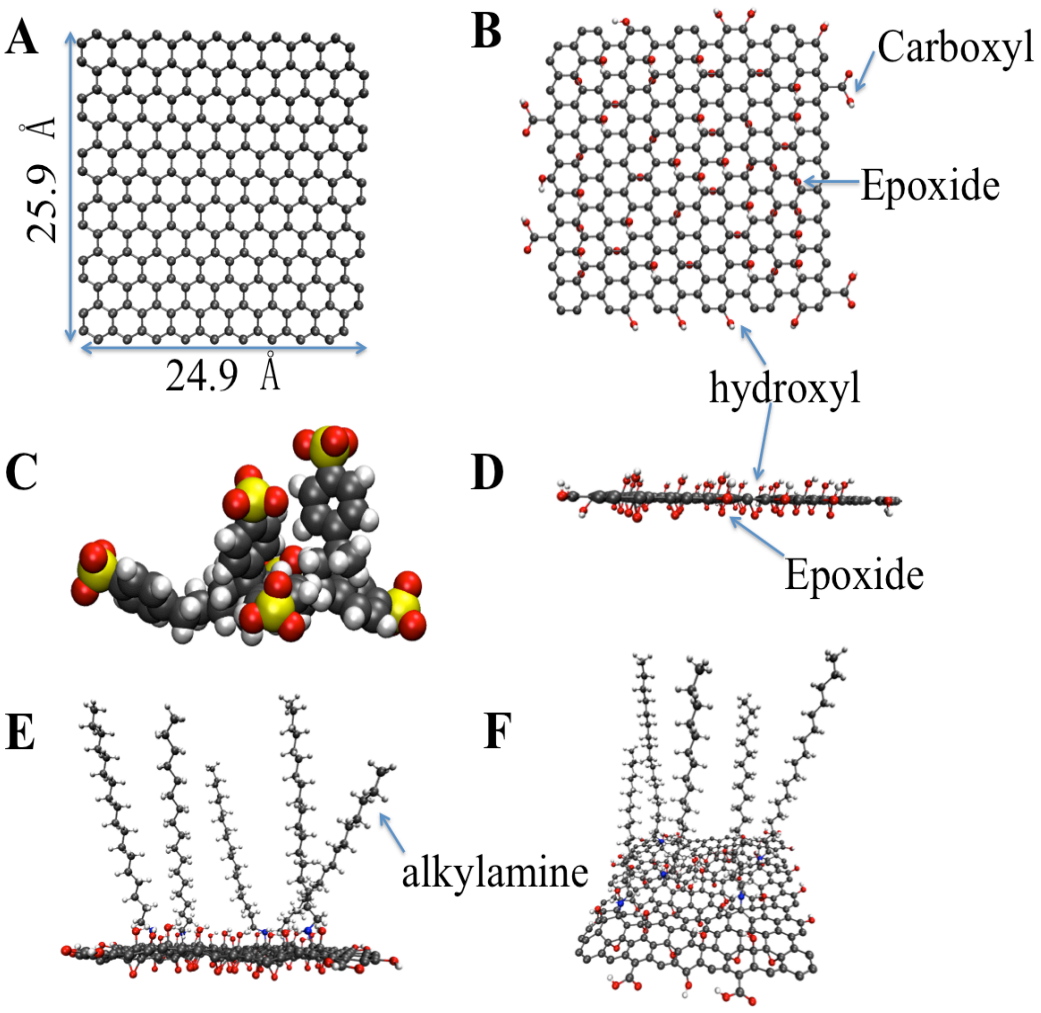

Figure 2.2 The structure of graphene, graphene oxide, and AJN.
(A) 24.9 Å × 25.9 Å mono layer graphene with 238 carbon atoms, (B) top view of graphene oxide, (D) side view of graphene oxide, (C) PSS with 6 SS units, (E) side view of graphene AJN, (F) top view of graphene AJN.

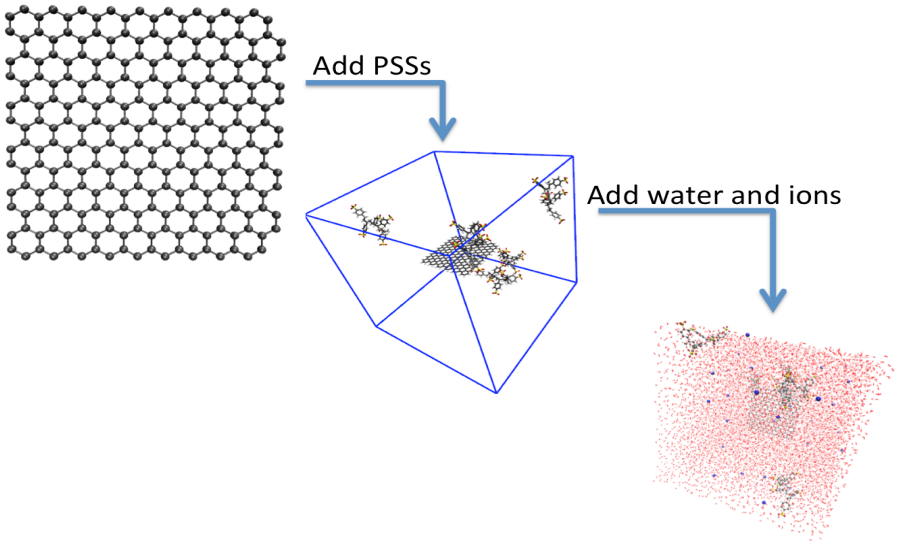

Figure 2.3 Preparation processes of molecular dynamics simulation. (1) Randomly distribute 5 PSS molecules around target structure within a periodic box; (2) add solvent water and 30 sodium ions into the box.

2.2.2 Simulation results

Three target structures were investigated with molecular dynamics simulation: (1) graphene, (2) graphene oxide, and (3) graphene AJN. Structures are shown in Figure 2.2. In all three simulations, 3 out of 5 PSS molecules combine with the target structure, as illustrated in Figure 2.5. Two of them are on the top side and the other one is on the bottom side. Both top-view and side-view of the binding configurations of graphene, graphene oxide, and graphene AJN are shown in Figure 2.5. From the binding interface between PSSs and target structures, we can find the dominant binding interactions. The carbon backbone of PSS is closed to graphene's surfaces, while the sulfonate functional group is apart from it (Figure 2.5A and B). The binding interface for graphene is hydrophobic, which indicates the dominant interaction between PSSs and graphene is van der Waals interactions and hydrophobic interactions. PSSs enclose graphene, forming a particle with a hydrophobic core and a hydrophilic surface. The highly negative charged surface prevents graphene from aggregation, therefore, improving the stability of graphene in aqueous solution. The binding interface is different for graphene oxide. The sulfonate

functional groups are closed to the top-side surface of graphene oxide and form hydrogen bonds with hydroxyl groups (Figure 2.5C and D). On the bottom side, the binding interface between PSS and graphene oxide is hydrophobic. The binding interface indicates that the dominant interactions on the top side of graphene oxide are hydrogen bonds and electrostatic interactions, while the dominant interactions on the bottom side are van der Waals interactions and hydrophobic interactions. The complex structure consists of one hydrophilic surface and one hydrophobic surface, which are unstable in aqueous solution. It may dimerize as a sandwich structure with graphene oxide on the top and bottom and PSSs in the middle (Figure 2.4). For graphene AJN, alkylamines chains cover the top side. The carbon backbones of PSS bind to alkylamine and part of sulfonate functional groups connect with hydroxyl groups by hydrogen bonds (Figure 2.5E and F). This indicates the dominant interactions are hydrophobic interactions and hydrogen bonds on the top side of AJN. On the bottom side, van der Waals interactions and hydrophobic interactions still play the dominant role. The cover of alkylamine facilitates a hollow particle with hydrophilic center and surface.

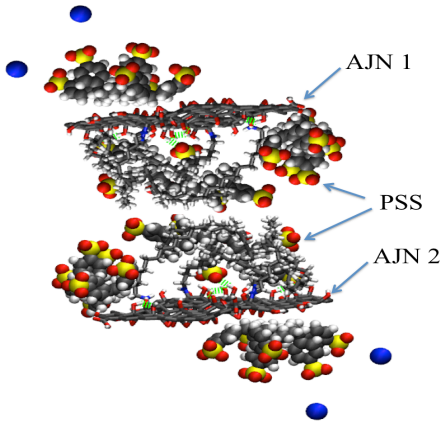

Figure 2.4 Illustration of the dimerization of PSS enclosed AJN.
The AJN-PSS complex structure consists of one hydrophilic surface and one hydrophobic surface, which are unstable in aqueous solution. It may dimerize as a sandwich structure with graphene oxide on the top and bottom and PSSs in the middle.

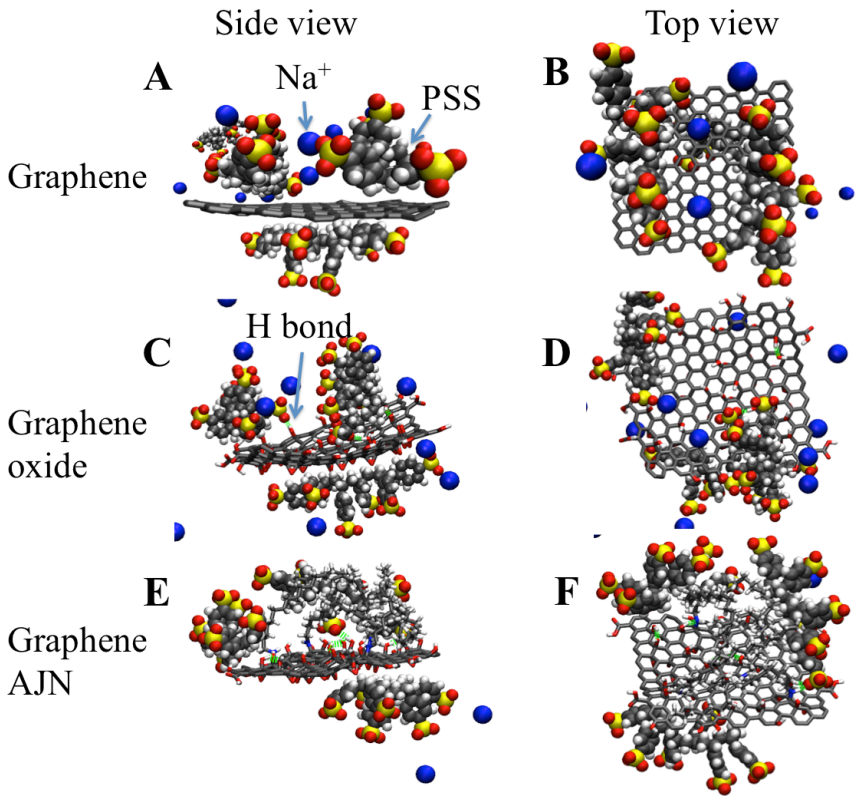

Figure 2.5 Simulation result: graphene, graphene oxide, and graphene AJN bind with PSSs.
Target structure binds with 3 PSS: two on the top side and one on the bottom side. Panel A and B are binding configurations of graphene. Panel C and D are binding configurations of graphene oxide. Panel E and F are binding configurations of graphene AJN. Panel A, C, and E are side views of configurations. Panel B, D, and F are top views of configurations. Blue beads are sodium ions. Green dotted lines are hydrogen bonds. (A) PSSs combine with graphene by hydrophobic interactions. The carbon backbone of PSS is closed to graphene, while the sulfate group is apart from it. PSSs surround graphene, forming a particle with a hydrophobic core and a hydrophilic surface. (C) On the top side (hydroxyl surface), PSSs bind to graphene oxide by hydrogen bonds and electrostatic interactions. The sulfonate functional groups are closed to graphene oxide, while the carbon backbone is apart from it, forming a hydrophobic top side surface. On the bottom side (epoxy surface), the carbon backbone of PSS is closed to graphene oxide, while the sulfate groups are apart from it, forming a negative charged hydrophilic bottom-side surface. The complex structure consists of one hydrophilic surface and one hydrophobic surface. (E) For graphene AJN, alkylamines form a cover on the top side. The carbon backbone of PSS close to alkylamine, and part of sulfonate functional groups also connect with hydroxyl groups by hydrogen bonds. The dominant interactions are hydrophobic interaction and hydrogen bond on the top side. On the bottom side, hydrophobic interaction still plays the dominant role. The cover of alkylamine facilitates a hollow particle with hydrophilic center and surface.

Figure 2.5 only shows the binding configuration in the equilibrium state. To investigate the binding dynamics, we track the evolution of center of mass (COM) distances between 5 PSSs and target structures in 100 ns in Figure 2.6. The distance is represented by orange dotted lines. Panel A shows the schematics of COM distance between PSSs and graphene. Two PSSs are far way from graphene (more than 4 nm), in the meanwhile, the other three are closed to graphene (around 1 nm). The binding dynamics are very different for graphene, graphene oxide, and graphene AJN (Figure 2.6B, C, and D). (B) The distances between PSSs and graphene fluctuate between 0.5 nm and 5.0 nm. Every PSS can approach graphene surface and every PSS is apart from graphene for some times. None of 5 PSSs sticks to graphene for a long time, implying the weak interactions between PSSs and graphene. As mentioned above, the dominant interactions are van der Waals interactions and hydrophobic interactions between PSSs and graphene, which are weak compared to hydrogen bonds and electrostatic interactions. (C) 3 out of 5 PSSs fluctuate around 1.5 nm from the graphene oxide. The small amplitude of fluctuation indicates strong and stable interactions between them. These can be attributed to the existence of hydrogen bonds and electrostatic interactions. The distances of the other two PSSs fluctuate around 4.0 nm, and approach to graphene oxide surface at the time point 22 ns and 50 ns, indicating the weak repulsive force on the surface. (D) 3 out of 5 PSSs combine to graphene AJN firmly. Their distances remain around 1.5 nm with little fluctuation, implying the interactions are strong. The distances of the other two PSSs fluctuate around 4.5 nm and always keep away from graphene AJN. It takes AJN system longer time to reach equilibrium state than graphene system and graphene oxide system. All of these should be attributed to the strong repulsive force on the surface of AJN-PSS complex.

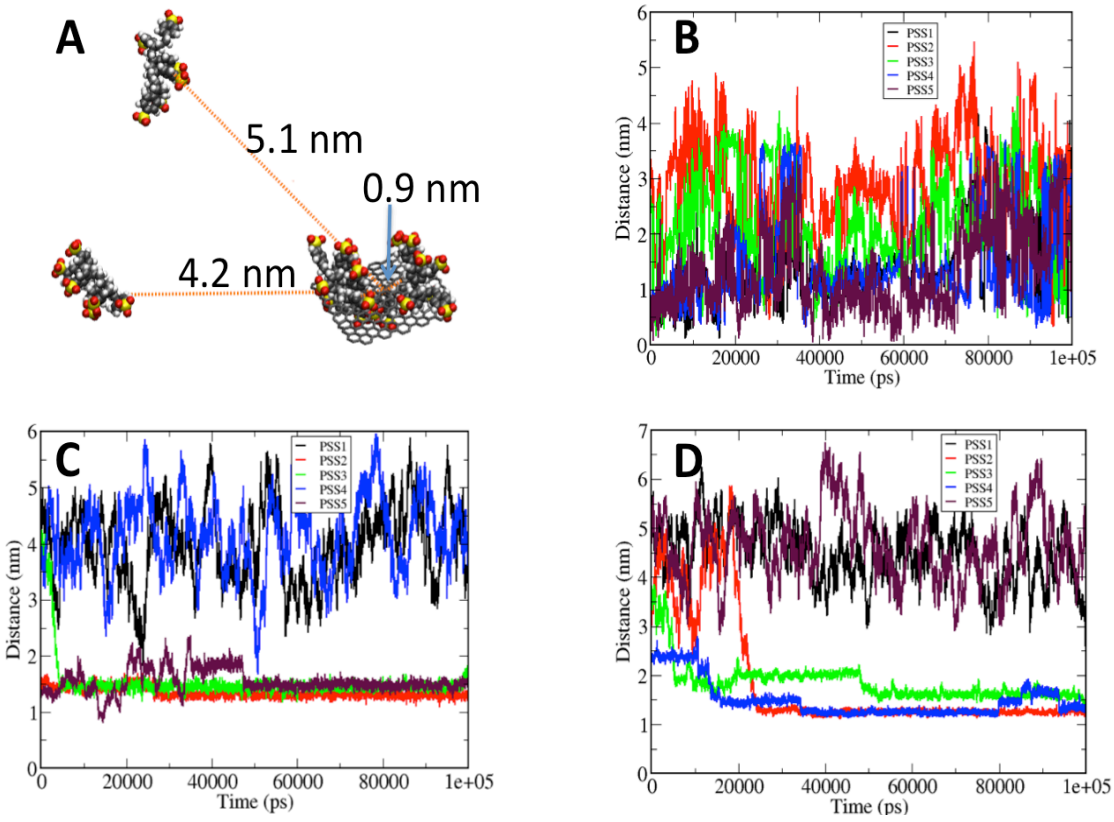

Figure 2.6 Center of mass (COM) distance between 5 PSSs and target structures.

(A) Orange dotted lines represent the distance between PSSs and graphene. Two PSSs are far way from graphene (more than 4 nm), in the meanwhile, the other three are closed to graphene (around 1 nm). (B) The distances between PSSs and graphene fluctuate between 0.5 nm and 5.0 nm. Every PSS can approach graphene and every PSS is apart from graphene for some times. None of 5 PSSs sticks to graphene for a long time, implying the weak interactions between PSSs and graphene. (C) 3 out of 5 PSSs fluctuate around 1.5 nm from the graphene oxide. Little fluctuation indicates strong interactions between them. The distances of the other two PSSs fluctuate around 4.0 nm, and approach to graphene oxide at the time point 22 ns and 50 ns, indicating the weak repulsive force on the surface. (D) 3 out of 5 PSSs combine to graphene AJN firmly. Their distances remain around 1.5 nm with little fluctuation, implying the interactions are strong. The distances of the other two PSSs fluctuate around 4.5 nm and always keep away from graphene AJN, because of the strong repulsive force on the surface.

To further investigate the contact interface, we also track the evolution of binding interface area between PSSs and target structures in 100 ns (Figure 2.7). Panel A shows the schematics of the contact interface between graphene AJN and PSSs. The contact interface is marked out by the blue rectangle. A 5 ns NVT and a 5 ns NPT equilibration run was performed before the 100 ns production run. As shown in Figure 2.7B, graphene system is in equilibrium state from the beginning of 100 ns production run, while it takes graphene oxide and graphene AJN 10 ns and 30 ns to reach equilibrium, respectively. AJN system takes long time because of the strong repulsive force on the surface. The dominant interactions between graphene and PSSs are van der Waals interactions and hydrophobic interactions, while hydrogen bonds and electrostatic interactions play a major role in both graphene oxide system and AJN system. The composition of interactions explains why graphene system reaches equilibrium state fastest. The contact interface area of graphene, graphene oxide, and graphene AJN are 15 nm^2, 10 nm^2, and 7 nm^2, respectively. The contact interface area was computed with the double cubic lattice method that proposed by Frank Eisenhaber and his colleagues in 1995 [9]. Graphene has the largest contact interface because it is closed to PSS molecules. Larger contact interface area also indicates greater short-distance interactions (van der Waals interactions and hydrophobic interactions). The contact interface area of AJN is larger than graphene oxide, implying the van der Waals interactions and hydrophobic interactions are larger between AJN and PSS molecules. The contact interface area is consistent with previous interaction analysis from the binding configuration.

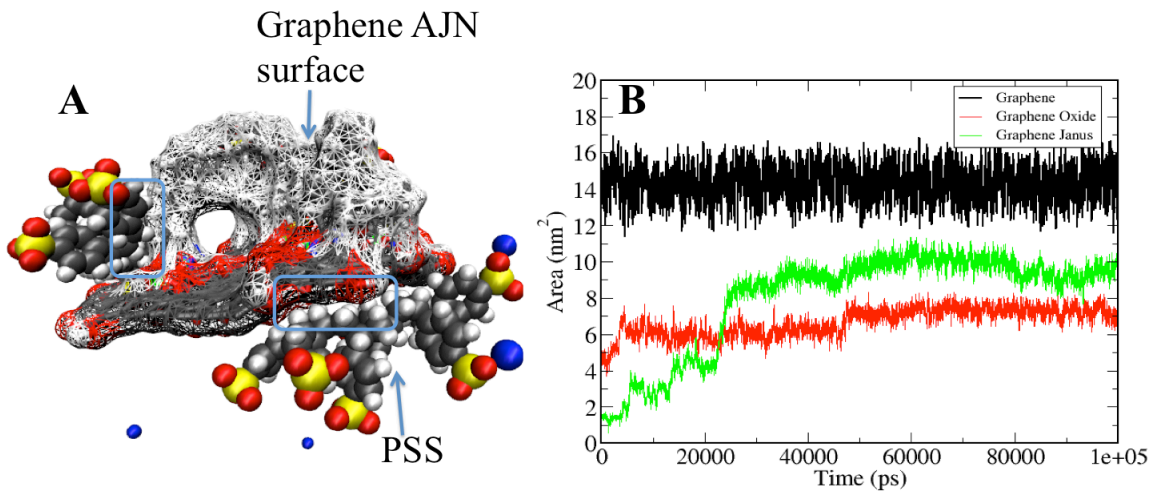

Figure 2.7 Contact interface area between target structures and PSSs. (A) Illustration of the contact interface between graphene AJN and PSSs. The contact interface is marked out by the blue rectangle. (B) A 5 ns NVT and a 5 ns NPT equilibration run was performed before the 100 ns production run. Graphene system is in equilibrium state from the beginning of production run. It takes graphene oxide and graphene AJN 10 ns and 30 ns to reach equilibrium, respectively. The contact interface area of graphene, graphene oxide, and graphene AJN are 15 nm^2, 10 nm^2, and 7 nm^2, respectively.

2.2.3 Conclusions

PSS is a highly negative charged polymer. It was widely used as ion-exchange resins to remove ions such as potassium, calcium, and sodium from solution in technical or medical applications. Here, we find that PSS is also a good additive to generate a stable aqueous dispersion of graphene, graphene oxide, and graphene AJN. Molecular dynamics simulation results indicate the binding modes are different for PSS with graphene, graphene oxide, and graphene AJN.

PSSs combine with graphene by van der Waals interactions and hydrophobic interactions, forming a particle with negative charged hydrophilic surface, which prevents the aggregation of graphene. For graphene oxide, PSSs bind to the epoxy side by van der Waals interactions and hydrophobic interactions, and bind to the hydroxyl side by hydrogen bonds and electrostatic interactions. GO-PSS complex has an amphiphilic surface, which is unstable in aqueous solution. Two of these unstable amphiphilic particles may combine, forming a sandwich structure with graphene oxide on the top and bottom and PSSs in the middle. For graphene AJN, PSSs bind to the alkylamines on the top side. All of the hydrogen bonds, electrostatic interactions, van der Waals interactions, and hydrophobic interactions play an important role in the binding. Hydrophobic interactions are still the dominant interaction in the binding of PSSs with graphene AJN's bottom side. The structure of AJN-PSS complex is a hollow particle with a hydrophilic core and a hydrophilic surface.

According to our molecular dynamics simulations, the stability of graphene will be better than graphene oxide and graphene AJN in an aqueous solution with PSS, and the stability of graphene oxide will be the worst. As PSSs bind to the bottom side of graphene AJN by hydrophobic interactions, decreasing the oxidization degree of the graphene substrate may improve its stability in aqueous solution. All of these results are required to be further verified by experiments.

2.3 PSS binds with graphene AJN in water and brine

2.3.1 Molecular dynamics simulation methods

A 24.9 Å × 25.9 Å mono layer graphene with 238 carbon atoms was used as substrate[3]. A 30% oxidized graphene oxide was constructed by attaching 4 carboxyls to the edges, 24

epoxides and 28 hydroxyls to the bottom, top and edges of the substrate graphene. 5 alkylamines were attached to the top side of graphene oxide to construct graphene AJN. 6 sodium 4-styrenesulfonate (SS) units were connected as a poly (sodium 4-styrenesulfonate) (PSS) molecule (Figure 2.2). All of the construction processes were implemented with PyMOL [4]. The charge distribution of PSS was computed with Atomic Charge Calculator [5]. The topology structures were created with TPPmktop [6].

The molecular dynamics simulation was performed using GROMACS 5.1.4 [7]. OPLS-AA force field was used for the simulation. After an energy minimization, the system underwent a 5 ns equilibration at 300 K (NVT ensemble) and a 5 ns equilibration at 1 bar (NPT ensemble), followed by a 100 ns production run. The time step was set to 2 fs. All bond lengths were constrained using the LINCS algorithm. Cut-off of 1.2 nm was used for Lennard-Jones interactions and the real part of the long-range electrostatic interactions, which were calculated using the Particle-Mesh Ewald (PME) method. 0.16 nm grid spacing was used for PME. The information of system was recorded every 100 ps.

In the simulation of AJN with PSSs in water, the periodic box size was 80 Å × 80 Å × 80 Å. 1 AJN molecule was placed in the center of the box. 5 PSSs and 16569 water molecules were randomly distributed in the box.

In the simulation of AJN with PSSs in saline solution, the periodic box size was 80 Å × 80 Å × 80 Å. 1 AJN molecule was placed in the center of the box. 5 PSSs, 188 Na^+ ions, 186 Cl^- ions, 14 Ca^{2+} ions, and 16420 water molecules were randomly distributed in the box.

2.3.2 Simulation results

A variety of graphene oxide structures were reported in literature [10, 11]. The structure of graphene oxide depends on the oxidation method used and oxidation degree [11]. We created a different model for AJN in this section according to experimental measurements. In the previous

section, 24 epoxides were on the bottom of substrate graphene, and 28 hydroxyls were on to the top and edges of the substrate graphene. In this section, 24 epoxides and 28 hydroxyls were randomly distributed on both sides of substrate graphene.

At the beginning of the simulation of PSS molecules binding with AJN, 5 PSS molecules were randomly distributed around AJN with a center of mass (COM) distance more than 3 nm. When PSS molecule binds to the bottom side of AJN, the COM distance is around 1nm, while the COM distance is around 1.6 nm when binding to the top side of AJN because of the existence of alkylamines on the top side.

In water, PSS molecules are mutually exclusive because PSS are highly negatively charged. As shown in Figure 2.8A, only two PSS molecules bind to AJN: one on the top side and the other on the bottom side. Both of them bind to AJN with the hydrophobic part, and the negatively charged sulfonate functional groups are facing outside. This indicates the dominant interactions between AJN and PSS are van der Waals interactions and hydrophobic interactions. The AJN-PSS complex has a hydrophilic surface, which makes it stable in aqueous solution. Figure 2.8C shows the evolution of COM distance between 5 PSS molecules with AJN in water. Two PSS molecules (the blue and red line in Figure 2.8C) bind to AJN in a short time and stick to AJN for 100 ns. Repulsed by these two bonded PSS molecules, the other three PSS molecules never get a chance to approach to AJN.

In the saline solution with 3% NaCl (wt) and 0.5% $CaCl_2$ (wt), the existence of ions alters the interface property. Ions shield the electrostatic interactions and impair the repulsive interactions between PSS molecules. Especially Ca^{2+} ions, which carry two positive charges, play as connectors, connecting two PSS molecules by binding to sulfonate functional groups. As shown in Figure 2.8B and D, three out of five PSS molecules bind to AJN: two on the top side and one on the bottom side. There is another PSS molecule connects to the AJN-bonded PSS by Ca^{2+} ions (the purple curve in Figure 2.8D). The contacting interface between PSS and AJN is

hydrophobic. This indicates that the dominant interactions are van der Waals interactions and hydrophobic interactions.

The simulation results show that PSS can enclose AJN and form AJN-PSS complex, which has a hydrophilic surface and stable in water and brine. The existence of ions in brine shields the electrostatic repulsive interactions; hence, the size of AJN-PSS complex particle in saline solution should be larger than that in water, which is verified by the experiment result.

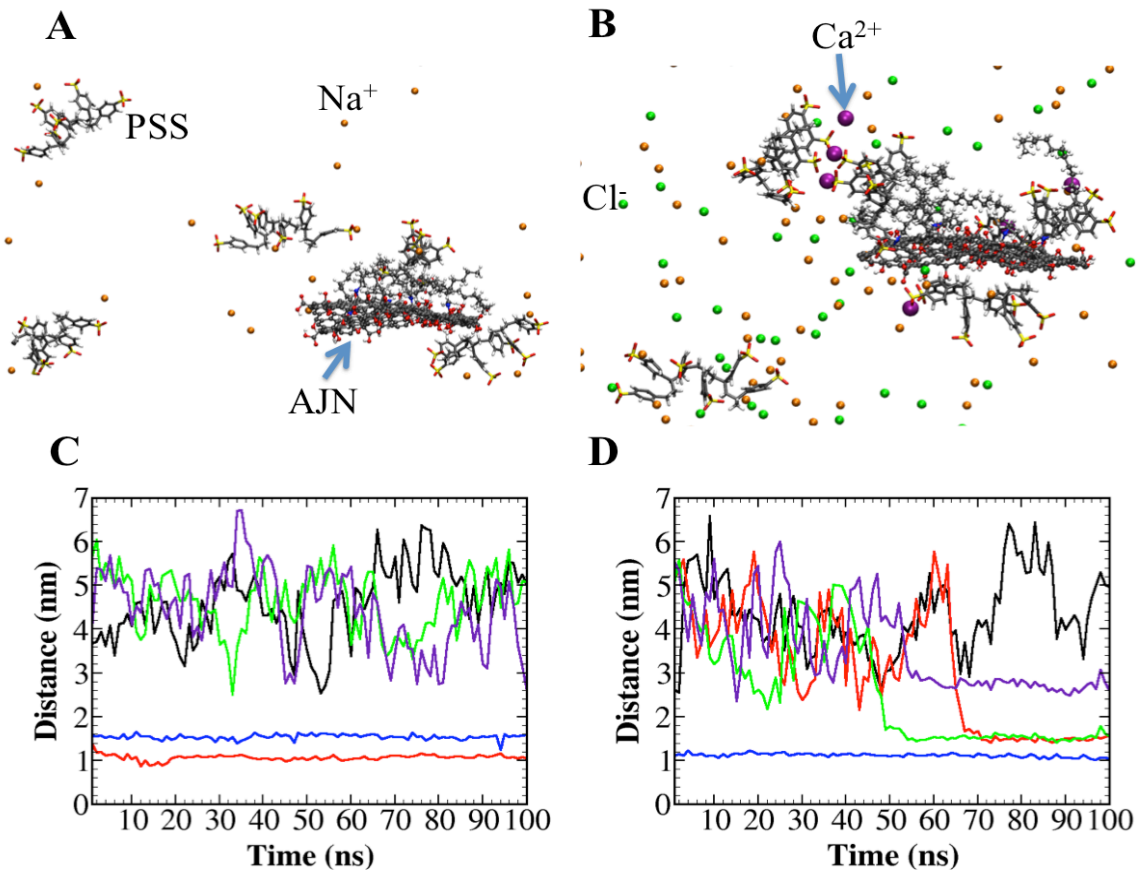

Figure 2.7 Molecule dynamics simulation of PSS with AJN.
Panel A and panel B are configurations of PSS bonded AJN at the end of 100 ns simulation in water and brine respectively. AJN is in the center, surrounded by PSS molecules and ions. Orange beads are Na^+ ions, green beads are Cl^- ions, and purple beads are Ca^{2+} ions. Panel C and panel D are the center of mass distance from 5 PSS molecules to AJN in water and brine, respectively.

2.3.3 Experiment materials and methods

Synthesis of graphene-based amphiphilic Janus nanosheets (AJN)

The amphiphilic Janus nanosheets were synthesized using the wax-masking method [12, 13]. Briefly, graphene oxide (GO) was first fabricated by the improved chemical oxidation method [14]. Paraffin wax (80 g) was melted at a temperature of 75 °C and then mixed with GO (200 mg) and water (300 g) and NaCl (8g). The mixture was vigorously stirred at 75 °C with a speed of 1800 rpm and then cooled down to room temperature. After extensive wash with NaOH (pH ~ 9), DI water and ethanol, the GO covered wax particles were dispersed in the absolute alcohol solution of octadecylamine and stirred overnight. After several washes with ethanol, wax was dissolved in toluene and removed. AJN were dried at 60 °C and the nanofluid of AJN stabilized in DI water was made.

Stabilization of AJN in brine

Poly(sodium 4-styrenesulfonate) (PSS, Mw~70000) from Sigma-Aldrich was dissolved in DI water to make solutions of different concentrations, e.g., 0.01wt%, 0.1wt%, 0.25wt%, 0.5wt%, 0.75wt% and 0.1wt%. AJNs were diluted with PSS solutions to make AJN concentrations of 0.005wt% and 0.01wt%. The dispersions of AJN/PSS were sonicated for 30 mins before NaCl (3wt%) and CaCl2 (0.5wt%) were dissolved. The AJN/PSS brine dispersions were settled for further observation and evaluation.

2.3.4 Experiment results

As Figure 2.8a shows, the average hydrodynamic size of AJN increases when the concentration of PSS increases. This indicates that PSS is attached to the surface of AJN, enlarger the hydrodynamic size of AJN. Further TEM-EDS mapping verified the binding of PSS on AJN (Figure 2.8b and c).

The dispersion stability test result is shown in Figure 2.9. The dispersion stability of 0.005 wt% AJN is improved from 6 hours to 48 hours by adding 0.5 wt% or more PSS (Figure 2.9a), and the dispersion stability of 0.01 wt% AJN is improved from 2 hours to 48 hours by adding 0.75 wt% or more PSS (Figure 2.9b). The averaging hydrodynamic size of AJN is larger in brine than that in water (Figure 2.9c, d).

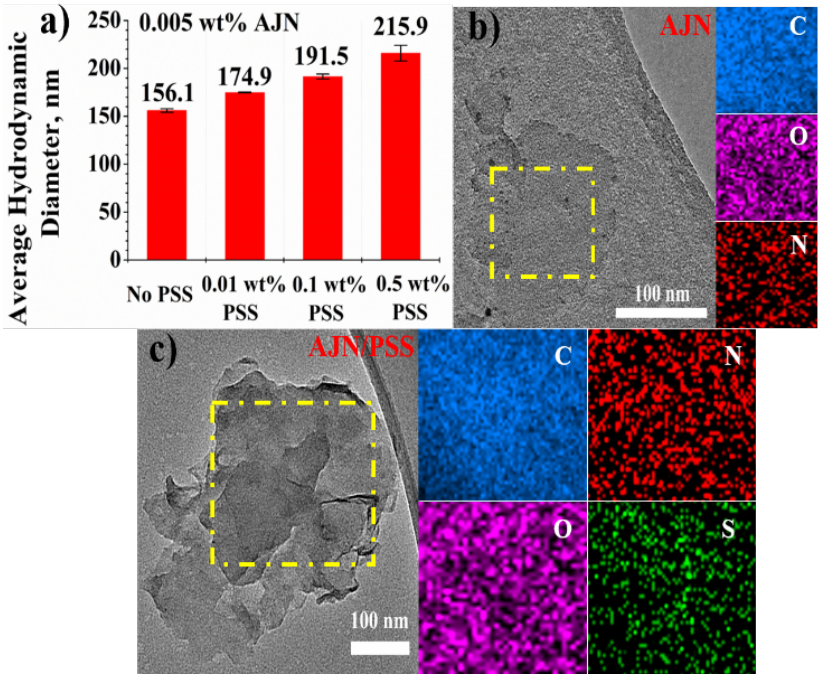

Figure 2.8 Average hydrodynamics diameters and STEM-EDS mapping. **a)** Hydrodynamic diameter measurements of graphene-based amphiphilic Janus nanosheets (AJN) in DI water with increased poly(sodium 4-styrenesulfonate) (PSS) concentrations. STEM-EDS mapping of b) AJN and c) AJN/PSS after several times centrifuge and washing.

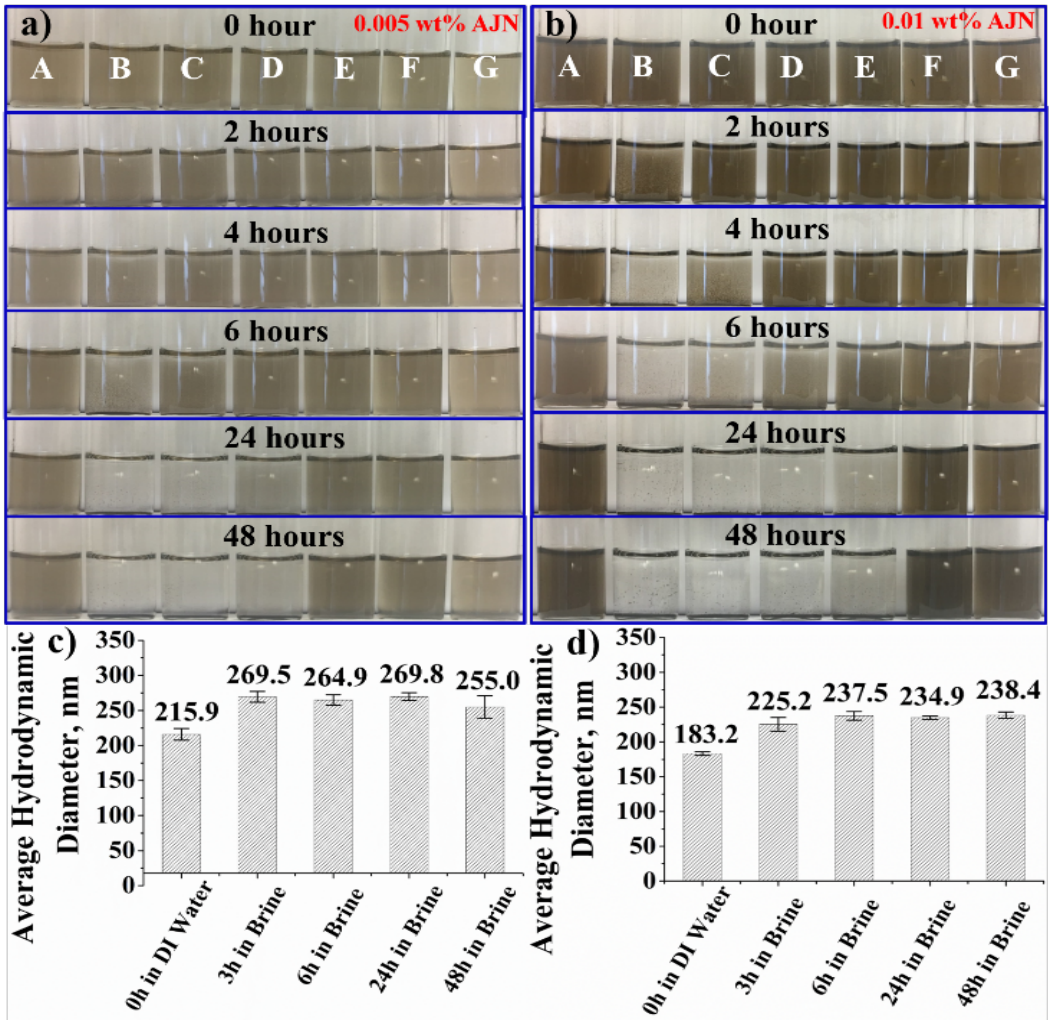

Figure 2.9 Visual stability testing of a) 0.005 wt% and b) 0.01 wt% AJN in brine with different concentration of PSS.
(A: No PSS in DI water; B: 0.01 wt% PSS in brine; C: 0.1wt% PSS in brine; D: 0.25 wt% PSS in brine; E: 0.5 wt% PSS in brine; F: 0.75 wt% PSS in brine; G: 1 wt% PSS in brine). Hydrodynamic diameter measurements of **c)** 0.005 wt% AJN and 0.5 wt% PSS, and **d)** 0.01 wt% AJN and 0.75 wt% PSS in brine.

2.3.5 Conclusions

Molecular dynamics simulation results show (1) PSS molecules bind to AJN surface by van der Waals interactions and hydrophobic interactions in both water and brine; (2) PSS – bonded AJN has a negative charged surface, which prevents the aggregation of AJN and improves the dispersion stability in both water and brine; (3) the existence of ions, especially Ca^{2+}

ions, shield the electrostatic repulsive interactions, reducing the dispersion stability of AJN; (4) the size of AJN-PSS complex should be larger in brine than that in water.

Our experiment results demonstrated the MD simulation results. In summary, PSS is an effective additive to increase the dispersion stability of AJN in brine.

2.4 PSS-bonded AJN in biphasic solution

2.4.1 Molecular dynamics simulation methods

A 24.9 Å × 25.9 Å mono layer graphene with 238 carbon atoms was used as substrate [3]. A 30% oxidized graphene oxide was constructed by attaching 4 carboxyls to the edges, 24 epoxides and 28 hydroxyls to the bottom, top and edges of the substrate graphene. 5 alkylamines were attached to the top side of graphene oxide to construct graphene AJN. 6 sodium 4-styrenesulfonate (SS) units were connected as a poly (sodium 4-styrenesulfonate) (PSS) molecule (Figure 2.2). All of the construction processes were implemented with PyMOL [4]. The charge distribution of PSS was computed with Atomic Charge Calculator [5]. The topology structures were created with TPPmktop [6].

The molecular dynamics simulation was performed using GROMACS 5.1.4 [7]. OPLS-AA force field was used for the simulation. After an energy minimization, the system underwent a 5 ns equilibration at 300 K (NVT ensemble) and a 5 ns equilibration at 1 bar (NPT ensemble), followed by a 100 ns production run. The time step was set to 2 fs. All bond lengths were constrained using the LINCS algorithm. Cut-off of 1.2 nm was used for Lennard-Jones interactions and the real part of the long-range electrostatic interactions, which were calculated using the Particle-Mesh Ewald (PME) method. 0.16 nm grid spacing was used for PME. The information of system was recorded every 100 ps.

The periodic box size was 60 Å × 60 Å × 90 Å. 1 AJN-PSS complex molecule was placed in the center of the box. 444 heptane molecules were distributed on the top 30 Å of the box, forming a heptane layer. 5 PSSs, 84 Na^+ ions, 78 Cl^- ions, 6 Ca^{2+} ions, and 7587 water molecules were randomly distributed in the bottom 60 Å of the box, forming a saline solution layer.

2.4.2 Simulation results

Biphasic solution consists of saline solution with 3% NaCl (wt) and 0.5% $CaCl_2$ (wt) and heptane. The AJN-PSS complex is grabbed from the simulation of AJN with PSSs in brine. AJN is surrounded by 3 PSSs (Figure 2.10A). In the beginning configuration, the plane of graphene sheet was perpendicular to the interface of heptane and brine. After a 5 ns simulation, 2 PSS molecules on the top side of AJN moved away and bond with heptane, exposing the hydrophobic carbon chain to the saline solution. The hydrophobic interactions drove AJN to the heptane layer. Just like nails, carbon chains screwed into heptane layer. PSS molecules were also distributed in the interface between heptane and water (Figure 2.10B). There is no significant difference in the dispersion process and rate at 300 K and 343 K.

The existence of alkylamines on AJN increases the binding surface of AJN with heptane significantly (Figure 2.11). The surface area of substrate graphene for a single side is 6.5 nm^2 and the contact interface area between AJN and heptane is 30 nm^2, which means attached alkylamines on the top side of AJN increases the contact area with heptane by 4 times. The major interactions between AJN and heptane are hydrophobic interactions and van der Waals interactions, which are positively related to the area of contact interface. Larger contact area also reflects greater interaction strength. Hence, AJN can contact with heptane firmly in the biphasic interface.

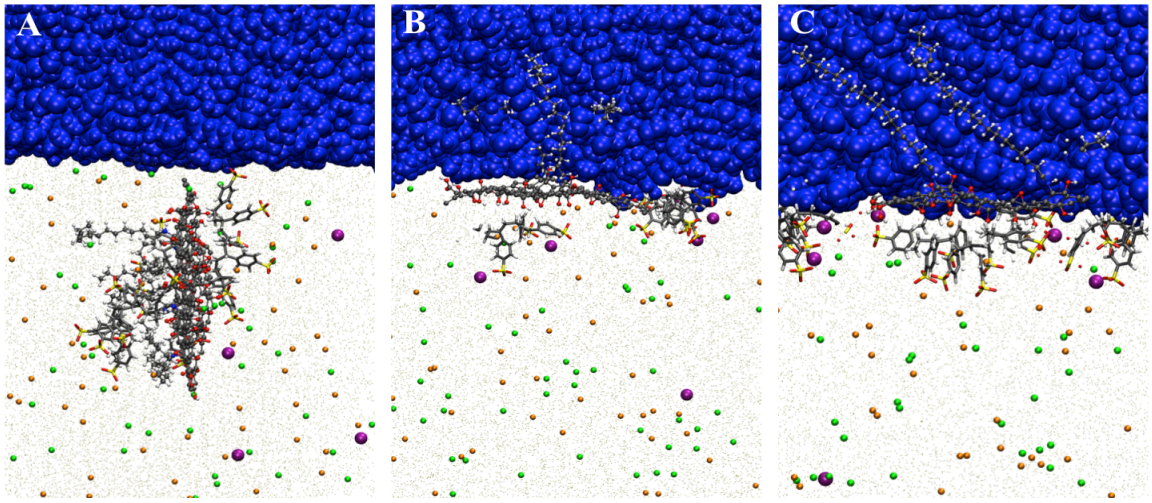

Figure 2.10 Simulation of AJN-PSS complex in biphasic solution.
Blue spheres in the top represent heptane layer. Tan dots in the bottom represent water molecules. AJN and PSS are represented by sticks. Orange beads are Na^{+} ions, green beads are Cl^{-} ions, and purple beads are Ca^{2+} ions. Panel A shows the beginning configuration. Panel B illustrates the cross-section of final configuration after 100 ns simulation at 300K. Panel C shows the cross-section of final configuration after 100 ns simulation at 343K.

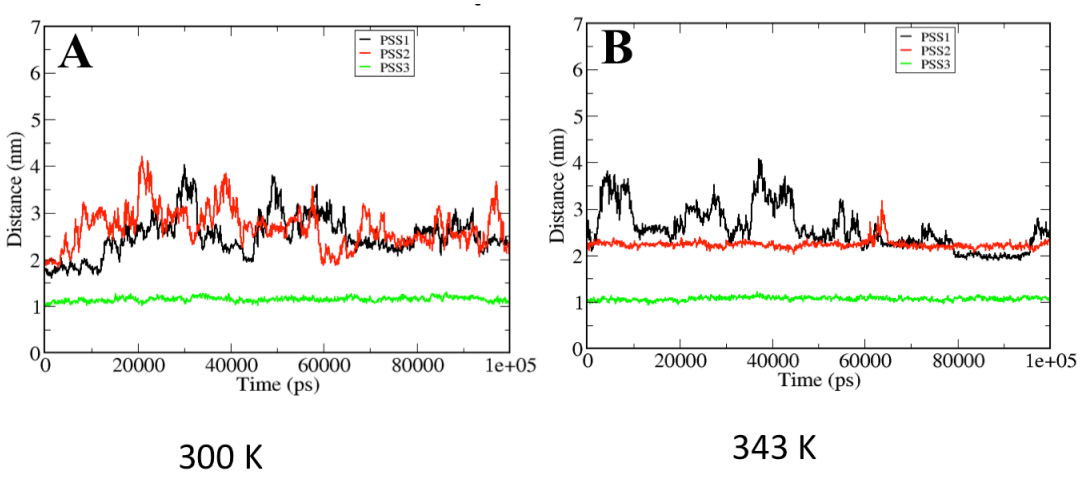

Figure 2.11 Center of mass (COM) distance between 3 PSS molecules and AJN .

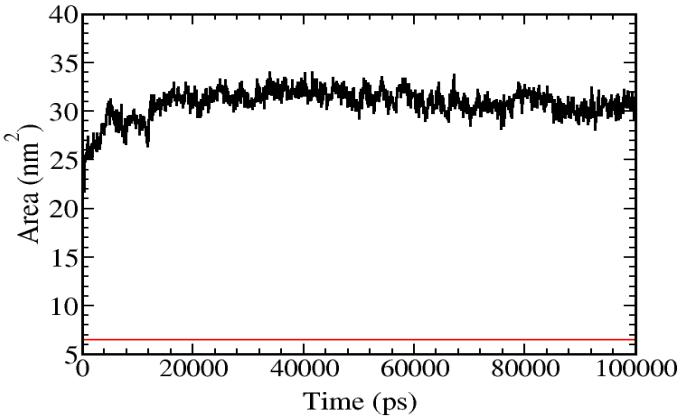

Figure 2.12 Contact surface area of AJN with heptane.
The black line is contact surface area of AJN with heptane, and the red line is the rectangle area of the graphene sheet. Attached carbon chain on the top side of AJN increases the contact area with heptane by 4 times.

2.4.3 Experiment results

Without AJN in the interface of heptane and brine, the interface is a concave because of interfacial tension (Figure 2.13A). Interfacial tension reduces when AJN is distributed on the interface, resulting in a flat interface (Figure 2.13B and C). As shown in Figure 2.13, PSS-bonded AJN succeeded to move from brine to the heptane-brine interface by shaking. Shaking produced many droplets. The deforming process is accelerated when the temperature increases to 70 ^{o}C.

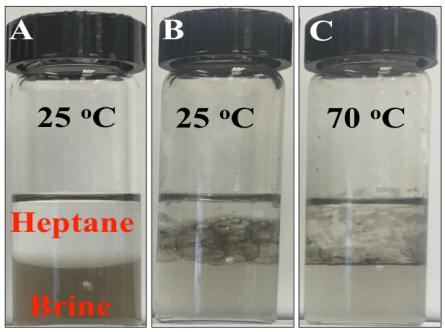

Figure 2.13 AJN/PSS mixture in heptane/brine system.
(A) Initial state before shaking at 25 ^{o}C. (B) After shaking at 25 ^{o}C. (C) After shaking at 70 ^{o}C.

2.4.4 Conclusions

Molecular dynamics simulation results show that PSS-bonded AJN would move to the heptane-brine interface. As the hydrophobic interactions and van der Waals interactions between heptane and PSS are greater than that between AJN and PSS, PSS molecules that bonded to the carbon chains would fall off and bind to heptane. The amphiphilic property of AJN can be retained in the interface and reduce the interfacial tension.

Experiments results demonstrate that AJN's amphiphilic property could be retained by shaking. High temperature would help to deform droplets.

2.5 Synthesis of AJN with starch

As we mentioned in previous sections, the application of AJN with PSS is a promising in crude recovery. Here we reported a scalable and economical approach for AJN synthesis with graphene oxide and starch. As shown in Figure 2.14, by simply mixing GO and tapioca starch microspheres in water for a few hours at room temperature, GO is immobilized on the surface of tapioca starch microspheres (molecule formula $(C_6H_{10}O_5)_n$). After successive washing with water and ethanol, the single-side surface hydrophobization of GO was conducted with alkylamine in ethanol at room temperature. After washing, AJN was released from the starch microspheres by sonication and heating in ethanol. The mixture separated into two phases, with starch microspheres at the bottom portion and AJN dispersed in ethanol at the upper portion.

The mechanism of why GO is immobilized on the surface of tapioca starch microspheres is remained to be answered. Here we applied molecular dynamics simulation to explore the interactions on the interface of starch microspheres and GO.

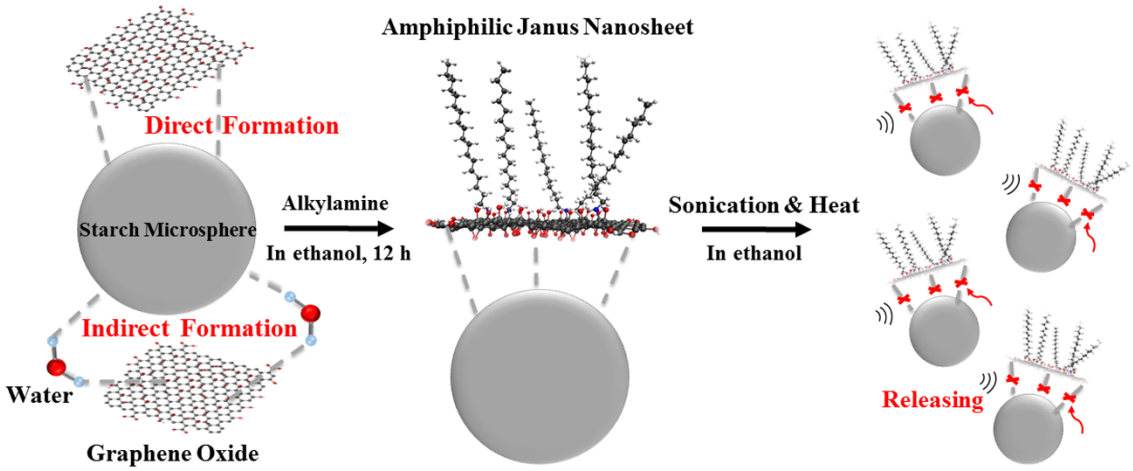

Figure 2.14 Schematics of AJN synthesis with starch and graphene oxide.

2.5.1 Molecular dynamics simulation methods

A 24.9 Å × 25.9 Å mono layer graphene with 238 carbon atoms was used as the substrate. A 30% oxidized graphene oxide was constructed by attached 4 carboxyls, 24 epoxides, and 28 hydroxyls to the substrate graphene. The structure of starch molecule was downloaded from Protein Data Bank (ID: 4BFN) with a molecule formula $(C_6H_{10}O_5)_4$. The topology structures were created with TPPmktop [6].

The molecular dynamics simulation was performed using GROMACS 5.1.4 [7]. OPLS-AA force field was used for the simulation. A graphene oxide molecule was placed in the center of 6 nm × 6 nm × 6 nm box. 6 starch molecules and 6810 water molecules were randomly distributed in the box. After an energy minimization, the system underwent a 10 ns production simulation at 300 K and 1 bar. The time step was set to 2 fs. The information of system was recorded every 100 ps. All bond lengths were constrained using the LINCS algorithm. Cut-off of 1.2 nm was used for Lennard-Jones interactions and the real part of the long-range electrostatic interactions, which were calculated using the Particle-Mesh Ewald (PME) method. 0.16 nm grid spacing was used for PME.

2.5.2 Simulation results

In the molecular dynamics simulation, we found that graphene oxide binds to starch molecules in a short time (less than 1 ns). Given the contact area between them is small, the van der Waals interactions and hydrophobic interactions should be weak. Abundant in oxygen, it's effortless for GO and starch to form hydrogen bonds. Hydrogen bonds serve as the dominant interactions between GO and starch. Hydrogen bonds are much stronger than van der Waals interactions and hydrophobic interactions, which explained why GO is immobilized on the surface of tapioca starch microspheres.

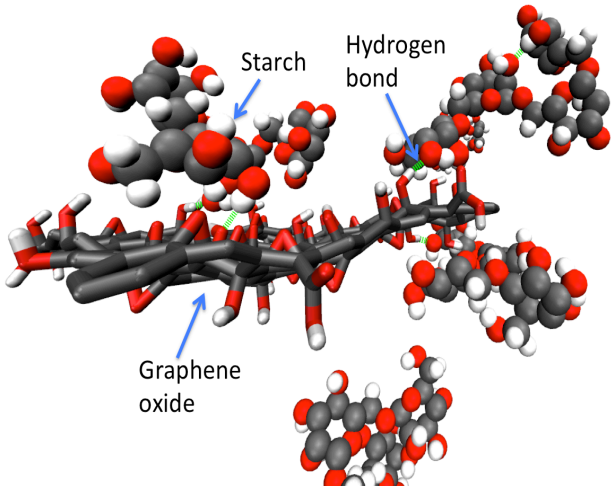

Figure 15 Molecular dynamics simulation of graphene oxide with starch molecules.
Starch molecules are represented by beads. Oxygen atoms are in red, carbon atoms are in grey, and hydrogen atoms are in white. The green dotted lines represent hydrogen bonds.

2.5.3 Conclusions

In summary, a more efficient method to synthesize graphene-based amphiphilic Janus nanosheets has been found. With the help of molecular dynamics simulation, we found that the formation of hydrogen bonds immobilized GO on the surface of tapioca starch microspheres for

subsequent hydrophobization using alkylamine. By breaking the hydrogen bonding, amphiphilic Janus nanosheets were released from the surfaces. This method is highly facile and scalable. In comparison with the previous wax-in-water emulsion template masking method [2], there is no need to dissolve wax templates with large amounts of organic solvents, supporting economical production at large scale.

2.6 References

1. Raffa, P., A.A. Broekhuis, and F. Picchioni, *Polymeric Surfactants for Enhanced Oil Recovery: A Review.* Journal of Petroleum Science and Engineering, 2016. **145**: p. 723-733.

2. Luo, D., F. Wang, J. Zhu, F. Cao, Y. Liu, X. Li, R.C. Willson, Z. Yang, C.W. Chu, and Z. Ren, *Nanofluid of Graphene-Based Amphiphilic Janus Nanosheets for Tertiary or Enhanced Oil Recovery: High Performance at Low Concentration.* Proceedings of the National Academy of Sciences (PNAS), USA, 2016. **113**(28): p. 7711-6.

3. Li, J. and F. Wang, *Water Graphene Contact Surface Investigated by Pairwise Potentials from Force-Matching Paw-Pbe with Dispersion Correction.* The Journal of Chemical Physics, 2017.

4. *The Pymol Molecular Graphics System, Version 1.7.4 Schrödinger, Llc*.

5. Ionescu, C.-M., D. Sehnal, F.L. Falginella, P. Pant, L. Pravda, T. Bouchal, R.S. Vařeková, S. Geidl, and J. Koča, *Atomicchargecalculator: Interactive Web-Based Calculation of Atomic Charges in Large Biomolecular Complexes and Drug-Like Molecules.* Journal of Cheminformatics, 2015. **7**(1): p. 50.

6. TPPmktop. Available from: http://erg.biophys.msu.ru/tpp/.

7. Abraham, M.J., T. Murtola, R. Schulz, S. Páll, J.C. Smith, B. Hess, and E. Lindahl, *Gromacs: High Performance Molecular Simulations through Multi-Level Parallelism from Laptops to Supercomputers.* SoftwareX, 2015. **1**: p. 19-25.

8. Jorgensen, W.L., D.S. Maxwell, and J. Tirado-Rives, *Development and Testing of the Opls All-Atom Force Field on Conformational Energetics and Properties of Organic Liquids.* Journal of American Chemical Society (JACS), 1996. **118**(45): p. 11225-11236.

9. Eisenhaber, F., P. Lijnzaad, P. Argos, C. Sander, and M. Scharf, *The Double Cubic Lattice Method: Efficient Approaches to Numerical Integration of Surface Area and Volume and to Dot Surface Contouring of Molecular Assemblies.* Journal of Computational Chemistry, 1995. **16**(3): p. 273-284.

10. Schniepp, H.C., J.-L. Li, M.J. McAllister, H. Sai, M. Herrera-Alonso, D.H. Adamson, R.K. Prud'homme, R. Car, D.A. Saville, and I.A. Aksay, *Functionalized Single Graphene Sheets Derived from Splitting Graphite Oxide.* The Journal of Physical Chemistry B, 2006. **110**(17): p. 8535-8539.

11. Kumar, H.V., S.J. Woltornist, and D.H. Adamson, *Fractionation and Characterization of Graphene Oxide by Oxidation Extent through Emulsion Stabilization.* Carbon, 2016. **98**: p. 491-495.

12. Wu, H., W. Yi, Z. Chen, H. Wang, and Q. Du, *Janus Graphene Oxide Nanosheets Prepared Via Pickering Emulsion Template.* Carbon, 2015. **93**: p. 473-483.

13. Hong, L., S. Jiang, and S. Granick, *Simple Method to Produce Janus Colloidal Particles in Large Quantity.* Langmuir, 2006. **22**(23): p. 9495-9499.

14. Marcano, D.C., D.V. Kosynkin, J.M. Berlin, A. Sinitskii, Z. Sun, A. Slesarev, L.B. Alemany, W. Lu, and J.M. Tour, *Improved Synthesis of Graphene Oxide.* ACS Nano, 2010. **4**(8): p. 4806-4814

Chapter 3 Degradation of carbon nanotube in vivo

A part of this chapter contains our previous published works:

1. Ding, Y., Tian, R., Yang, Z., Chen, J., & Lu, N. (2016). Binding of human IgG to single-walled carbon nanotubes accelerated myeloperoxidase-mediated degradation in activated neutrophils. Biophysical Chemistry, 218, 36-41.

2. Ding, Y., Tian, R., Yang, Z., Chen, J., & Lu, N. (2017). Effects of serum albumin on the degradation and cytotoxicity of single-walled carbon nanotubes. Biophysical chemistry, 222, 1-6.

3. Ding, Y., Tian, R., Yang, Z., Chen, J., & Lu, N. (2017). NADPH oxidase-dependent degradation of single-walled carbon nanotubes in macrophages. Journal of Materials Science: Materials in Medicine, 28(1), 7.

3.1 Introduction

The biotechnological and biomedical applications of carbon nanotubes (CNTs) have raised large concerns about their possible adverse effects on human health. Many in vivo and in vitro studies have indicated that CNTs can develop an inflammatory response and may be cytotoxic[1-4]. Due to their chemically inert and stable abilities, CNTs are accumulated in vivo and hardly to be cleared; hence, biopersistence of CNTs is one of the major stumbling blocks on the way of CNTs' broad biomedical applications. Studies on the biocompatibility and biodegradative mechanism of CNTs are of great importance in nanomedicine [5].

Apart from the chemical degradation of CNTs by strong acids and oxidants, enzymatic oxidative degradation of CNTs was demonstrated in recent years using heme peroxidases, such as horseradish peroxidase (HRP) and human myeloperoxidase (MPO) [6-9]. The carboxylated

single-walled CNTs (SWCNTs) can be degraded by peroxidase activity of these heme proteins in the presence of low concentrations of hydrogen peroxide (H_2O_2). The interaction of active heme with H_2O_2 leads to the formation of peroxidase reactive intermediates, which can effectively oxidize CNTs [8, 9]. The degradation of CNTs into short fragments (such as short-chain carboxylated alkanes and alkenes) can decrease their toxicity and accelerate their clearance from the body [9]. Enzymatic degradation of CNTs proceeds to a high extent only if pristine CNTs have defect sites (such as carboxylic groups) on the graphitic surface.

As one of the major human peroxidases, MPO is abundantly expressed in neutrophils that play a crucial role in the principal defense mechanisms of innate immunity [10, 11]. In addition to its role in the peroxidase cycle, MPO possesses a unique chlorinating to catalyze the oxidation of Cl^- to produce hypochlorite (OCl^-) [10]. Both reactive radical intermediates of MPO and OCl^- are the oxidants involved in the degradation process of SWCNTs in vitro and in vivo [9, 12]. It was demonstrated that oxidation and clearance of SWCNTs from the lungs of MPO-deficient mice after pharyngeal aspiration was markedly less effective whereas the inflammatory response was more robust than in wild-type animals [12], providing direct evidence for the dominant participation of MPO in the in vivo biodegradation of CNTs.

During the interactions with components of biofluids in vivo, non-covalent coating of SWCNTs with proteins will inevitably affect recognition patterns, metabolic pathways, and toxicity of the nanomaterials [13, 14]. It has been reported that the binding of human serum proteins to CNTs can significantly alter their cellular interaction pathways and sharply reduces their cytotoxicity[15, 16]. Interactions of CNTs with bovine serum albumin (BSA) can enhance their biocompatibility, and the BSA-dispersed SWCNTs can be uptaken by various cells without any apparent deleterious cellular effects[17]; hence, the nature of the nanomaterial ‘coronation’ by human proteins may impact its degree of recognition and biodegradation by immune cells. As the second most abundant protein in human blood plasma and extracellular fluid,

immunoglobulin G (IgG) is an antibody isotype vital for immune system function [18-20]. It is responsible for the primary defense in humans when external antigenic compounds invade the body. Here, it coats the pathogen surfaces (opsonization) allowing their recognition and phagocytosis, binds pathogens resulting in their immobilization and agglutination, activates the classical pathway of the complement system, and binds and neutralizes toxins [20]. Despite its role in the immune system and importance in many medical applications, IgG is rarely used as a model protein in protein-SWCNTs interactions.

Although the interactions between proteins and CNTs are believed to play an important role in the biological effects of CNTs [15-17], no previous efforts have been made to demonstrate that the IgG-SWCNTs interactions would influence the biodegradation of nanotubes. In this study, we employed both theoretical and experimental approaches to investigate human IgG–SWCNTs interactions. Through the competitive binding to nanotubes, the binding of IgG could impair MPO-induced SWCNTs biodegradation in vitro; however, the binding of IgG to SWCNT could enhance cellular uptake of nanotubes and stimulate MPO release and OCl^- formation in neutrophils, thereby promoting their degradation. The current work demonstrates that the binding of IgG may be an major determinant for MPO-mediated SWCNTs biodegradation in activated human inflammatory cells; therefore, functionalization of SWCNTs by IgG aimed to target them to immune cell may provide a good platform to improve the biodegradation and biocompatibility of nanotubes in vivo.

3.2 Computational modeling and docking

3.2.1 Methods and materials

The three-dimensional structures of nanotubes were generated using Nanotube Modeller software with chirality parameters m = 14 and n = 0. The diameter of CNT was 1.1 nm [9]. The

CNT was carboxylated on one ending by the Builder tool in Pymol visualization software [21]. CNT was docked to the X-ray crystal structure of BSA (PDB ID 3V03) and IgG (PDB ID 1IGT) using the Lamarckian Genetic Algorithm provided by AutoDock4.2 software. The receptor (BSA and IgG) was placed in the center of the box. The box size was 88 × 58 × 72 points for BSA and 104 × 126 × 126 points for IgG with a spacing of 1 Å between the grid points. The receptor's grid maps were calculated by AutoGrid first. The value of ga_run was set 1000. That means 1000 trials were ran to find the best binding pose.

3.2.2 Binding interface of BSA with SWCNT

Molecular docking studies were performed using AutoDock 4.2 software to structurally characterize possible SWCNTs interaction sites on BSA. The docking of oxidized SWCNTs to BSA indicates the most preferred binding site on proteins for SWCNTs. The predicted binding energy was -9.83 kcal/mol. Residue LYS64, CYS75, ALA78, ARG81, GLU82, CYS91, and GLN94 are included in the binding pocket (Figure 3.1B) and predict to stabilize the interaction between SWCNTs and BSA.

Various weak interactions may contribute to protein adsorption on CNTs, such as π-π stacking, hydrophobic interactions, and electrostatic interactions [15, 16]. Our simulations reveal that polar residues, e.g., two cysteines (CYS75, CYS91) and GLN94, seem to have significant contributions to the binding of proteins onto CNTs (Figure 3.1B). Based on previous studies [15, 16, 22] and results herein, it can be demonstrated that these hydrophilic residues contact SWCNTs via their nonpolar aliphatic chain, whereas the polar groups are pointing out to the water, further indicating that the hydrophobic interaction serves as one of driving forces in the protein–CNTs binding. Also, the oxidized groups (carboxyl) on SWCNTs in the binding site are stabilized by electrostatic interaction with the positively charged residue ARG81 on BSA (Figure 3.1B); therefore, these theoretical results herein illustrate that besides of the widespread π-π

stacking interactions [16], the hydrophobic interactions between SWCNTs and polar residues (CYS, GLN) in BSA and electrostatic interaction of positively charged ARG residue with carboxyls on SWCNTs might be the crucial factors in stabilizing the binding of carboxylated SWCNTs with BSA.

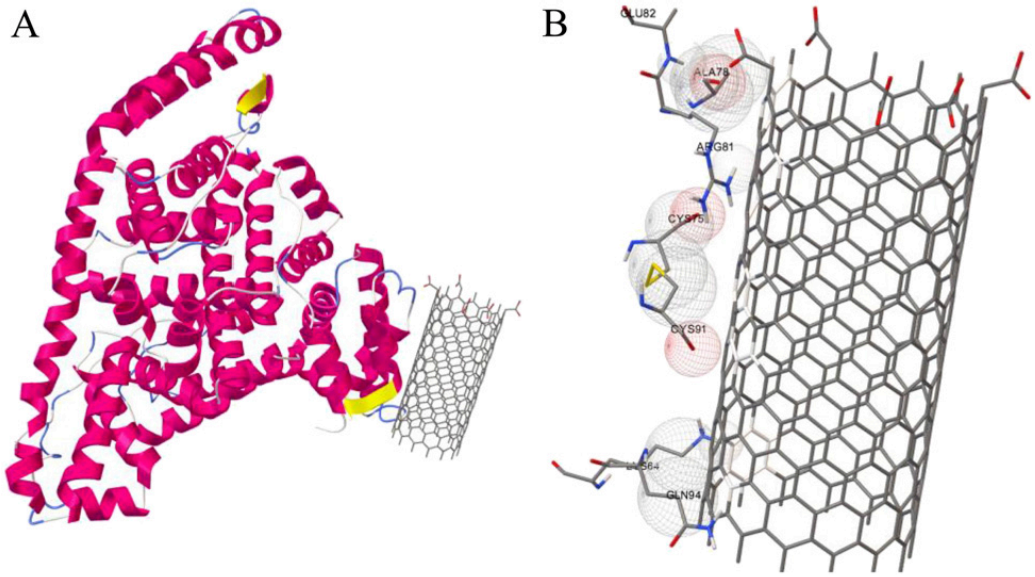

Figure 3.1 Binding interface of BSA with SWCNT.
(A) The predicted binding interface of BSA and SWCNT. The binding energy is -9.83 kcal/mol. (B) The detail of binding interface, which includes LYS64, CYS75, ALA78, ARG81, GLU82, CYS91, and GLN94. The red grid spheres represent negative-charged atoms, and the blue grid spheres represent positive-charged atoms.

3.2.3 Binding interface of IgG with SWCNT

Molecular docking studies were performed using AutoDock 4.2 software to structurally characterize possible SWCNTs interaction sites on IgG. The docking of oxidized SWCNTs to IgG indicates the most preferred binding site on proteins for SWCNTs. The predicted binding energy is -15.93 kcal/mol, which is much stronger the binding of BSA and SWCNT. The best binding of CNT is located in the region of the F_c fragment of IgG (Figure 3.2A). Residue

GLN287, THR303, GLN305, GLN307, THR308, ARG310, and LYS345 are included in the binding pocket (Figure 3.2B) and predict to stabilize the interaction between SWCNTs and IgG.

Firstly, the oxidized groups (carboxyl) on SWCNTs in the binding site are supported by electrostatic interactions with these positively charged residues, ARG310 and LYS345 on IgG (Figure 3.2B). The similar electrostatic interactions with SWCNTs were observed for HSA and MPO, both of that the interactions were related to the positively charged ARG residues (such as Arg 160 for HSA [21], ARG 294, ARG 307, ARG 507 for MPO [9]). Also, the binding might be related to the hydrophobic interactions since the SWNTs sidewalls are not fully oxidized and contain hydrophobic regions. Our simulations reveal that polar residues, e.g., three glutamines (GLN287, GLN305, GLN307) and two threonines (THR303, THR308) in F_c domain, seem to have significant contributions to the strong binding of proteins onto CNTs (Figure 3.2B). Based on previous studies [15, 16] and results herein, it could be demonstrated that these hydrophilic residues contacted SWCNT via their nonpolar aliphatic chain, whereas the polar groups are pointing out to the water, further indicating that the hydrophobic interaction served as one of driving forces in the protein–CNT binding; therefore, these theoretical results herein illustrate that the electrostatic interaction of positively charged residues (ARG, LYS) with carboxyls on SWCNTs and hydrophobic interactions between SWCNTs and polar residues (GLN, THR) in IgG might be the crucial factors in stabilizing the binding of carboxylated SWNTs with IgG.

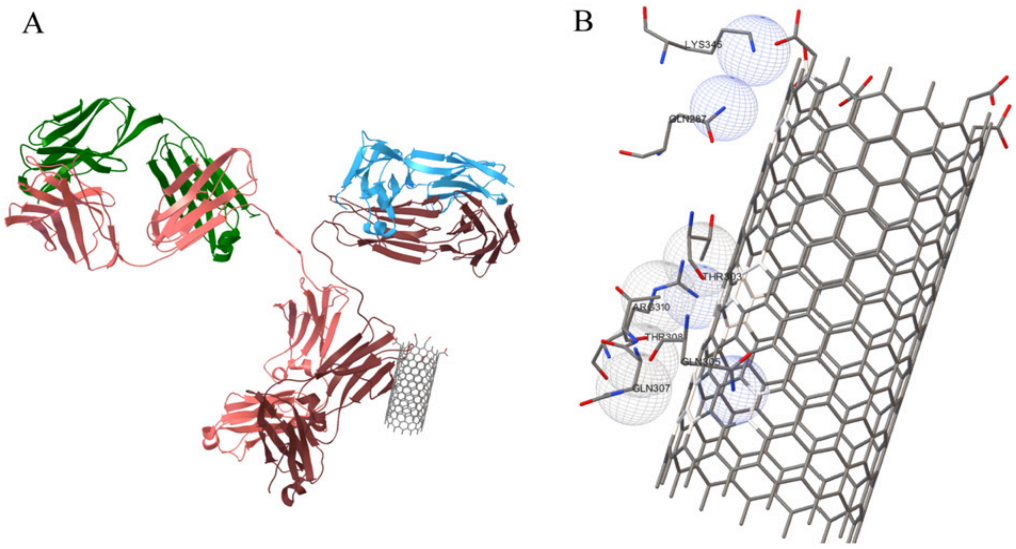

Figure 3.2 Binding interface of IgG with SWCNTs.
(A) The predicted binding interface of IgG and SWCNT. The binding energy is -15.93 kcal/mol. (B) The detail of binding interface, which includes GLN287, THR303, GLN305, GLN307, THR308, ARG310, and LYS345 The red grid spheres represent negative-charged atoms, and the blue grid spheres represent positive-charged atoms.

3.2.4 Binding interface of MPO with SWCNT

Molecular docking studies were performed using AutoDock 4.2 software to characterize possible SWCNTs interaction sites on MPO structurally. The predicted binding energy is -15.49 kcal/mol, which is much stronger than the binding of BSA. Figure 3.3A illustrates the binding configuration of SWCNT with MPO. Residue LYS308, GLY441, ARG314, SER315, GLN444, GLU446, and GLN450 are included in the binding pocket (Figure 3.3B) and are predicted to stabilize the interactions between SWCNTs and MPO.

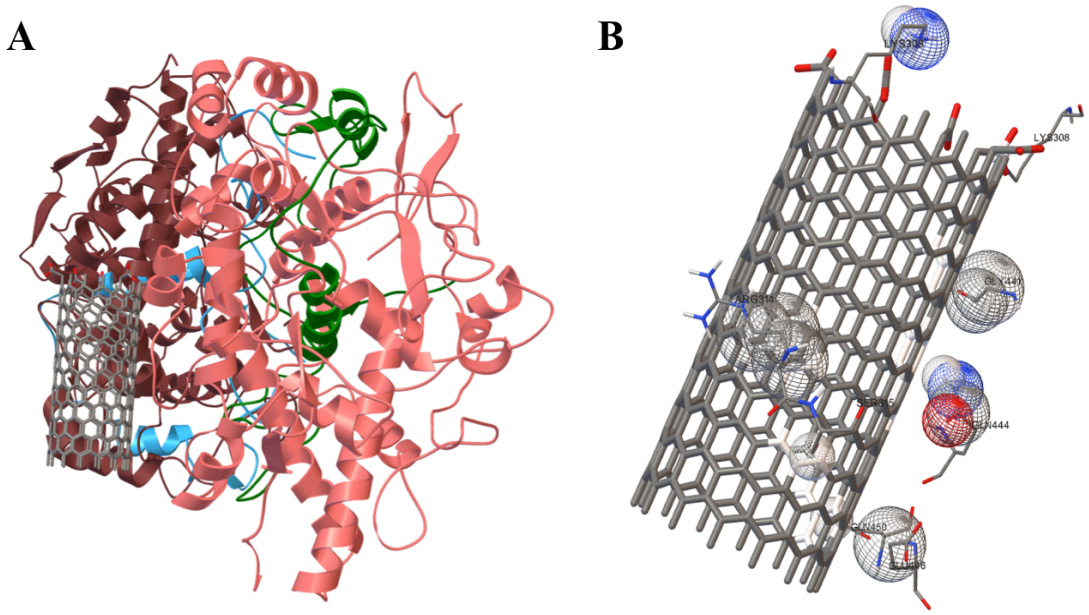

Figure 3.3 Binding interface of MPO with SWCNT.
(A) The predicted binding interface of MPO and SWCNT. The binding energy is -15.43 kcal/mol. (B) The detail of binding interface, which includes LYS308, GLY441, ARG314, SER315, GLN444, GLU446, and GLN450. The red grid spheres represent negative-charged atoms, and the blue grid spheres represent positive-charged atoms.

3.2.5 Conclusions of docking

SWCNT has the similar binding site and binding mechanism with BSA, MPO, and IgG. Electrostatic interaction of positively charged residues (ARG, LYS) with carboxyls on SWCNTs and hydrophobic interactions between SWCNTs and polar residues in IgG are the crucial factors in stabilizing the binding of carboxylated SWNTs with protein. SWCNT is appropriate to bind with BSA, MPO, and IgG, however, the binding energies are -9.83 kcal/mol, -15.43 kcal/mol, and -15.93 kcal/mol, respectively. The binding strength of MPO and IgG are much stronger than BSA, and the binding strength of IgG (-15.93 kcal/mol) is comparable to MPO (-15.43 kcal/mol). SWCNT is more likely to bind with IgG, which is verified by our experiment.

3.3 Experimental section

3.3.1 Methods and materials

Single-walled carbon nanotubes (SWCNTs) (purity > 90%, outer diameter: 1-2 nm, length: 0.5-2 μm) were purchased from XF NANO (China). IgG from human serum, zymosan, human myeloperoxidase (MPO), and sodium hypochlorite (NaOCl) was purchased from Sigma-Aldrich. Carboxylated single-walled carbon nanotubes (SWCNTs) were prepared and used throughout the study unless specified otherwise.

SWCNTs (0.2 mg/ml) in PBS (20 mM, pH 7.4) were incubated with IgG in 1:1 ratio (w/w) for 1 h at 37 °C with sonication for 2 min every 15 min.

SWCNTs and IgG-SWCNTs (0.1 mg/ml) were incubated with human MPO in PBS (20 mM) containing NaCl (140 mM) and diethylene triamine pentaacetic acid (DTPA, a transition metal chelator, 100 μM). Hydrogen peroxide (H_2O_2) was added at a rate of 400 μM per 12 h [9]. Because of the loss of MPO activity and IgG in the incubation system, the enzyme and IgG were replenished after 24 h, and the reaction mixture was maintained at 37 ^{o}C for 48 h. Where indicated, IgG was incubated with SWCNTs before MPO addition.

Cells were incubated with either serum-opsonized zymosan (SOZ) or nanotubes for 30 min; then, neutrophils were centrifuged, and the obtained supernatant was used for MPO and OCl^- measurements according to previous studies [7, 9].

3.3.2 IgG binds with SWCNTs

Transmission electron microscopy (TEM) and circular dichroism (CD) spectra were further applied to monitor interactions between IgG and SWCNTs. TEM image of SWCNTs incubated with IgG revealed the formation of a ‘protein corona’ on the nanotube surface (Figure 3.3 C). The IgG molecule could spontaneously bind to the surface of SWCNTs in a non-uniform

form. After 30 min incubation, the CD spectrum showed that SWCNTs induced a decrease in the β-structure composition of IgG. These results indicated that the non-uniform adsorption of IgG on SWCNTs caused significant changes in the protein secondary structures.

To confirm the findings mentioned above, we attempted to semi-quantitatively analyze protein adsorption by SDS-PAGE and quantify the binding of IgG to SWCNTs, and further confirmed the strong binding of IgG to SWCNTs. Adsorbed proteins released from SWCNT were analyzed. After 10 min of incubation, the band intensity of the protein rapidly changed from light to dark, which indicated that protein content in the sediment became much bigger due to protein adsorption onto SWCNT molecules. The protein-binding capacity of SWCNTs at 60 min was 0.52±0.01 mg IgG per mg of SWCNTs, much higher than the MPO-binding capacity of SWCNTs (0.18±0.02 mg per mg of nanotubes) [6]. These different protein-binding capacities were possibly related to the characteristics of protein and the various numbers of protein molecules on top of SWCNTs. The characteristic folds in IgG are grouped in different segments, two identical F_{ab} segments connected via the hinge region to one F_c segment, thus forming a Y-shaped conformation [23]. IgG exhibiting considerable segmental flexibility from the Y-shaped structure was more accessible to binding onto SWCNT surface. Although the similar molecular weights were present for IgG (~148 kDa) and MPO (~144 kDa), the numbers of each protein binding to SWCNT surfaces were about three and two molecules on average for Ig [16], and MPO [9], respectively, which seemed to show a positive correlation to the larger adsorption capacity of IgG on the nanotube surface. This result is consistent with our docking result.

3.3.3 Binding of IgG to SWCNTs reduced biodegradation in vitro

Then, MPO-mediated SWCNTs biodegradation was studied. The degradation degree could be estimated on the basis of the absorption intensity at λ=1060 nm, which was considered as the characteristic of semiconducting transition band in CNTs. It was previously demonstrated

that this intensity gradually decreased as degradation of SWCNTs progressed [6, 9]. Figure 3.4A showed that all of MPO/H_2O_2, MPO/H_2O_2/Cl^- and NaOCl could effectively oxidize SWCNTs. Moreover, the D-band in the Raman spectra corresponded to defects in the CNT wall and the ratio of this to the G-band (I_D/I_G ratio) was used to monitor the integrity of SWCNTs [7, 9]. The I_D/I_G ratio increased from 0.07 at the beginning to 0.14 as a result of SWCNT degradation by MPO/H_2O_2/Cl^- system (Figure 3.4B). Changes in nanotube morphology were further confirmed by TEM. The fibrillar structure of intact nanotubes was lost, and the shortened nanotubes were present (Figure 3.4C). These results suggested that SWCNTs were oxidized and degraded during their incubation with MPO/H_2O_2/Cl^- system, which was consistent with previous studies [6-9].

To investigate the effect of IgG on nanotube degradation, IgG was sufficiently incubated with SWCNTs for 1 h to form IgG-absorbed SWCNTs (IgG-SWCNTs). After the binding of IgG to nanotubes, IgG-SWCNTs were also significantly oxidized by MPO/H_2O_2/Cl^- and the degradation showed a slower rate than unbounded SWCNTs (Figure 3.4); therefore, the binding of IgG could effectively impair MPO-catalysed biodegradation of SWCNTs in vitro.

Previous studies have suggested that carboxyl groups on SWCNTs are found to play a critical role in biodegradation, and the direct interactions of MPO with SWCNTs are present during the biodegradation process [9]. Considering the fact that IgG was more accessible than MPO to binding onto SWCNT surface, the reduced effect of binding of IgG on MPO-induced SWCNTs biodegradation was mainly due to the competitive binding of IgG and MPO to nanotube surfaces; however, the presence of reactive intermediates of MPO and OCl^- would oxidize proteins and successively strip the protein from CNTs [7]; therefore, MPO system could damage and peel off IgG from the surface of SWCNTs, and subsequently degrade nanotubes. On the other hand, IgG could be considered as a competitive substrate for MPO-induced oxidants and effectively protect the surfaces of nanotubes from the direct exposure of oxidants, thus exhibiting a protective effect on oxidative degradation of SWCNTs.

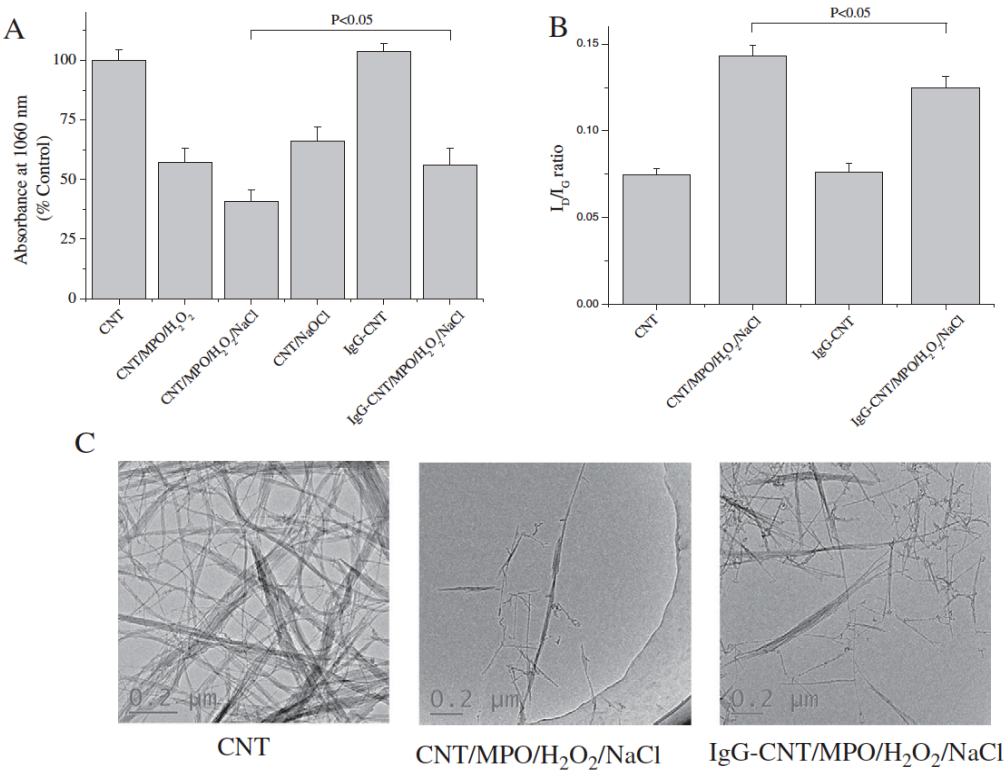

Figure 3.4 Binding of IgG to SWCNTs reduced MPO-mediated degradation of nanotubes in vitro.
(A) Effects of MPO and NaOCl on the degradation of SWCNTs. The absorbance of SWCNTs at 1060 nm could be used to measure the degradation of SWCNTs. (B) D/G intensity ratios obtained from Raman spectroscopy on SWCNTs, showing the defects on the walls of SWCNTs ($P<0.05$, groups versus indicated group). (C) TEM analyses track the biodegradation of nanotubes.

3.3.4 Binding of IgG to SWCNTs accelerated biodegradation in neutrophils

The present results above provided the effect of the binding of IgG on MPO-induced SWCNTs degradation in vitro; then, we carried out an additional experiment exploring whether the binding of IgG influenced the biological action of SWCNTs in human blood neutrophils. Both MPO and OCl^- are generated upon activation of neutrophils [9]. As shown in Figure 3.5A and B, SWCNTs exhibited no significant effect on neutrophils concerning the generation of MPO and OCl^-. In contrast, a slightly stimulatory effect of IgG-SWCNTs on these cells was observed,

which was based on the elevated MPO level, OCl^-, superoxide radicals ($O_2^{\cdot -}$) and H_2O_2 formation from neutrophils. Probably due to the low levels of MPO and OCl^-, biodegradation of SWCNTs and IgG-functionalized nanotubes did not occur during their incubation in nonactivated neutrophils (Figure 3.6A).

Next, we evaluated whether SWCNTs biodegradation could proceed in MPO-rich neutrophils upon activation. Stimulation of neutrophils was then performed using serum-opsonized zymosan (SOZ), which was known to effectively trigger MPO release in human neutrophils [7, 12]. During neutrophil activation by SOZ, these marked elevations on the release of MPO and generation of OCl^-, $O_2^{\cdot -}$, and H_2O_2 were observed in human neutrophils (Figure 3.5). Under these stimulated conditions, IgG–SWCNTs underwent more significant degradation than that of non-IgG-functionalized nanotubes in neutrophil (Figure 3.6B), where an increase in I_D/I_G ratio was characteristic of oxidatively modified nanotubes. Inhibitors of MPO (4-aminobenzoic acid hydrazide) and NADPH oxidase (apocynin) attenuated the oxidative degradation process. This result suggested that both MPO and NADPH oxidase were essential for SWCNTs biodegradation by human neutrophils. During neutrophil activation, NADPH oxidase generates $O_2^{\cdot -}$ [9]. The latter dismutates to H_2O_2, which enables MPO to produce reactive intermediates and OCl^- locally, thus providing a necessary condition for the biodegradation of nanotubes. This discovery of enzymatic SWCNTs degradation in activated neutrophils will also open new opportunities for the regulation of CNTs fate in vivo by controlling inflammatory response and employing nanotube-metabolizing enzymes.

Furthermore, we found a significant increase in the cellular uptake of IgG-coated SWCNTs by neutrophils than that of non-functionalized nanotubes, which was consistent with the following facts: (1) as the basic elements of the recognition layer, IgGs were strongly adsorbed onto the walls of the CNTs (Figure 3.2), and could function as a carrier protein for nanotube transportation [9]; (2) the stimulatory effect of IgG-SWCNTs on these inflammatory

cells is higher (Figure 3.5); (3) the degree of oxidative degradation on IgG-SWCNTs in activated neutrophils (Figure 3.6B) is higher; therefore, these results herein demonstrated that the uptake of IgG-absorbed SWCNTs by neutrophils might result in an MPO-driven biodegradation process in activated inflammatory cells. Previous study has described that the binding of the F_c fragment to F_c receptors is a major step in immune defense and it enables the transport of immunoglobulins across cells to their primary sites of action [23]; therefore, the attachment of functional IgG to CNTs may make them recognizable by specific receptors on cells as well as this may change metabolic fate of nanotubes. Similarly, the presence of serum albumin coating markedly enhanced the uptake of SWCNTs by neutrophils or macrophage cells [7, 24-26]. In J774A.1 macrophage-like cells, the majority of BSA-modified SWCNTs were preferentially localized in the perinuclear space and regions along the cell periphery [26]. In future studies, it will be of interest to investigate the subcellular localization of "naked" and IgG-modified SWCNTs inside neutrophils.

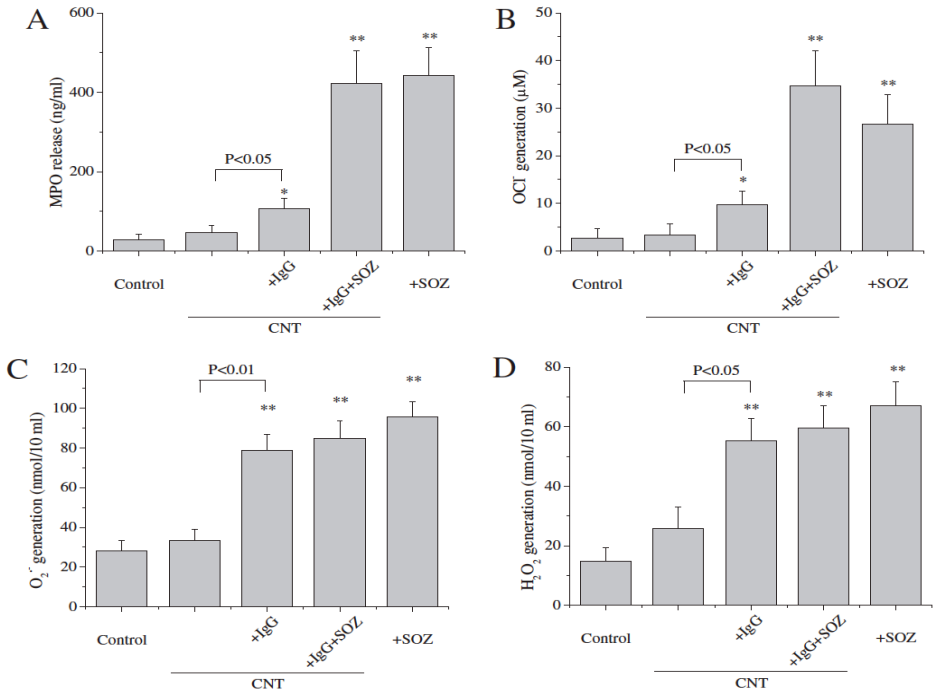

Figure 3.5 IgG-functionalized SWCNTs induced the release of MPO and generation of OCl^- in human neutrophils.
In the absence or presence of serum-opsonized zymosan (SOZ), extracellular release of MPO (A), generation of extracellular OCl^- (B), $O_2^{\cdot-}$ (C) and H_2O_2 (D) were assessed in neutrophils (1×10^6 cells per ml) in response to SWCNT and IgG-SWCNTs (**P<0.01, *P<0.05, groups versus Control).

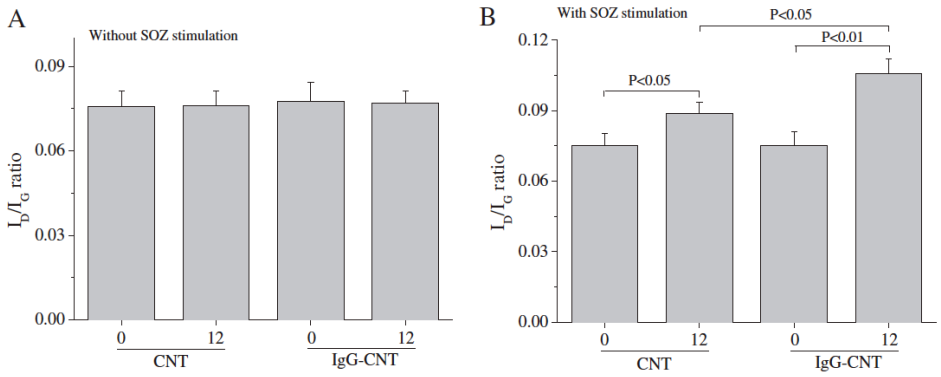

Figure 3.6 Biodegradation of SWCNT and IgG-functionalized SWCNTs in neutrophils in the absence (A) or presence (B) of SOZ stimulation.
D/G intensity ratios obtained from Raman spectroscopy showing biodegradation of nanotubes in human neutrophils after 0 and 12 h (P<0.01, P<0.05, groups versus indicated group, N = 3).

In vivo, animals exposed to CNTs by inhalation, pharyngeal aspiration or intraperitoneal injection developed an acute inflammatory response with increased amounts of circulating neutrophils and activation of neutrophils [6, 9, 12]. Meanwhile, MPO and OCl^- could be present in high concentrations within activated neutrophils and in the extracellular space at inflammatory sites (Figure 3.5), and the binding of IgG would enhance cellular uptake of nanotubes; then, both oxidants (reactive radical intermediates of MPO, OCl^-) with high concentrations and SWCNTs coexisted at inflammatory sites and thereby created the conditions favorable for the degradation of nanotubes. Collectively, the interaction of IgG with SWCNTs herein would influence their delivery, uptake, and toxicity, and hence offer new opportunities to modulate MPO-driven nanotube biodegradation and clearance at the sites of inflammation and in phagosomes. Also, the binding of IgG to SWCNTs may reveal previously unrecognized physiologic effects of human IgG in connection with nanotube biodegradation.

3.4 Conclusions

In this study, we used both theoretical and experimental approaches to investigate the binding of IgG to SWCNTs and its relevance to MPO-mediated SWCNTs degradation. Although the binding of IgG could impair MPO-induced SWCNTs degradation in vitro, the IgG–SWCNTs interactions could affect the cellular inflammatory responses and result in higher biodegradation abilities. The binding of IgG to SWCNTs would enhance cellular uptake of nanotubes, and stimulate MPO release and OCl^- formation in neutrophils, thereby facilitating their degradation process (Figure 3.7). Upon SOZ stimulation (i.e. under natural inflammatory response), both SWCNTs and IgG-SWCNTs were significantly biodegraded in neutrophils, and the biodegradation degree was more for IgG-coated SWCNTs. These findings suggest that the binding of IgG may be an important determinant for SWCNTs biodegradation in human activated

inflammatory cells, and therefore, may provide more insight into the safe design of CNTs for future biomedical applications.

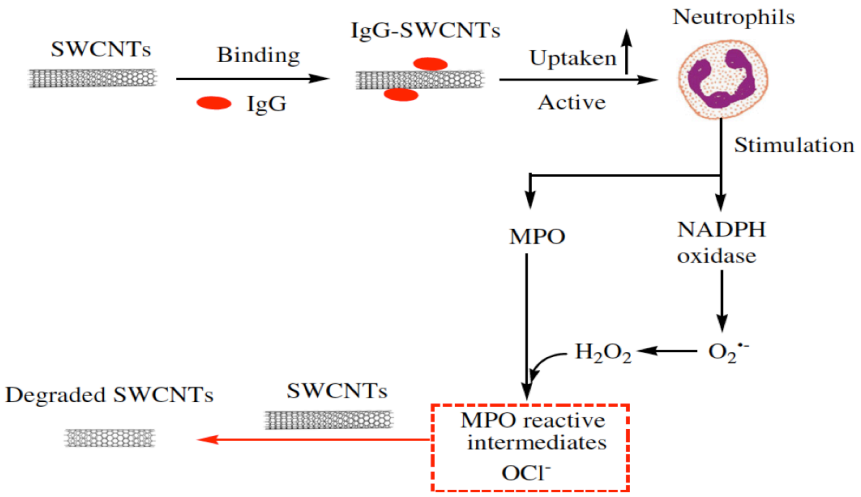

Figure 3.7 Proposed mechanisms for IgG coating-dependent degradation of SWCNTs in neutrophils.

3.5 References

1. Vashist, S.K., D. Zheng, G. Pastorin, K. Al-Rubeaan, J.H.T. Luong, and F.-S. Sheu, *Delivery of Drugs and Biomolecules Using Carbon Nanotubes.* Carbon, 2011. **49**(13): p. 4077-4097.

2. Shvedova, A.A., A. Pietroiusti, B. Fadeel, and V.E. Kagan, *Mechanisms of Carbon Nanotube-Induced Toxicity: Focus on Oxidative Stress.* Toxicology and Applied Pharmacology, 2012. **261**(2): p. 121-133.

3. Saito, N., H. Haniu, Y. Usui, K. Aoki, K. Hara, S. Takanashi, M. Shimizu, N. Narita, M. Okamoto, and S. Kobayashi, *Safe Clinical Use of Carbon Nanotubes as Innovative Biomaterials.* Chemical Reviews, 2014. **114**(11): p. 6040-6079.

4. Johnston, H.J., G.R. Hutchison, F.M. Christensen, S. Peters, S. Hankin, K. Aschberger, and V. Stone, *A Critical Review of the Biological Mechanisms Underlying the in Vivo and in Vitro Toxicity of Carbon Nanotubes: The Contribution of Physico-Chemical Characteristics.* Nanotoxicology, 2010. **4**(2): p. 207-246.

5. Bianco, A., K. Kostarelos, and M. Prato, *Making Carbon Nanotubes Biocompatible and Biodegradable.* Chemical Communications, 2011. **47**(37): p. 10182-10188.

6. Vlasova, I.I., T.V. Vakhrusheva, A.V. Sokolov, V.A. Kostevich, A.A. Gusev, S.A. Gusev, V.I. Melnikova, and A.S. Lobach, *Pegylated Single-Walled Carbon Nanotubes Activate Neutrophils to Increase Production of Hypochlorous Acid, the Oxidant Capable of Degrading Nanotubes.* Toxicology and Applied Pharmacology, 2012. **264**(1): p. 131-142.

7. Lu, N., J. Li, R. Tian, and Y.-Y. Peng, *Binding of Human Serum Albumin to Single-Walled Carbon Nanotubes Activated Neutrophils to Increase Production of Hypochlorous Acid, the Oxidant Capable of Degrading Nanotubes.* Chemical Research in Toxicology, 2014. **27**(6): p. 1070-1077.

8. Kotchey, G.P., Y. Zhao, V.E. Kagan, and A. Star, *Peroxidase-Mediated Biodegradation of Carbon Nanotubes in Vitro and in Vivo.* Advanced Drug Delivery Reviews, 2013. **65**(15): p. 1921-1932.

9. Kagan, V.E., N.V. Konduru, W. Feng, B.L. Allen, J. Conroy, Y. Volkov, I.I. Vlasova, N.A. Belikova, N. Yanamala, and A. Kapralov, *Carbon Nanotubes Degraded by Neutrophil Myeloperoxidase Induce Less Pulmonary Inflammation.* Nature Nanotechnology, 2010. **5**(5): p. 354-359.

10. Van der Veen, B.S., M.P.J. de Winther, and P. Heeringa, *Myeloperoxidase: Molecular Mechanisms of Action and Their Relevance to Human Health and Disease.* Antioxidants & Redox Signaling, 2009. **11**(11): p. 2899-2937.

11. Arnhold, J. and J. Flemmig, *Human Myeloperoxidase in Innate and Acquired Immunity.* Archives of Biochemistry and Biophysics, 2010. **500**(1): p. 92-106.

12. Shvedova, A.A., A.A. Kapralov, W.H. Feng, E.R. Kisin, A.R. Murray, R.R. Mercer, C.M.S. Croix, M.A. Lang, S.C. Watkins, and N.V. Konduru, *Impaired Clearance and Enhanced Pulmonary Inflammatory/Fibrotic Response to Carbon Nanotubes in Myeloperoxidase-Deficient Mice.* PLoS one, 2012. **7**(3): p. e30923.

13. Holt, B.D., K.N. Dahl, and M.F. Islam, *Cells Take up and Recover from Protein-Stabilized Single-Wall Carbon Nanotubes with Two Distinct Rates.* ACS Nano, 2012. **6**(4): p. 3481-3490.

14. Delogu, L.G., E. Venturelli, R. Manetti, G.A. Pinna, C. Carru, R. Madeddu, L. Murgia, F. Sgarrella, H. Dumortier, and A. Bianco, *Ex Vivo Impact of Functionalized Carbon Nanotubes on Human Immune Cells.* Nanomedicine, 2012. **7**(2): p. 231-243.

15. Zuo, G., S.g. Kang, P. Xiu, Y. Zhao, and R. Zhou, *Interactions between Proteins and Carbon‐Based Nanoparticles: Exploring the Origin of Nanotoxicity at the Molecular Level.* Small, 2013. **9**(9‐10): p. 1546-1556.

16. Ge, C., J. Du, L. Zhao, L. Wang, Y. Liu, D. Li, Y. Yang, R. Zhou, Y. Zhao, and Z. Chai, *Binding of Blood Proteins to Carbon Nanotubes Reduces Cytotoxicity.* Proceedings of the National Academy of Sciences, 2011. **108**(41): p. 16968-16973.

17. Holt, B.D., K.N. Dahl, and M.F. Islam, *Quantification of Uptake and Localization of Bovine Serum Albumin‐Stabilized Single‐Wall Carbon Nanotubes in Different Human Cell Types.* Small, 2011. **7**(16): p. 2348-2355.

18. Zhang, S., H. Yang, X. Ji, and Q. Wang, *Binding Analysis of Carbon Nanoparticles to Human Immunoglobulin G: Elucidation of the Cytotoxicity of Cnps and Perturbation of Immunoglobulin Conformations.* Spectrochimica Acta Part A: Molecular and Biomolecular Spectroscopy, 2016. **154**: p. 33-41.

19. Thakur, R., A. Das, V. Sharma, C. Adhikari, K.S. Ghosh, and A. Chakraborty, *Interaction of Different Prototropic Species of an Anticancer Drug Ellipticine with Hsa and Igg Proteins: Multispectroscopic and Molecular Modeling Studies.* Physical Chemistry Chemical Physics, 2015. **17**(26): p. 16937-16946.

20. Cukalevski, R., S.A. Ferreira, C.J. Dunning, T. Berggård, and T. Cedervall, *Igg and Fibrinogen Driven Nanoparticle Aggregation.* Nano Research, 2015. **8**(8): p. 2733-2743.

21. *The Pymol Molecular Graphics System, Version 1.7.4 Schrödinger, Llc*.

22. Li, L., R. Lin, H. He, L. Jiang, and M. Gao, *Interaction of Carboxylated Single-Walled Carbon Nanotubes with Bovine Serum Albumin.* Spectrochimica Acta Part A: Molecular and Biomolecular Spectroscopy, 2013. **105**: p. 45-51.

23. Vermeer, A.W.P., W. Norde, and A. van Amerongen, *The Unfolding/Denaturation of Immunogammaglobulin of Isotype 2b and Its F Ab and F C Fragments.* Biophysical Journal, 2000. **79**(4): p. 2150-2154.

24. Yang, S.T., Y. Liu, Y.W. Wang, and A. Cao, *Biosafety and Bioapplication of Nanomaterials by Designing Protein–Nanoparticle Interactions.* Small, 2013. **9**(9‐10): p. 1635-1653.

25. Monopoli, M.P., D. Walczyk, A. Campbell, G. Elia, I. Lynch, F. Baldelli Bombelli, and K.A. Dawson, *Physical− Chemical Aspects of Protein Corona: Relevance to in Vitro and in Vivo Biological Impacts of Nanoparticles.* Journal of the American Chemical Society, 2011. **133**(8): p. 2525-2534.

26. Boyer, P.D., B.D. Holt, M.F. Islam, and K.N. Dahl, *Decoding Membrane-Versus Receptor-Mediated Delivery of Single-Walled Carbon Nanotubes into Macrophages Using Modifications of Nanotube Surface Coatings and Cell Activity.* Soft Matter, 2013. **9**(3): p. 758-764.

Chapter 4 Carbon nanotube array based biosensor I

A part of this chapter contains our previous published works and submitted manuscript:

1. Chen, J., Lewis, C., Balamurugan, D., Yang, Z., Ai, L., & Cai, D. (2016). Theoretical analysis of a high performance protein imprint on a nanosensor. *Sensing and Bio-Sensing Research*, *7*, 12-19.

2. Yang, Z., Chen, J., Willson, R. C., Cai, D., Ren, Z., Improved detection performance by artificially enhanced interface formation in electropolymerized protein imprints (submitted)

4.1 Introduction

Detection of biomolecules is crucial for many fields, such as healthcare, food safety, environmental monitoring, and drug screening [1-3]. The development of facile and reliable devices that enable direct, high sensitive/selective, and rapid analysis of the target species is necessitated to facilitate the improvement of the detection outcome [4]. The pivot of detection of biosensor resides in the target molecule recognition and consequent signal transduction for electrical amplification. CNTs offer several assets for detection purpose because of their unprecedented structural, mechanical, and electronic properties [5]. First, they constitute scaffolds/platforms, which may be functionalized through conjugation of several entities, thereby potentially enhancing recognition and signal transduction processes [6]. Given their ability to conduct electricity is 100 times greater than copper wires, CNTs are perfect for transduction of electric signals generated upon recognition of a target. Furthermore, the ability of CNTs to cross biological membrane readily makes them applicable in vivo with minimal invasiveness[6].

The study of the CNT-based biosensor was in an explosive growth since 2007 [4]. Tu first reported the development of low site density aligned carbon nanotube array electrode in 2003 [7]; then Lin reported a glucose biosensors based on the carbon nanotube nanoelectrode in 2004, which achieves a limit of detection at 0.08 mM [8]. In 2010, Cai developed an ultra-sensitive biosensor promoted the limit of detection to the level of 10 pg/L with molecule imprint (MI) technology [9].

Biorecognition of proteins with molecular imprints attracts broad interests of applications in biodetection, biopurification, and bioseparation; however, it is still a serious challenge due to the complexity of protein molecules [10]. Conventional approaches established for imprinting small molecules can't be directly applied to protein regarding the choices of monomers selection, temperature, pH, solvent, ionic strength for polymer preparation. The massive amount residues on the protein surface can orchestrate a multitude of interactions with environmental molecules by hydrophobicity, electrical attraction, polarity, hydrogen bond, and van der Waal (VDW) force. Traditionally, functional monomers (fMer) are used to pre-complex with the template based on the complementary interactions between the two molecules; then, the complex is fixed in the scaffold of polymerized cross-linking monomers [11]. The detail is shown in Figure 1.9. The special requirements to design protein imprint reside in at least two folds: first, an fMer screening by computational chemoinfomatics analysis is necessitated, yet the validated guideline and strategy are still unavailable. In line of such effort, GOLD package was used to study the docking of 7 fMers on human serum albumin [12]. It derived the characteristics of the fMer binding, as well as their probable interruption of the protein structures. Second, a complexation between multiple fMers and a protein could help to imprint recognition sites in different aspects of the protein molecule. In a pilot research, the statistical copolymerization of simple binding monomers in defined stoichiometric ratios had shown improved selectivity of protein imprints [13]. But as the number of functional monomer species increase, it becomes difficult to satisfy the reaction

conditions simultaneously in a single polymerization system. To solve the problem, we should first have the binding details of the fMers for a give protein template, which could allow more freedom to choose compatible fMers to produce multiple recognition features in the imprint.

Electropolymerization has been exploited for surface imprinting in biosensors [14]. The reaction normally happens in the aqueous electrolyte solution, which is favorable to retain the physiological conformation of proteins. Various polymers like pyrrole and thiophene derivatives have been used as the imprinting materials [15]. Although mostly no co-polymers are used as the fMer to fabricate imprints in this paradigm, the electropolymerization-based sensors still exhibit remarkable sensitivity and selectivity [16-18]. There may be unrevealed advantages of the process to facilitate the performance of the imprint. In our previous study, protein imprints were fabricated on the tips of a carbon nanotube (CNT) array through electropolymerization of polyphenol (PPn), and were used to conduct ultrasensitive protein sensing [9]. The recognition of target by the imprint was demonstrated with the detections of various proteins including human ferritin E7 biomarker protein (E7) of human papillomavirus (HPV), and bovine calmodulin protein with responsive concentration < 1 ng/L. The sensor differentiated the hFtn under the competition of horse ferritin, apoferritin, and whole protein constituents extracted from bovine muscle tissues in the spiked buffers. Using the same fabrication method, Viswanathan S, et al. (2012), also achieved exceptional detection of ovarian cancer biomarker CA125 in human serum samples [19].

Here, we are looking for the answer of following two questions: 1) How could imprint produced in the simple electropolymerization of phenol provide such high performance? 2) How to improve the performance of protein imprint? The first question will be answered in this chapter, and another one will be answered in the next chapter.

4.2 Methods and materials

4.2.1 Reagents and instrumentation

Phenol, phenol oligomers, ferrocene carboxyl acid (FCA) and bovine serum albumin were obtained from Sigma-Aldrich (St. Louis, MO). Human ferritin protein was obtained from AbD Serotec (Raleigh, NC). Horse ferritin and apoferritin were obtained from MP Biomedicals (Solon, OH). Phosphate buffered saline was obtained from Fisher Scientific (Pittsburgh, PA). Electropolymerization and electrochemical behavior of thin-films were conducted with a Reference600 electrochemical system supplied by Gamry Inc. (Warminster, PA) operating via Framework. Data analysis was conducted with Echem Analyst. TEM images of PPn coated CNTs were obtained with a JEM-2010F TEM (JEOL, Tokyo, Japan) operating at 200 kV.

4.2.2 CNT array preparation

The procedures are the same as previous report [9]. It can be briefly described as following. Array fabrication begins with CNT growth via plasma-enhanced chemical vapor deposition on polystyrene sphere-patterned substrates, followed by embedding in SU8-2002 photoresist and then mechanically polished to expose the tips. First, SU8 was spun on an array at 3000 rpm for 30 s. Following a soft bake for 5 min at 100 °C, SU8 was cross-linked by exposure to UV light for 3 min, and then the sample was incubated at 150 °C overnight. Lastly, the chip was polished with a vibratory polisher (Buehler in Lake Bluff, IL) with 80% power level for 6-9 hrs until the pattern was revealed.

4.2.3 Electrochemistry experiments

A three-electrode electrochemical system included the CNT chip, chlorinated silver wire, and platinum wire as the working, reference and counter electrodes, respectively. PPn film was deposited on the CNT array by cyclic voltammetry in a phenol (1.5 mM) supplemented phosphate

buffered saline (PBS), pH= 7.4. The potential on the working electrode was scanned 5 times between 0 to 0.9 V vs. the reference electrode. In order to entrap ferritin in the PPn coating, the protein (100 mg/ml) was added to the PPn deposition buffer. Following electrophoretic attraction by applying 300 mV DC voltage for 30 s, cyclic voltammetric voltages were used to form the PPn coating as described above for co-deposition of ferritin.

EIS was conducted before and after the PPn deposition to evaluate the impedance properties of the electrode surface and its interface to the buffer solution containing FCA (1 mM) in PBS. The sine wave was 10 mV peak-to-peak in amplitude. It was superimposed on a 300 mV DC voltage. Frequency was scanned from 1 Hz to 1 MHz. The impedance data were fitted to an electrical equivalent circuit using the impedance analysis function in Echem Analyst software. DPV was conducted in the same buffer as that for EIS. Initial and final potentials vs. reference electrode were 0 and 0.5 V respectively. Pulse size was 50 mV and pulse time was 0.05 s; step size was 2 mV, and sample period was 0.1 s.

4.2.4 Protein imprint development

For imprint development, the sensor with ferritin-entrapped PPn coating was rinsed and incubated overnight in deionized water at room temperature. Alternatively, a developing buffer containing acetic acid (5% w/v) and sodium dodecyl sulfate (SDS) (10% w/v) was used for higher protein extract efficiency. After ferritin entrapment and removal, the sample was evaluated by TEM and EIS. To prepare TEM samples, coated CNTs were carefully scraped off with a sharp blade in isopropanol. About 10 ml of CNT suspension was dropped onto TEM copper grids with carbon film. The samples were checked with TEM immediately after isopropanol was vaporized. With this specimen preparation, the cross –section of the coated CNTs could be observed by TEM bright field imaging, as shown in Figure 4.3B.

4.2.5 Molecular dynamics simulation with NAMD

Molecular dynamics simulations were performed for E7 protein in explicit water molecules with oligomers. Three independent simulations were prepared for each type of oligomers – OLS, OLE, and OLT. In each system, initially, oligomers were randomly placed around E7 protein at a distance of 5 Å or greater from the surface of the protein, or from each other. For the simulation of phenolic fMers competition, 12 OET and 12 OLS were added into the system with random position

The structural Hamiltonian and the parameters of the Lennard-Jones potential for the oligomers were taken from the General Amber Force Field (GAFF) and Antechamber from AMBER10 [20, 21]. The point charges for the oligomers were obtained with the AM1-BCC method [22, 23] as implemented in the Antechamber. Water was modeled by TIP3P model [24], and E7 protein was modeled by Amber force field 99SB. The simulations were carried out with NAMD (version 2.9) [25].

During the simulations, the bonds were fixed by using the SHAKE [26] algorithm with the integration time step of 2 *fs*. The damping coefficient for the Langevin dynamics was 5 ps^{-1}. The switching distance on the Lennard-Jones term was set at 10 Å, and the cutoff was 12 Å. The electrostatics interactions were calculated using the particle mesh Ewald (PME) method [27] with a grid size less than $\frac{1}{Å^3}$ spacing. The protein-oligomers-water system was equilibrated as follows: Initially, the water molecules were energetically minimized using the conjugate gradient method, and then gradually heated to 300 K with a temperature step of 3 K. At each temperature step, the solvent molecules were equilibrated for 2 *ps* under a constant NVT conditions using Langevin dynamics. After the final temperature of 300 K was achieved, the solvent molecules were equilibrated further for 5 *ns* under constant NVT. To adjust the density of water, an equilibration of 5 *ns* under constant NPT conditions was performed using the Nośe-Hoover Langevin piston

pressure control. At this stage, the density of protein-oligomer-water system was close to the liquid water density at 300 K, followed by another 10 *ns* under a constant NVT. From the well-equilibrated system, the production runs were performed for a total of 100 *ns*. In the competition simulation, a100 ns NAMD simulation was performed first, then 4 sets of follow-up 20 ns NAMD simulation, which restart from the end of previous 100 ns simulation, was performed.

4.3 The hypothetical mechanism of phenol-based protein imprint

Here, we are looking for the answer of following question: How could imprint produced in the simple electropolymerization of phenol provide such high performance? It may help us to understand the unusual functionality of the electropolymerization products and uncover a new mechanism to efficiently and effectively develop imprints for other protein biomarkers. Our hypothesis is shown in Figure 4.1. The polymerization of PPn randomly derives isomeric structures with ortho-, meta- and para- dialkoxy benzene units in various polymerization degrees [28, 29]. Such a repertoire of oligomers provides an interactive system to facilitate the interaction with the protein template and preferentially self-assemble into a complex to form recognition interfaces. The complex can be entrapped in the PPn scaffold and transfer the unique recognition interface to the imprint after the removal of the template. In this process, the oligomers serve as the fMers used in conventional imprinting. The phenolic compounds actually fall in a category of fMer currently chosen for the protein imprint, which is selected very roughly by their property: either neutral or weak acidic or basic [10]. To explore the hypothetical process, we take a computational approach to analyze the interaction of the compounds on the E7 biomarker, to outline the interactions between the compounds and the template. The results could suggest the experimental approach to improve the imprint.

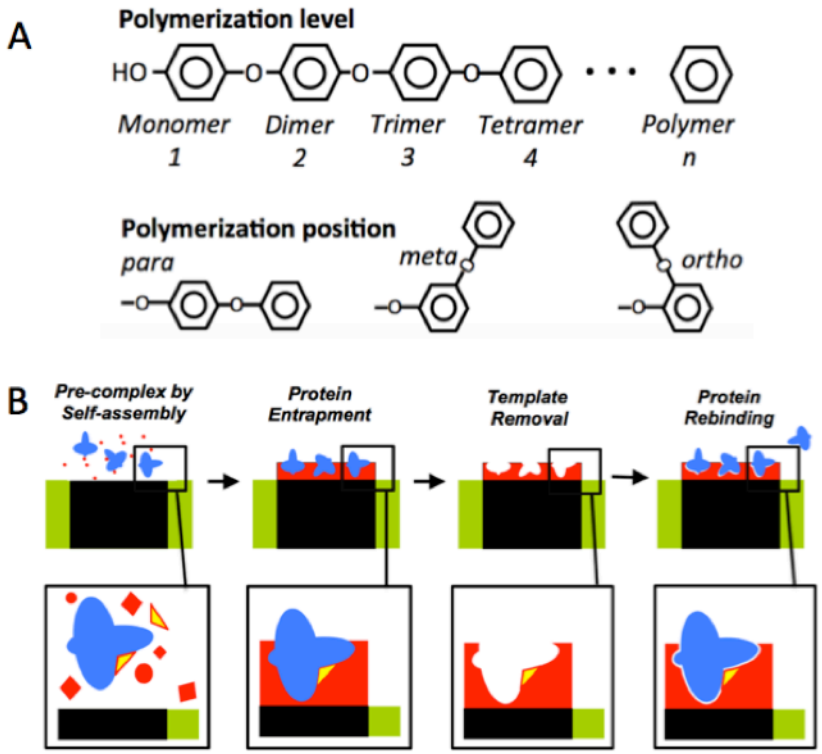

Figure 4.1 Hypothetical imprinting process.
(A) Isomeric PPn produced in the electropolymerization. (B) Isomeric oligomers shown in different shapes are produced on the CNT nanoelectrode (black). Some of the products (yellow) have higher affinity with the template protein (blue) than others (red), and complex with the protein.

4.4 Experimental evidence

Our hypothesis mechanism includes two parts: 1) there should have a relatively high local concentration of various phenolic compounds around the carbon nanotube electrodes; 2) various phenolic compounds should pre-complex with E7 protein, forming a binding interface assembly. Our experimental evidences support the first part, and molecular dynamics simulation provide the supporting for the second part.

To start, we repeated the fabrication of the high-quality imprint as conducted previously with electropolymerized PPn and human ferritin (hFtn) [9]. The protein detection with impedance

and leakage current measurements by electrochemical impedance spectroscopy (EIS) and differential pulse voltammetry (DPV) verified the quality of imprint (Figure 4.2). The results of EIS and DPV were correlated and showed selective and sensitive responses to the hFtn target.

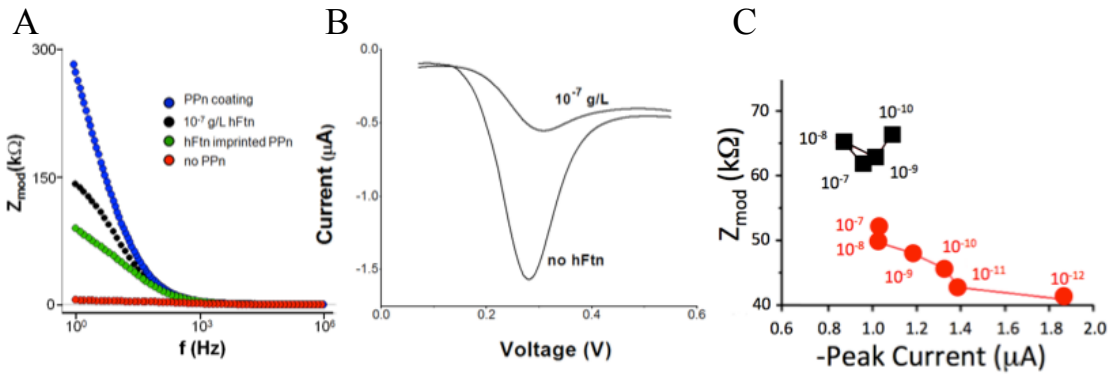

Figure 4.2 Ultrasensitive protein sensing with EIS and DPV by the CNT nanosensor.
The sensor was imprinted with the human ferritin (hFtn). (A) Electrochemical impedance spectroscopy (EIS) with the nanosensor under conditions: as original (no PPn), after PPn coating (PPn coating), after imprint development (hFn imprinted PPn), after imprint rebinding with hFn at 10^{-7} g/L (10^{-7} g/L hFn). (B) Differential pulse voltammetry (DPV) recording of leakage current in the nanosensor: after imprint development (no hFn), and after imprint rebinding with hFn at 10^{-7} g/L (10^{-7} g/L). (C) The signals from EIS and DPV recording are correlated with the hFn rebinding when the concentration increasing from 10^{-12} to 10^{-7} g/L, while no concentration dependent correlation is shown in the non-specific binding of bovine serum albumin.

The strong binding at a protein interface with its receptor is formed by a group of weak interactions at multiple residues [30-32]. Accordingly, if the proposed interface of the E7 protein is formed by a weak interaction, the concentration of the oligomers should be high enough so that the assembly of PPn products on the E7 protein could happen. As shown in Figure 4.3A, the self-limiting Faradic current during the electropolymerization was 146 μC. It was converted into the theoretical volume (denoted as V_{PPn}^{*}) of the PPn deposited on the sensor.

In a transmission electron microscope (TEM) image, the thickness of PPn coating on CNT was 15±3 nm (n=20) (Figure 4.3B). Based on that, the actual volume of PPn deposition

(V_{PPn}) was estimated too. The comparison of the volumes suggested that only 10% of the oxidized phenol molecules were deposited on the CNT tips (Figure 4.3C). The rest could be diffused into the solution at the vicinity of the CNT. Such a high molecular transfer rate was facilitated by the geometry of the nanosensor [33]. Assuming all products were phenolic dimers and applying the Fick's second law of diffusion, the concentration profiles of PPn at the nanoelectrode were estimated (see details in Supporting Information). During the first CV cycle, the concentration could reach as high as 60 mM within a spherical space 20 μm to the CNT (Figure 4.3D).

The calculation process is shown below. The actual volume of PPn (V_{PPn}) can be calculated according to following equation:

$$V_{PPn} = N \times V$$

N is the total amount of nanotubes on the sensor chip. V is the PPn volume on each nanotube. For the example in Figure 4.2, $N = 6.24 \times 10^7$, $V = 2.65 \times 10^{-22}$ m^3. Accordingly, we have $V_{PPn} = 1.7 \times 10^{-14}$ m^3.

Given all phenol participated in the reaction are deposited on the CNT, we can have an alternative way to get the volume of PPn (V_{PPn}^*):

$$V_{PPn}^* = \frac{m \times Q_{PPn}}{F \times \sigma}$$

m is 94 g/mole, Q_{PPn} is the total charge generated during the electropolymerization and equals to 146 μC according to Figure 4.2. *F* is the Faradic constant, 9.65×10^4 C/mole. σ is the density of phenol, 10^6 g/m^3.

Calculated with all numbers above, we have $V_{PPn}^* = 1.42 \times 10^{-13}$ m^3. So in the example shown in Figure 4.2,

$$V_{PPn} = \left(\frac{1}{8.3}\right) \times V_{PPn}^*$$

According to the Faradic current, *I(τ),* produced in the deposition, the concentration profiles of PPn at the nanoelectrode can be derived based on the Fick's second law of diffusion:

$$\phi(r,t) = \int d\,\phi(r,t) = \int_0^t \frac{2}{(4D(t-\tau))^{3/2}} e^{-\frac{r^2}{4D(t-\tau)}} \frac{I(\tau)}{F} d\tau$$

The estimation is based on the assumption that all PPns are dimers.

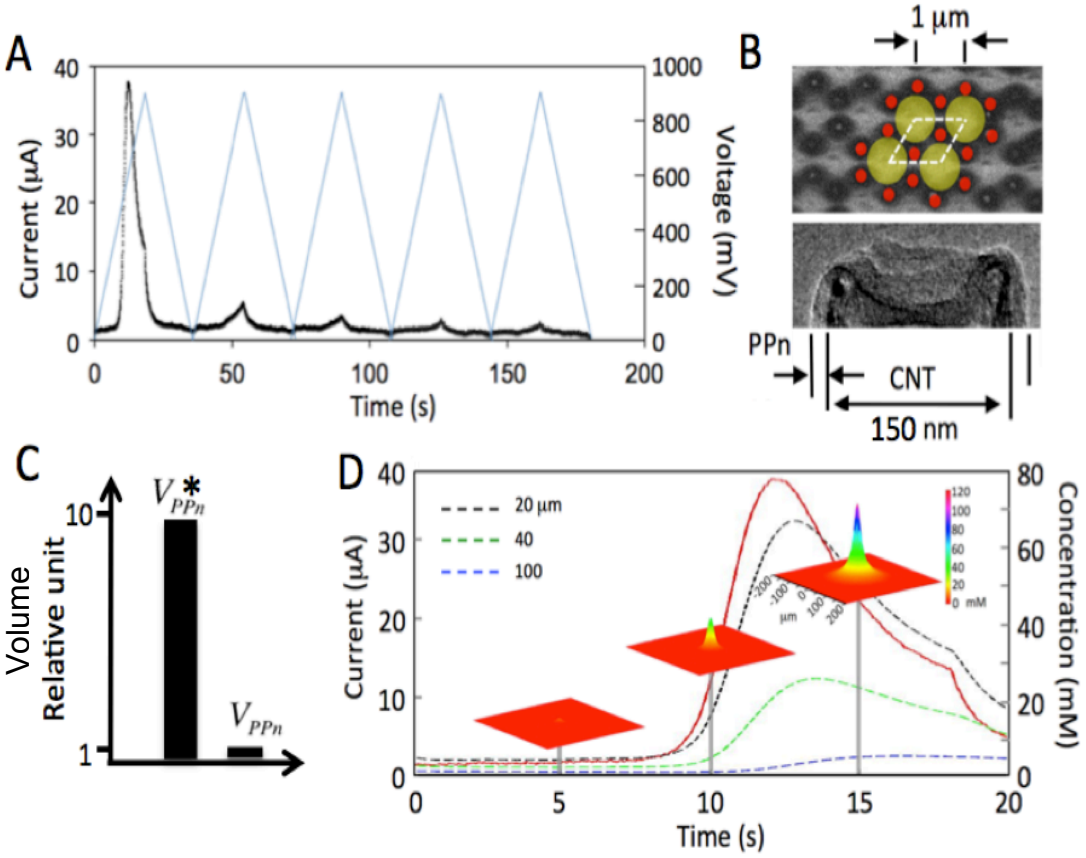

Figure 4.3 PPn concentration profiles in solution during electropolymerization. (A) Self-limiting faradic current in five voltammetric electropolymeirzation cycles. (B) PPn coating on a nanoelectrode array. (Top) Top view with scanning electronic microscopy. The array of nanoelectrodes was in red. (Bottom) Transmission electron microscopy of a single CNT tip coated with electropolymerized PPn. (C) Comparison of PPn deposition volumes estimated in the two approaches. (D) Oligomer concentration profiles calculated according to the diffusion of dimer molecules produced at each nanoelectrode in the first voltammetric cycle. Traces: time courses of the faradic current (red), and dimer concentration correspondingly at 20, 40 and 100 μm from the electrode. The three 3D profiles indicated the dimer concentration profiles in a 400x400 μm^2 area around a nanoelectrode at 5, 10, and 15 s after starting the voltage cycle.

4.5 Molecular dynamics simulation of phenolic compounds self-assembling

The electropolymerization process completes in seconds, and the self-assemble process happens in a much shorter time. The fast reaction makes it very difficult to observe to self-assemble directly in experiment. In this case, molecular dynamics simulation is an alternative to explore the assembly process. As we mentioned above, phenol isomeric dimmers are the leading products in the early stage of electropolymerization, and the concentration could reach as high as 60 mM within a spherical space 20 μm to the CNT. Hence, we use phenolic dimers as the representative of phenolic fMers. The high concentration of phenolic dimers is very likely to assemble around E7 protein.

Human papilloma viruses (HPVs) are a DNA virus family of approximately 200 types that cause human diseases ranging from benign manifestations to debilitating malignancies. As one of only two viral proteins always express in HPV-associated cancers, E7 plays a central role in both the viral life cycle and carcinogenic transformation [34], and is thought to be one of the most promising cervical cancer biomarkers [35].

Here we used the C-domain of HPV45 E7 protein as the target protein (PDB ID: 2EWL), applied all-atomic molecular dynamics simulation to investigate the self-assembling of the phenolic fMers. The simulation is implemented with NAMD (version 2.9), a widely used molecular dynamics simulation software. In the simulation, an E7 protein molecule was placed in the center of the box. Initially, 24 phenolic dimers were randomly placed around E7 protein at a distance of 5 Å or greater from the surface of the protein, or from each other, corresponding to a concentration of 69 mM in the experiment. More than 60,000 explicit water molecules were randomly distributed in the box to make the density of the system get the value 0.989 g/cm^3. The system is equilibrated in a 5 ns NVT and a 5 ns NPT, followed by a 100 ns production run. All

three isomeric dimers, OLS (*4*-Phenoxyphenol), OSE (*2*-Phenoxyphenol) and OET (*3*-Phenoxyphenol) were investigated. Three simulations of OLS, OSE, and OET assembling with E7 protein were implemented first. Considering the competition effect among different dimers, a simulation including both OLS and OET was performed to explore the competition effect.

4.5.1 Simulation of the assembling of mono phenolic dimers

Here we investigated the assembling of OLS, OSE, OET with E7 protein, respectively. The E7-OLS system, like the other two, exhibited stable energy level that converged to -1.43×10^5 kcal/mol during the 100 ns production. The trajectories of all contacting phenolic dimer in every 200 ps were overlaid with the protein in Figure 4.4A. The contact between the molecules was defined in Figure 4.4B. If the distance between two atoms of an oligomer and a protein residue was less than 4 angstroms, a contact was counted. The contact with the protein over time was very dynamic. The averages of contacts per frame (Figure 4.4C, top) largely diverged in each residue. A large contact value and small deviation gave a high score, which meant the contact in high frequency and stability. The highly scored residues were highlighted in red (Figure 4.4C, bottom). In the E7-OLS ensemble, the 18 high-scored and non-charged residues claimed 63 % of the total contact, in which thirteen of them were hydrophobic amino acids. The negatively charged residues, i.e. 20 D, 24 E, 28 E and 33 D did not show high contact frequency although their electrostatic energy was larger than the average. The positively charged residues have very limited amount of contacts. In general, the simulation demonstrates a selective interaction between the phenolic dimers and the protein residues.

To further investigate what the dominant interaction in the contact is, we examined the total energies in details. As shown in Figure 4.5, VDW interaction contributes the central part in the total energy, followed by electrostatic interactions. The peak of the overall interaction is around -190 kCal/mol, to which the VDW interaction contributes the dominant -120 kCal/mol,

and electrostatic interaction provides70 kCal/mol (Figure 4.5B). The interaction detail in each contact is listed in Figure 4.6. The highly scored residues in Figure 4.4C are highlighted in red. The dominant interaction of all highly scored residues is VDW interactions.

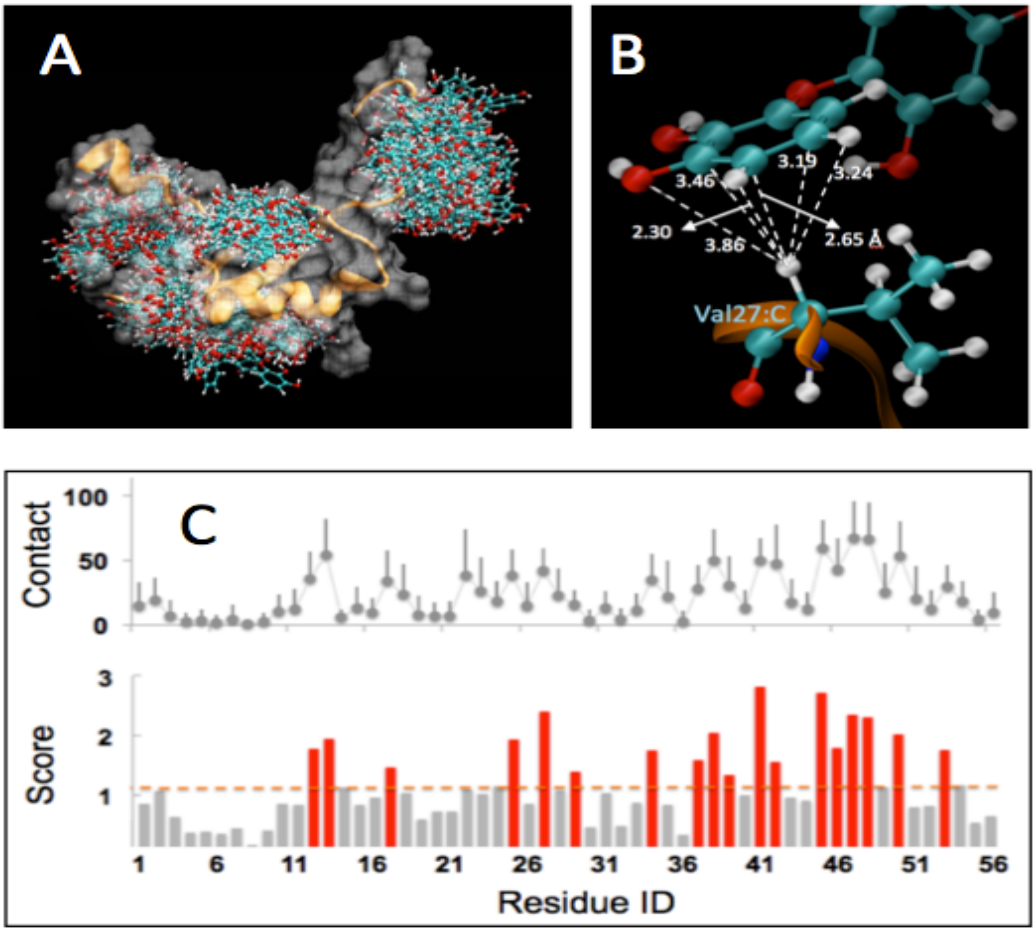

Figure 4.4 Contact between OLS and E7 protein.
(A) Overlay of OLS trajectory on E7 sampled in every 200 ps. OLS is in ball-and-stick. Color representation: Carbon (blue), Oxygen (red). E7 backbone is illustrated in ribbon. Its surface is also outlined in silver. (B) A contact is counted when a dimer atom is less than 4 angstroms (dashed lines) to a residue atom (Val:C). Total number of contact is obtained after all dimer atoms are taken into account. (C) Evaluation of E7 residue contacts. (top) Distribution of contact in residues. The contact number represents contacts per frame. Standard deviation is shown as bar. (bottom) Score of contact in residues. A contact score was defined as: *Contact score=Contact number/Deviation*. Dashed line marked score 1.2, an arbitrary criteria to identify favored contact residues (red). E7 residue ID from 1 to 56 represents amino acid sequence: GSHMAEPQRHKILCVCCKCDGRIELTVESSAEDLRTLQQLFLSTLSFVCP WCATNQ.

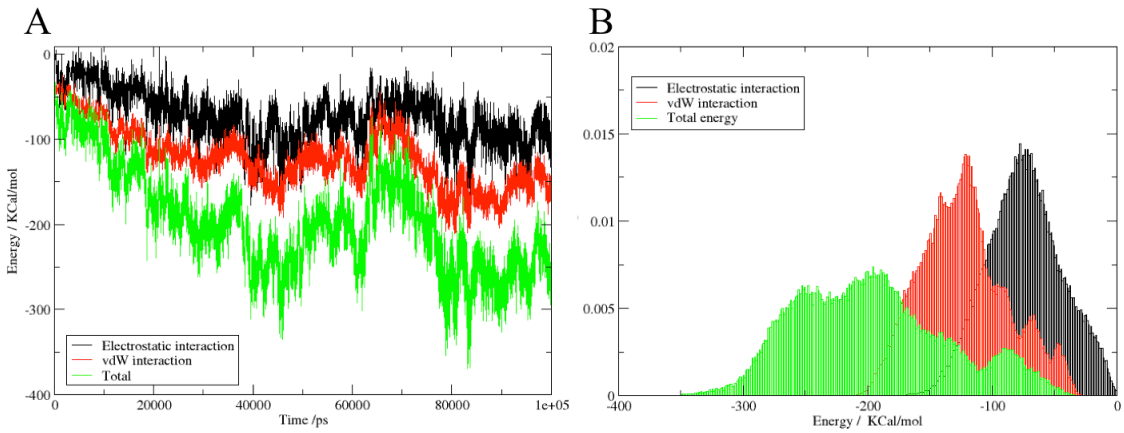

Figure 4.5 Electrostatic interaction (black), VDW interaction (red), and total interaction (green) in the simulation.
Panel A shows the time evolution of all three interactions. Panel B shows the histogram of these three interactions. The peak of electrostatic interaction is around -70 kCal/mol, the peak of VDW interaction is around -120 kCal/mol, and the peak of total interaction is around -190 kCal/mol.

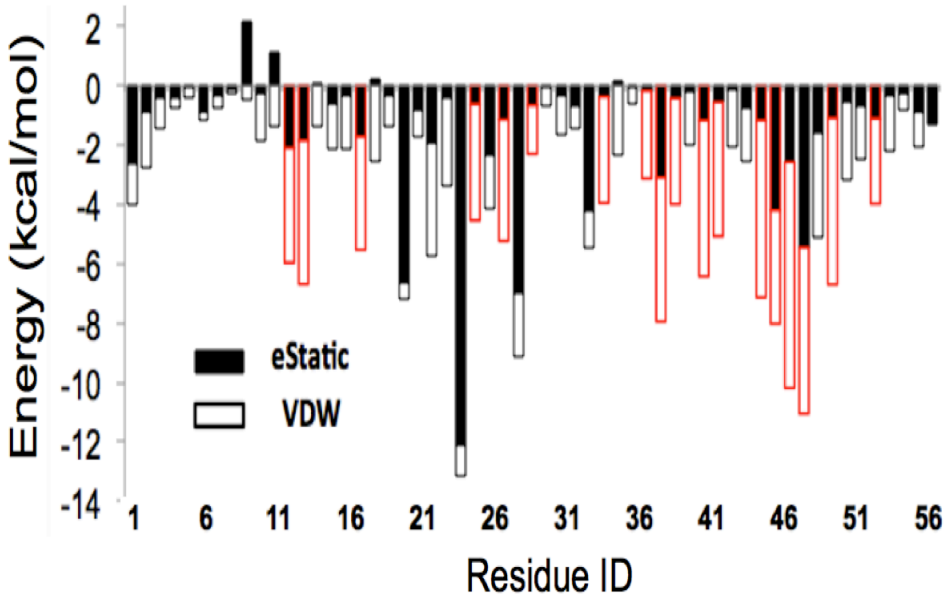

Figure 4.6 Contact energy between OLS and E7 residues.
The electrostatic energy (eStatic) and van der Waals energy (VDW) are overlaid for comparison. The highly scored residues in Figure 4.4C are highlighted in red.

The same conclusion was also drawn with the simulations of the other two dimers, OSE and OET. In fact, their contacts were not identical. The high-score (i.e. score >= 1.2) residues for the three oligomers were collected in Figure 4.7. The hydrophobic residues claimed 72, 65, and 65% of the contact with OLS, OSE, and OET respectively. OLS showed three high-frequency binding regions, i.e. R1: (25, 27, 29), R2: (45, 46, 47, 48) and R3: (37, 42), that was a consensus with OSE in R1 and R3, and OET in R2 and R3 (Figure 4.8). In fact, all those grouped residues were continuous patches of a contact interface.

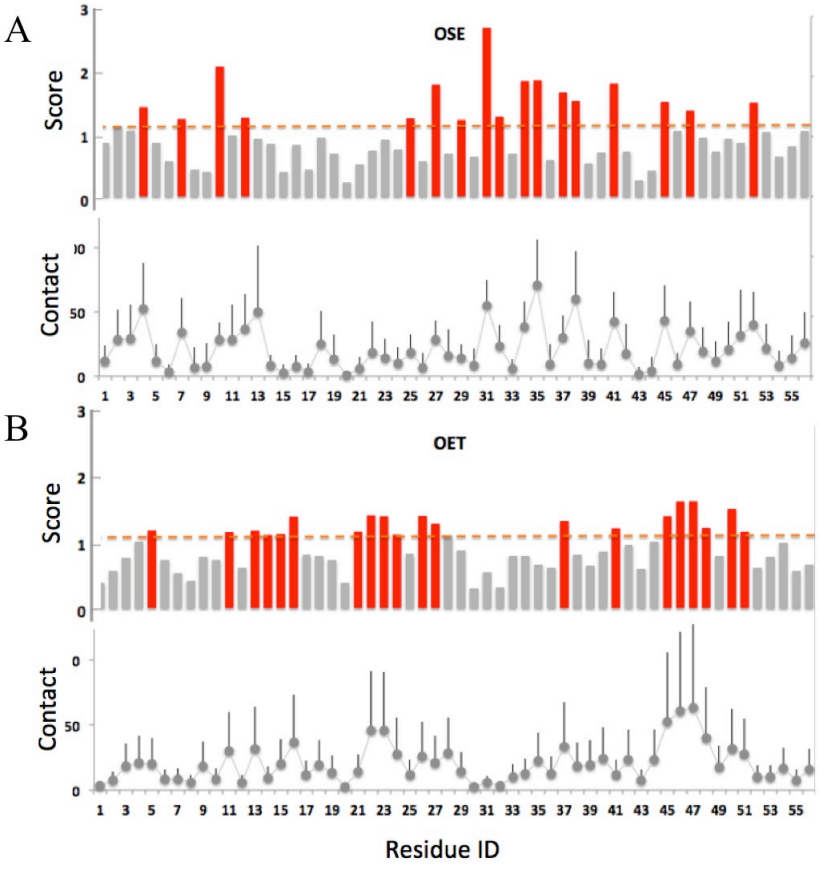

Figure 4.7 Contact of OSE-E7 (a) and OET-E7 (b). Contact value represents contact number per frame. Highly frequent contacts (red) are identified with score 1.2.

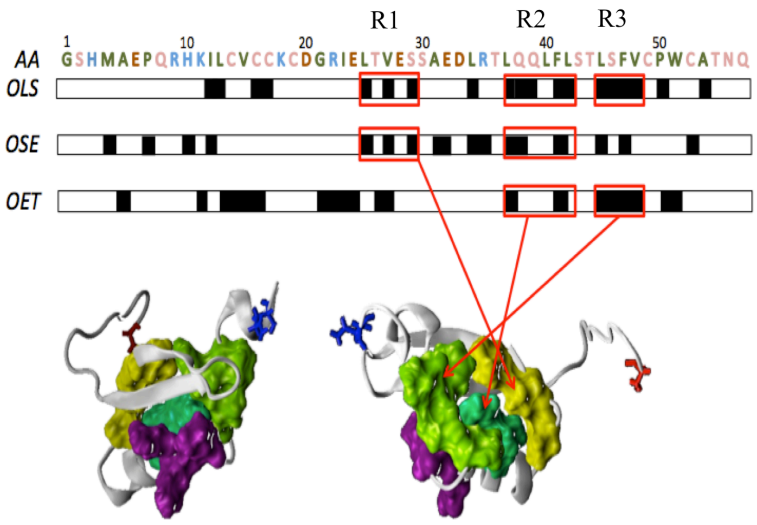

Figure 4.8 Contact interfaces of phenolic dimers with E7 protein.
Based on the contact score, the high contact residues with OLS, OSE, and OET are marked with solid block in the sequence. Three shared contact regions, i.e. R1, R2, and R3, are highlighted in red boxes. Each of them is a continuous surface in the protein. Their residue positions are visualized in the protein (ribbon) structure with different colors: R1, yellow; R2, green; R3, light blue in the front, purple in the back. Opposite sides of E7 protein are shown.

4.5.2 Simulation of the assembling of mixed phenolic dimers

In the electropolymerization process, the self-assembling on the template protein actually takes place with the mixture of phenol oligomers. There will be competition and interaction among the heterogeneous molecules. To characterize the details, we set up a competition system containing 12 OLS and 12 OET. After the same equilibration as before, the simulation was run for 100 ns with NAMD; then four sets of follow-up 20 ns NAMD simulations initiated with the same trajectory from the end of the 100 ns were conducted to evaluate the convergent result of assembly. Root-mean-squared fluctuation (RMSF) for the backbone only was calculated to quantitatively measure the magnitude of the deviation between atomic positions of residues and their native structure from the trajectory. It showed typically large magnitudes at both terminals (Figure 4.9A). The residues between 6 and 50 were rather stable with their RMSF values stayed

below 3.6 angstroms for the first 20 ns (data not shown) and 2.5 angstroms for the follow-up 20 ns. The contact results of the follow-up simulation were highly consistent. Figure 4.9B showed the average amount of dimer per frame in contact with the residues. The deviation was consistently small. The simulation indicated that OLS dominated the phenolic dimers competition for the assembly with E7, since it contributed to 78% of the total contacts. Considering sequence 6 to 56 (residue 1-5 was not taken into account because they are modification residues), the high contact frequency was observed in two major motifs: residue 20 and 30 (mot20-30), and residue 40 and 50 (mot40-50). The regions matched the contact motifs that OLS shared with OSE and OET respectively (Figure 4.8). So the contact pattern from the competition demonstrated more similarity to that of the OLS alone, which indicated the dominant role of OLS from another perspective. The pattern was the result of multiple interactions between the OLS and OET, and between the phenolic dimers and the template separately. The structural similarity in the phenolic dimers largely minimized the energy barrier for OLS to interfere with OET's binding activity and take over the occupancy of the binding site. As shown in Figure 4.9C, OET occupied the four residues of R2:(45,46,47,48) at the beginning. OLS competed for the binding and overwhelmed OET after 5 ns. It dominated the contact in term of overall contact time and instant contact number.

If we investigate the binding from the view of single dimer molecule, we can find an interesting competition story. As shown in Figure 4.10, OET63 (phenolic dimer OET with molecular ID 63) and OLS60 were focused regarding their contact with residues in the 100 ns. OET63 got in touch with E7 at several motifs earlier than OLS60. At 3.5 ns, OET63 completely lost contact with the E7, but OLS60 stayed on. At 41 ns, OET63 came back and occupied R1; however, it lost the contact at 50 ns. In general, OET63 did not retain its contact at any part of the E7 longer than 10 ns, while OLS60 secured the contacts R1 and R3 for 30 ns and R2 for almost 100 ns. Particularly, we can observe the competition between OLS and OET on E7 protein.

Although OET63 contacted with R1, R2, and R3 earlier than OLS60, it was replaced at those places completely by OLS60 at 2.5 ns.

In Figure 4.11, we computed the binding probability of OET63 and OLS60 in the equilibrium state. After the intense competition, both OET63 and OLS60 have their favorite binding sites; hence, the final binding pattern for OET63 and OLS60 are totally different. The preferred binding sites are residue 16, 18-23, 49-52 for OLS60, and residue 17, 25-27, 37, 41, 45-48 for OET63. This is a little different with the binding pattern in the simulation without competition.

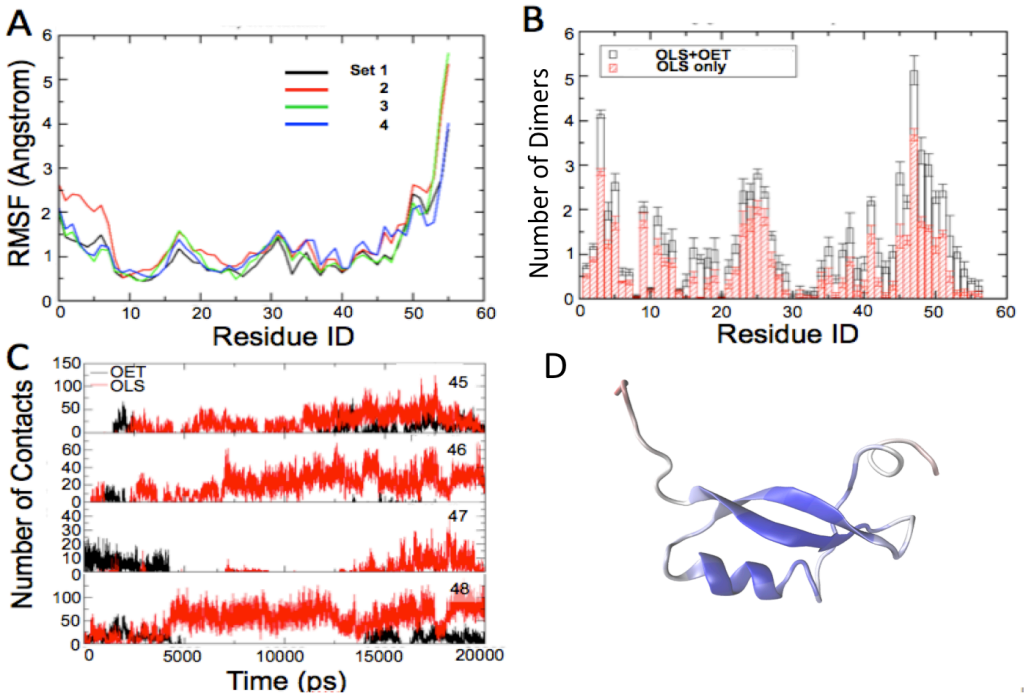

Figure 4.9 Competition in phenolic dimers for bindings with E7 protein. (A) RMSF values of the E7 residues in the four sets of follow-up competition between OLS and OET. (B) Summary of the average number of phenolic dimers in contact with each E7 residue from the four sets of follow-up competition for 20 ns. The total phenolic dimers, i.e. OLS+OET, and the OLS only are overlaid for comparison. Error bar stands for standard deviation. (C) Time course of phenolic dimers contacts in the competition for R2: (45,46,47,48). The data is from one of the 20 ns follow-up simulations. The number in each panel is the ID of residues. (D) Schematics of RMSF in E7 protein, the color from blue to red represent the RMSF value from low to high.

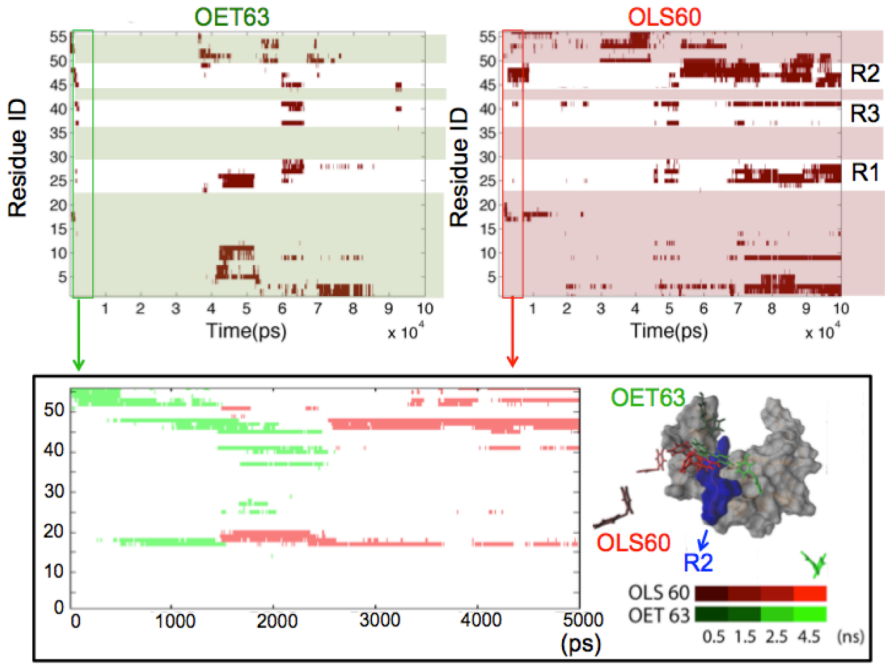

Figure 4.10 Trajectory of phenolic dimers as time course of residues in contact. OLS60 and OET63 closely interacted in the simulation for 100 ns. R1, R2 and R3 indicate the contact region extracted based on contact scores and outlined in Figure 3. A highly dynamic scenario at the first 5 ns is magnified. Inset: the relative position of the pfMers and the E7 protein at 0.5, 1.5, 2.5 and 4.5 ns.

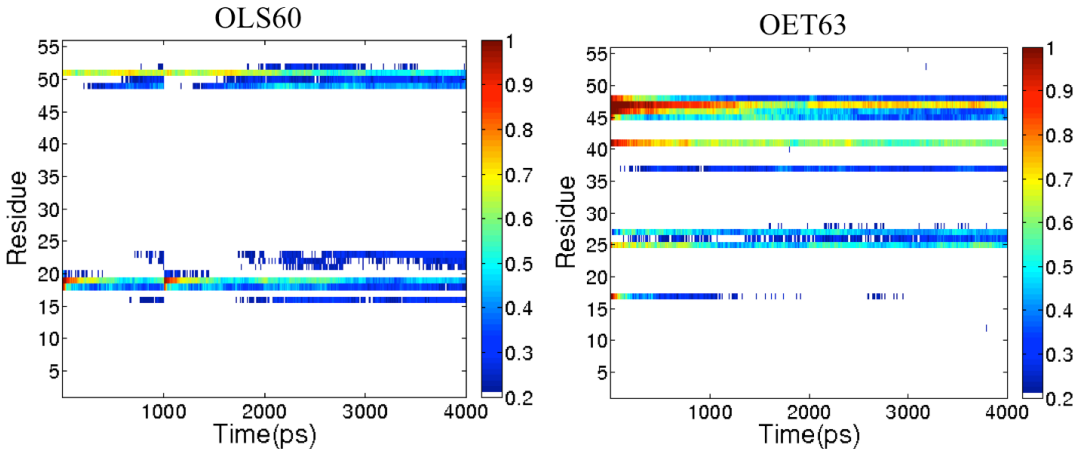

Figure 4.11 Binding probability of OLS60 with E7 (left panel) and binding probability of OET63 with E7 (right panel). The color represents the binding probability from 0.2 to 1.

4.6 Conclusions

Although the electropolymerization is a convenient method to develop MI on sensor electrodes, the formation of MI has not been studied in details yet [36]. In this chapter, we followed the experimental results of the ultrasensitive biosensing to investigate the mechanisms of high-performance protein imprinting.

First, we put forward our hypothesis based on the fact that the polymerization of PPn randomly derives isomeric structures with ortho-, meta- and para- dialkoxy benzene units in various polymerization degrees. Such a repertoire of oligomers provides an interactive system to facilitate the interaction with the protein template and preferentially self-assemble into a complex to form recognition interfaces. The complex can be entrapped in the PPn scaffold and transfer the unique recognition interface to the imprint after the removal of the template. In this process, the oligomers serve as the fMers used in conventional imprinting.

Then we demonstrated that a high concentration (60 mM) of phenolic oligomer could be produced within a spherical space 20 μm to the CNT in the electropolymerization process. The concentration of 60 mM is high enough for the phenolic oligomer to assemble around E7 protein.

Finally, we applied all-atom molecular dynamic simulation to prove that phenolic dimer can assemble around E7 in a short time (< 100 ns).

This study was focused on the self-assembly process that involved in the electropolymerization conducted with the nanosensor. All-atomic molecular dynamic simulations, with and without competition, demonstrated that the oligomers products from the reaction at the experimental concentration were able to complex with the E7 biomarker protein alike the fMers to complex with template molecules in conventional MI fabrications. In the contact analysis of the three dimers, i.e. OLS, OSE, and OET, these phenolic dimers shared some of their assembly characteristics but also exhibited their own properties. The competition simulation with OLS and

OET revealed that, even though the assembly was governed by OLS, OET has its own binding sites. The complex was selectively shaped with the characteristics of OLS and OET. It indicated that both OLS and OSE are important to determine the biorecognition of the E7 imprint. Regarding the possible binding sites for the E7 recognition, it was surprising that the high-frequency contact regions identified with the contact score agreed well with the result of competition simulation.

So self-assembly is a novel perspective to understand the formation of the recognition. The conclusion of this research suggests a new approach to design and synthesize the protein imprint: first, the oligomer products can be considered as fMers to contribute unique recognition properties like binding site and affinity to the imprint; second, the protein imprint can be developed to feature recognition motifs and unprecedented affinity using the designed pre-complex with the specific fMer. Lastly, the self-assembly can be facilitated by nanoelectrodes that provide advantageous concentration profiles of the fMers. With such novel concept, strategy, and tools, high-performance protein imprints can be designed and fabricated in the ultrasensitive nanosensors to satisfy the requirements of biorecognition in biodetections.

4.7 References

1. Zhang, X., Q. Guo, and D. Cui, *Recent Advances in Nanotechnology Applied to Biosensors.* Sensors, 2009. **9**(2): p. 1033-1053.

2. Justino, C.I.L., T.A. Rocha-Santos, and A.C. Duarte, *Review of Analytical Figures of Merit of Sensors and Biosensors in Clinical Applications.* TrAC Trends in Analytical Chemistry, 2010. **29**(10): p. 1172-1183.

3. Guo, S. and S. Dong, *Biomolecule-Nanoparticle Hybrids for Electrochemical Biosensors.* TrAC Trends in Analytical Chemistry, 2009. **28**(1): p. 96-109.

4. Yang, N., X. Chen, T. Ren, P. Zhang, and D. Yang, *Carbon Nanotube Based Biosensors.* Sensors and Actuators B: Chemical, 2015. **207**: p. 690-715.

5. Münzer, A.M., M. Heimgreiter, K. Melzer, A. Weise, B. Fabel, A. Abdellah, P. Lugli, and G. Scarpa, *Back-Gated Spray-Deposited Carbon Nanotube Thin Film Transistors Operated in Electrolytic Solutions: An Assessment Towards Future Biosensing Applications.* Journal of Materials Chemistry B, 2013. **1**(31): p. 3797-3802.

6. Tîlmaciu, C.-M. and M.C. Morris, *Carbon Nanotube Biosensors.* Frontiers in Chemistry, 2015. **3**.

7. Tu, Y., Y. Lin, and Z.F. Ren, *Nanoelectrode Arrays Based on Low Site Density Aligned Carbon Nanotubes.* Nano Letters, 2003. **3**(1): p. 107-109.

8. Lin, Y., F. Lu, Y. Tu, and Z. Ren, *Glucose Biosensors Based on Carbon Nanotube Nanoelectrode Ensembles.* Nano letters, 2004. **4**(2): p. 191-195.

9. Cai, D., L. Ren, H. Zhao, C. Xu, L. Zhang, Y. Yu, H. Wang, Y. Lan, M.F. Roberts, and J.H. Chuang, *A Molecular-Imprint Nanosensor for Ultrasensitive Detection of Proteins.* Nature Nanotechnology, 2010. **5**(8): p. 597-601.

10. Whitcombe, M.J., I. Chianella, L. Larcombe, S.A. Piletsky, J. Noble, R. Porter, and A. Horgan, *The Rational Development of Molecularly Imprinted Polymer-Based Sensors for Protein Detection.* Chemical Society Reviews, 2011. **40**(3): p. 1547-1571.

11. Turner, N.W., C.W. Jeans, K.R. Brain, C.J. Allender, V. Hlady, and D.W. Britt, *From 3d to 2d: A Review of the Molecular Imprinting of Proteins.* Biotechnology Progress, 2006. **22**(6): p. 1474-1489.

12. Kryscio, D.R., Y. Shi, P. Ren, and N.A. Peppas, *Molecular Docking Simulations for Macromolecularly Imprinted Polymers.* Industrial & Engineering Chemistry Research, 2011. **50**(24): p. 13877-13884.

13. Koch, S.J., C. Renner, X. Xie, and T. Schrader, *Tuning Linear Copolymers into Protein‐Specific Hosts.* Angewandte Chemie International Edition, 2006. **45**(38): p. 6352-6355.

14. Dechtrirat, D., K.J. Jetzschmann, W.F.M. Stöcklein, F.W. Scheller, and N. Gajovic‐Eichelmann, *Protein Rebinding to a Surface‐Confined Imprint.* Advanced Functional Materials, 2012. **22**(24): p. 5231-5237.

15. Whitcombe, M.J. and D. Lakshmi, *Imprinted Polymers.* Electropolymerization: Concepts, Materials and Applications, 2010: p. 133-151. Wiley-VCH.

16. Malitesta, C., E. Mazzotta, R.A. Picca, A. Poma, I. Chianella, and S.A. Piletsky, *Mip Sensors–the Electrochemical Approach.* Analytical and Bioanalytical Chemistry, 2012. **402**(5): p. 1827-1846.

17. Menaker, A., V. Syritski, J. Reut, A. Öpik, V. Horváth, and R.E. Gyurcsányi, *Electrosynthesized Surface‐Imprinted Conducting Polymer Microrods for Selective Protein Recognition.* Advanced Materials, 2009. **21**(22): p. 2271-2275.

18. Sharma, P.S., A. Pietrzyk-Le, F. D'souza, and W. Kutner, *Electrochemically Synthesized Polymers in Molecular Imprinting for Chemical Sensing.* Analytical and Bioanalytical Chemistry, 2012. **402**(10): p. 3177-3204.

19. Viswanathan, S., C. Rani, S. Ribeiro, and C. Delerue-Matos, *Molecular Imprinted Nanoelectrodes for Ultra Sensitive Detection of Ovarian Cancer Marker.* Biosensors and Bioelectronics, 2012. **33**(1): p. 179-183.

20. Case, D.A., T.A. Darden, Cheatham, C.L. Simmerling, J. Wang, R.E. Duke, R. Luo, M. Crowley, R.C. Walker, W. Zhang, K.M. Merz, B. Wang, S. Hayik, A. Roitberg, G. Seabra, I. Kolossváry, K.F. Wong, F. Paesani, J. Vanicek, X. Wu, S.R. Brozell, T. Steinbrecher, H. Gohlke, L. Yang, C. Tan, J. Mongan, V. Hornak, G. Cui, D.H. Mathews, M.G. Seetin, C. Sagui, V. Babin, and P.A. Kollman, *Amber 10*. 2008, University of California, San Francisco.

21. Wang, J., R.M. Wolf, J.W. Caldwell, P.A. Kollman, and D.A. Case, *Development and Testing of a General Amber Force Field.* Journal of Computational Chemistry, 2004. **25**(9): p. 1157-1174.

22. Jakalian, A., B.L. Bush, D.B. Jack, and C.I. Bayly, *Fast, Efficient Generation of High‐Quality Atomic Charges. Am1‐Bcc Model: I. Method.* Journal of Computational Chemistry, 2000. **21**(2): p. 132-146.

23. Jakalian, A., D.B. Jack, and C.I. Bayly, *Fast, Efficient Generation of High‐Quality Atomic Charges. Am1‐Bcc Model: Ii. Parameterization and Validation.* Journal of Computational Chemistry, 2002. **23**(16): p. 1623-1641.

24. Jorgensen, W.L., J. Chandrasekhar, J.D. Madura, R.W. Impey, and M.L. Klein, *Comparison of Simple Potential Functions for Simulating Liquid Water.* The Journal of Chemical Physics, 1983. **79**(2): p. 926-935.

25. Phillips, J.C., R. Braun, W. Wang, J. Gumbart, E. Tajkhorshid, E. Villa, C. Chipot, R.D. Skeel, L. Kale, and K. Schulten, *Scalable Molecular Dynamics with Namd.* Journal of Computational Chemistry, 2005. **26**(16): p. 1781-1802.

26. Ryckaert, J.-P., G. Ciccotti, and H.J.C. Berendsen, *Numerical Integration of the Cartesian Equations of Motion of a System with Constraints: Molecular Dynamics of N-Alkanes.* Journal of Computational Physics, 1977. **23**(3): p. 327-341.

27. Darden, T., D. York, and L. Pedersen, *Particle Mesh Ewald: An N·Log (N) Method for Ewald Sums in Large Systems.* Journal of Chemical Physics, 1993. **98**: p. 10089.

28. Flory, P.J., *Principles of Polymer Chemistry Cornell University Press, Ithaca, 1953.* There is no corresponding record for this reference.

29. Ežerskis, Z., G. Stalnionis, and Z. Jusys, *Electropolymerization of Chlorinated Phenols on a Pt Electrode in Alkaline Solution. Part Ii: An Electrochemical Quartz Crystal Microbalance Study.* Journal of Applied Electrochemistry, 2002. **32**(1): p. 49-55.

30. Goodsell, D.S., *Bionanotechnology: Lessons from Nature*. 2004: John Wiley & Sons.

31. Abyzov, A., A. Uzun, P.R. Strauss, and V.A. Ilyin, *An Ap Endonuclease 1–DNA Polymerase B Complex: Theoretical Prediction of Interacting Surfaces.* PLoS Computational Biology, 2008. **4**(4): p. e1000066.

32. Larsen, T.A., A.J. Olson, and D.S. Goodsell, *Morphology of Protein–Protein Interfaces.* Structure, 1998. **6**(4): p. 421-427.

33. Bard, A.J. and L.R. Faulkner, *Fundamentals and Applications.* Electrochemical Methods, 2001. **2**.

34. McLaughlin-Drubin, M.E. and K. Münger, *The Human Papillomavirus E7 Oncoprotein.* Virology, 2009. **384**(2): p. 335-344.

35. Fontecha, N., M. Basaras, S. Hernáez, D. Andía, and R. Cisterna, *Assessment of Human Papillomavirus E6/E7 Oncogene Expression as Cervical Disease Biomarker.* BMC Cancer, 2016. **16**(1): p. 852.

36. Whitcombe, M.J., N. Kirsch, and I.A. Nicholls, *Molecular Imprinting Science and Technology: A Survey of the Literature for the Years 2004–2011.* Journal of Molecular Recognition, 2014. **27**(6): p. 297-401.

Chapter 5 Carbon nanotube array based biosensor II

A part of this chapter contains our previous published works and unpublished manuscript:

1. Chen, J., Lewis, C., Balamurugan, D., Yang, Z., Ai, L., & Cai, D. (2016). Theoretical analysis of a high performance protein imprint on a nanosensor. *Sensing and Bio-Sensing Research*, *7*, 12-19.

2. Yang, Z., Chen, J., Willson, R. C., Cai, D., Ren, Z., Improved detection performance by artificially enhanced interface formation in electropolymerized protein imprints (submitted)

5.1 Introduction

In the last chapter, we find that it is the assembly-binding pattern enables the recognition of E7 protein. Naturally, the following question emerges: can we improve the recognition performance by modifying the binding pattern? To answer this question, we must figure out the binding pattern of different compounds; however, molecular dynamics simulation is too expensive and time-consuming. It's inappropriate for the screening of hundreds of candidate compounds. Computational docking is an alternative for molecular dynamics simulation, which is cheap and time-efficient with the penalty of accuracy. Docking is a computational method used to predict the preferred orientation and binding site of one molecule to another. Computed binding affinity indicates the strength of association. Among dozens of docking software, AutoDock is one of the most cited docking software in the research community. To make up the accuracy defect of docking, we apply molecular dynamics simulation to the picked compounds again.

5.2 Methods and materials

The dataset of 49 commonly used functional monomers was taken from the literature [1], and the dataset of 19 protein functional monomers was taken from the literature [2]. Those SDF format files were transformed into PDB format by Open Babel [3]. AutoDockTools1.5.6rc3 [4] was used to create the PDBQT format files by merging non-polar hydrogens, assigning the polar hydrogens, adding Gasteiger charges, and selecting the rotatable bonds.

AutoDock is one of the most cited docking software in the research community. It's free to access on line. AutoDock Vina is a new program for molecular docking and virtual screening based on AutoDock [5]. The accuracy of binding mode prediction is significantly improved, and the computing speed is two orders of magnitude faster compared with AutoDock 4. Further speed-up can be achieved by using multithreading. We used both AutoDock 4.2.5.1 and AutoDock Vina for docking in this paper.

For both AutoDock 4 and AutoDock Vina, the grid box was centered at the center of the E7 protein. The size of grid box was 42 Å × 36 Å × 28 Å, with a spacing 1 Å, covering the whole protein molecule. The value of ga_run was set to be 100 for AutoDock 4. The number of CPU was set to be 8 for AutoDock Vina. The other parameters were using the default values.

5.3 Docking accuracy testing with AutoDock

Before our further investigation, the accuracy of docking should be tested. To test the accuracy of docking, we compared the binding pattern of phenolic dimers OLS with the binding pattern we got from the molecular dynamic simulation. AutoDock 4 (version 4.2.5.1) was applied for the computational docking. The analysis by AutoDock 4 gave us a quantitative evaluation of the interaction determined by the calculation of van der Waals force, hydrogen bonding,

electrostatics, and desolvation. The grid box was centered at the center of the E7 protein (PDB ID: 2EWL). The size of grid box was 42 Å × 36 Å × 28 Å, with a spacing 1 Å, covering the whole protein molecule. The value of ga_run was set to be 100 for AutoDock 4.

Each run of docking produces a predicted binding mode and corresponding binding contacts. All binding contacts form 100 independent docking was collected to plot a histogram of binding contact as shown in Figure 5.1A. Residue LEU25, VAL27, GLU28, PHE41, and PHE47 form the binding interface, and most of them are nonpolar or aromatic groups. The docking result is very similar to the binding pattern we got from molecular dynamics simulation (Figure 5.1B). This test demonstrates that docking has a high accuracy in the prediction of the binding pattern as molecular dynamics simulation.

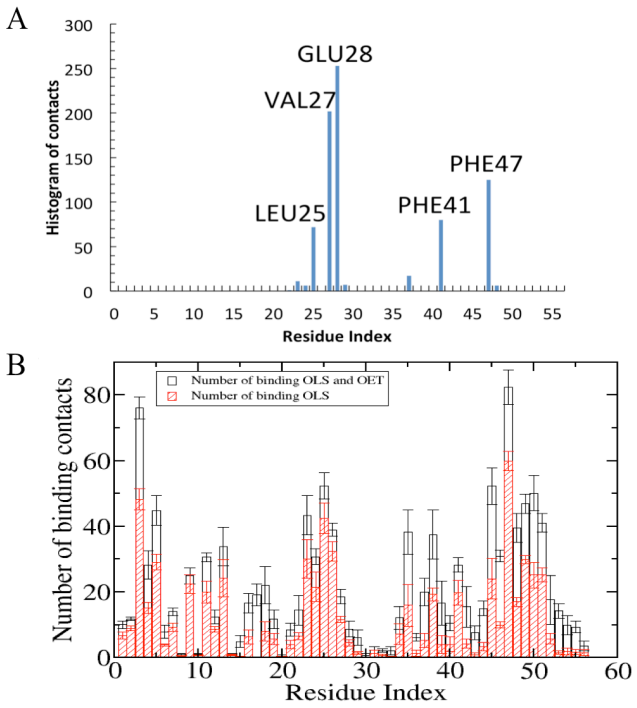

Figure 5.1 Comparison of the binding pattern of phenolic dimer OLS form docking (A) and molecular dynamics simulation (B).

5.2 Docking of phenolic oligomers

Having proved the accuracy of binding pattern prediction, we continued to investigate the binding pattern of 3 phenolic dimers and 9 phenolic trimers. The schematics of the binding pattern is shown in Figure 5.2A. The binding energy ΔG of the dimers showed a distribution from -2.4 to -4.1 kCal/mol (Figure 5.2B). In contrast, trimers had higher binding energy with the level between -2.1 to -5.2 kCal/mol. The mean values of ΔG of the dimer and trimer were -3.1±0.021 and -3.8±0.014 kCal/mol.

The result suggested that the phenolic oligomers had distinctive binding properties at least in the binding energy ΔG, which agreed to our hypothesis described in Figure 4.1. The cluster of docking also outlined the specific areas of the E7 protein that were subject to interaction in a great amount of contact with the compounds. It suggested the similarly as Figure 4.1. Since docking held advantages in screening efficiency, it became possible to examine a larger compound library to understand the characteristics of the assembly and optimize the E7 recognition of imprint in later sections.

Meanwhile, the difference in binding energy of phenolic dimer and phenolic trimer may be explained by the molecule size. Given the dominant interaction action between the phenolic oligomer and E7 protein is van der Waals interaction, larger molecule size indicates larger contact surface area, which results in larger binding energy. We get an opportunity to verify this suspicion in the screening of more compounds.

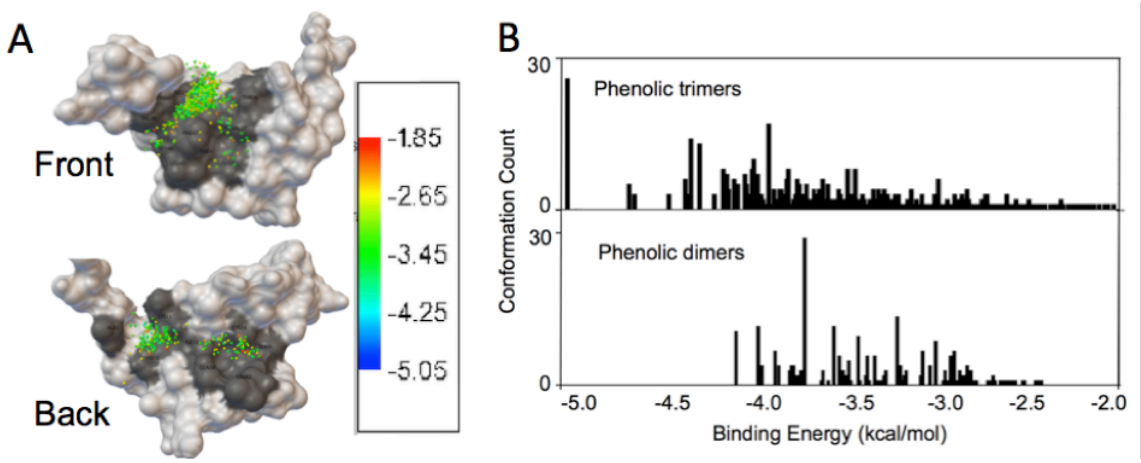

Figure 5.2 Docking of phenolic compounds on the E7 protein with AutoDock 4. (A) The clustering of all docking conformations on 2EWL. The dark areas outline the contact areas with the compounds. (B) Histogram of the binding energy from the docking of 9 trimers and 3 dimers.

5.4 Comparison of compounds from different libraries with AutoDock Vina

We extended the docking analysis for more phenolic oligomers up to pentamer. Also, we included the libraries for traditional fMer and protein imprinting (named pfMer) that were found in publications [1, 2]. Note that AutoDock Vina had improved the searching capability comparing to AutoDock 4 [5]. AutoDock Vina was used to go through the calculation of the libraries with totally 189 entries. The best pose that showed largest ΔG in the 100 runs of each compound was used for sorting and getting the compounds index in the plot (Figure 5.3A). The phenolic compounds from monomer to pentamer did show increase of ΔG with the number of aromatic groups. But this dependency decreased at high-level oligomers like tetramer and pentamer. About 30% percent of pentamers had even lower ΔG than the highest 5 trimers. The phenolic dimers and trimers were put for further comparison and characterization with the fMers and pfMers. Apparently, the dimers and timers had larger values of binding energy than most of the fMers and

pfMers. The contact maps of the top 10 scored phenolic dimer and trimers, fMers and pfMers are showed in Figure 5.3B. At the first look, the binding patterns seem to be similar; however, if we check the binding maps carefully, we would find three distinguish properties of phenolic oligomer with fMers and pfMers. 1) All top 10 scored phenolic oligomers have the similar binding pattern, while different fMers and pfMers's binding pattern are quite different. 2) The number of binding contact of phenolic oligomer (~300) is much more than fMers (~200) and pfMers (~100). 3) pfMers has more binding sites than phenolic oligomer and fMers. This makes it possible to get additional binding energy and binding sites by adding specific pfMer in the polymerization process.

It was helpful to clarify such preferential interaction with the E7 protein. The compounds in fMer library varied largely in the molecular weight, aromatic carbons, rotatable bond, and donor and acceptor of H-bond. Their values of ΔG were plotted to demonstrate the dependency of the interactions coherent to the properties of the E7. As shown Figure 5.4, the binding energy had a more obvious correlation to the values of molecular weight and aromatic atom than that of the rotatable bond, H-bond donor and acceptor, and polar area. So the van der Waal force and hydrophobic interaction seemed to play the major role in the interfaces. The interaction agreed with the structural characterization showing that a hydrophobic surface was dominative in its CR3 domain [6].

So far we have proved that the binding energy is positively correlated to the molecule weight and the number of aromatic atoms, which indicates the positive correlation between binding energy with compound's size. Does this mean the molecule with larger size is better for E7 imprinting? The answer is no. It's the total binding energy of all assembling molecules, rather the binding energy of a single molecule that indeed determines the recognition ability. Bigger size also means less assembling molecules. It's not necessary for the binding energy of a single

molecule to be large to ensure large total assembling binding energy. What are the criteria to pick out the best imprinting molecule? We will discuss the criteria in the following sections.

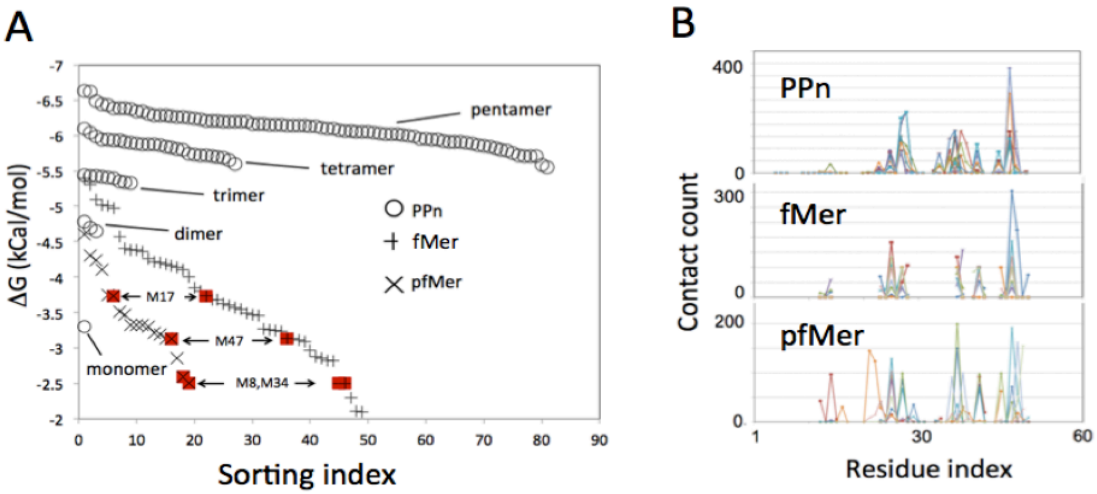

Figure 5.3 Comparison of docking on 2EWL.
The docking was performed with AutoDock Vina. (A) Binding energy of the 189 compounds. Libraries: PPn, phenolic oligomer; fMer, traditional functional monomer; pfMer, functional monomer for protein. The compounds in each library were sorted according to the binding energy and indexed. The red marked compounds were found in both fMer and pfMer libraries and indicated as internal control of docking. (B) Contact maps of the compounds including (top) PPn: 3 dimers and 9 trimers; (middle) fMer, (bottom) pfMer: top 10 ranked compounds in each library.

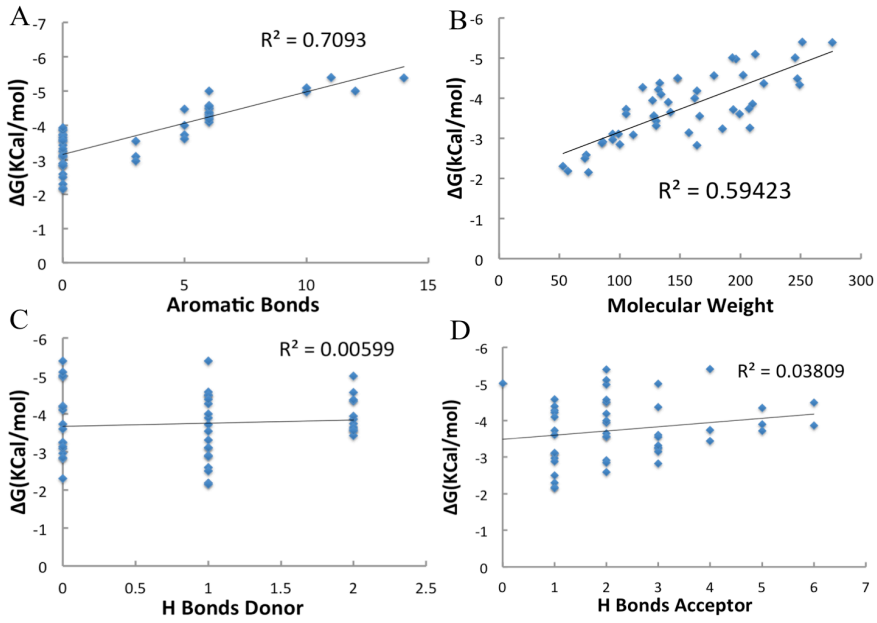

Figure 5.4 Correlation of binding energy of the fMers to the characteristics of the E7 protein.

5.5 Criteria for screening compounds with docking

It was known that small chemical compounds like urea denatured proteins due to the formation of strong hydrogen bonds with the residues [7]. Such an issue was also investigated in the docking study of fMer screening by GOLD [8]. So compounds either neutral or weak acidic or basic with relatively low binding energy was the rule-of-thumb to choose polymers for protein imprinting [2], just as shown clearly in Figure 5.2A. To our understanding, the compounds with interactions that exerted only at very few contacts should be screen out of the fMer candidates. In this regard, the binding energy averaged over contact might be important to inspect the compounds. The "binding energy per contact", i.e. ΔG/contact, were plotted versus ΔG in Figure A. The values of ΔG/contact were distributed between -0.3 to -1.2 kCal/mol. Some compounds had very high values meaning that their binding energy was mainly provided by few contacts. Of note, phenolic monomer, dimers, and trimers showed a similar level of average binding energy

closely positioned around -0.6 kCal/mol, although their values of total binding energy ΔG were clearly differentiated into three groups due to the different numbers of benzene ring. In contrast, the values of average binding energy of fMer and pfMer fell in much wider ranges. Some compounds with high ΔG and low average binding energy were highlighted in a red box. In this paper, the size of the box was chosen to include 10 phenolic oligomers, 9 fMers and 3 pfMer. In general, the selection actually represented a subpopulation of the fMer with distinctive characteristics. As shown in Figure 5.5B an C, the molecular weight and H-bond acceptor of the selected fMer compounds had reversed contributions to the average binding energy comparing to the entire library of fMer. Their k values were changed from -8.5e-4 to 1.4e-3 kCal/mol and -1.1e-2 to 5.2e-2 kCal/mol respectively. In this group of compounds, H-bond acceptor might only linearly increase the amount of contact without formation of H-bond to significantly increase the binding energy. On the other hand, the contribution by the aromatic carbon showed in Figure 5.5D was more intensified in the selected compounds considering k changing from -1.3e-2 of the entire fMer library to -2.1e-2 kCal/mol. All of them had at least 6 aromatic carbons. It thus far suggested the selection of aromatic rings for the hydrophobic interaction with the E7 protein.

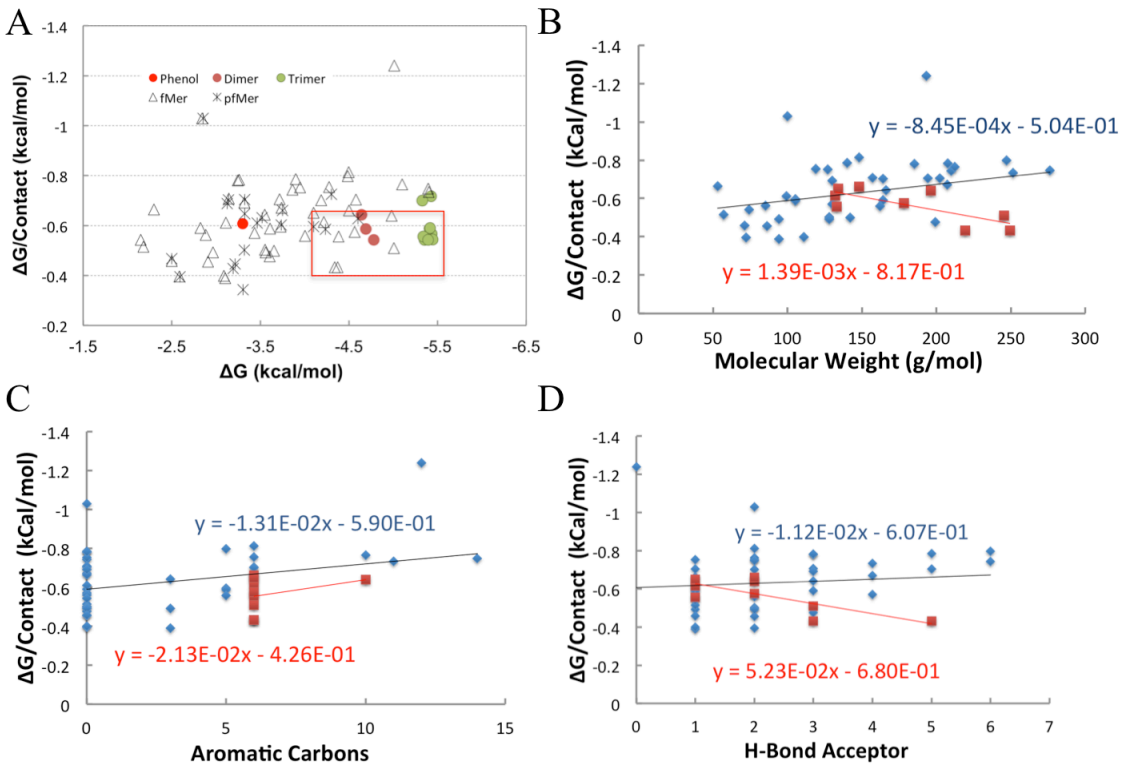

Figure 5.5 A subpopulation of the compounds selected based on binding energy and average binding energy.
(A) Scatter chart of ΔG/Contact vs. ΔG of the fMer, pfMer and phenolic monomer, dimer and trimer. Red box: the selection of compounds. The box size by arbitrary assigned range of ΔG (-4.0 to -5.5 kCal/mol) and ΔG/Contact (-0.4 to -0.7 kCal/mol). (B), (C) and (D) the subpopulation of selected fMer (red) outlined by the average binding energy ΔG/Contact depending on Molecular weight, H-Bond Acceptor and Aromatic Carbon respectively within the entire library of fMer (blue). The fitting of the data point were given as $y=kx+b$.

5.6 Prediction of interfacing with the compounds

In spite of the common aspects shared by the selected subpopulation of compounds, each individual compound did have distinctive docking details. As shown in Figure 5.6, two selected compounds, one from the fMer library and another from phenolic oligomers, were docked with their highest scored poses. The contact map was obtained from 100 runs of docking of each compound. The indicated interfaces were mostly composed of hydrophobic residues. The 4-

Phenoxyphenol, for example, was confined by three hydrophobic residues Leu37, Phe41 and Phe47 at the benzene end, and a hydrophobic residue Val27 at the middle benzene. Although a hydrogen bond was indicated by the software between the phenolic dimer's hydroxyl group and the nitrogen atom in Glu28, it was skeptical that this contact might be lost when a flexible protein structure was used, for example, in the molecular dynamics simulation. The structure, binding energy, average binding energy and the interface residues of all the selected compounds were summarized in Table 5.1. An interface residue was extracted if the amount of contact on this residue was more than 8% of the total on E7. The residue information of the binding energy and interface may provide guidance to the fabrication of imprint with designated requirements of affinity and binding sites. With a group of choices of such rational screened compounds, it will be more feasible to get few compatible ones into a polymerization system to fabricate the high-performance imprint with multiple recognition features.

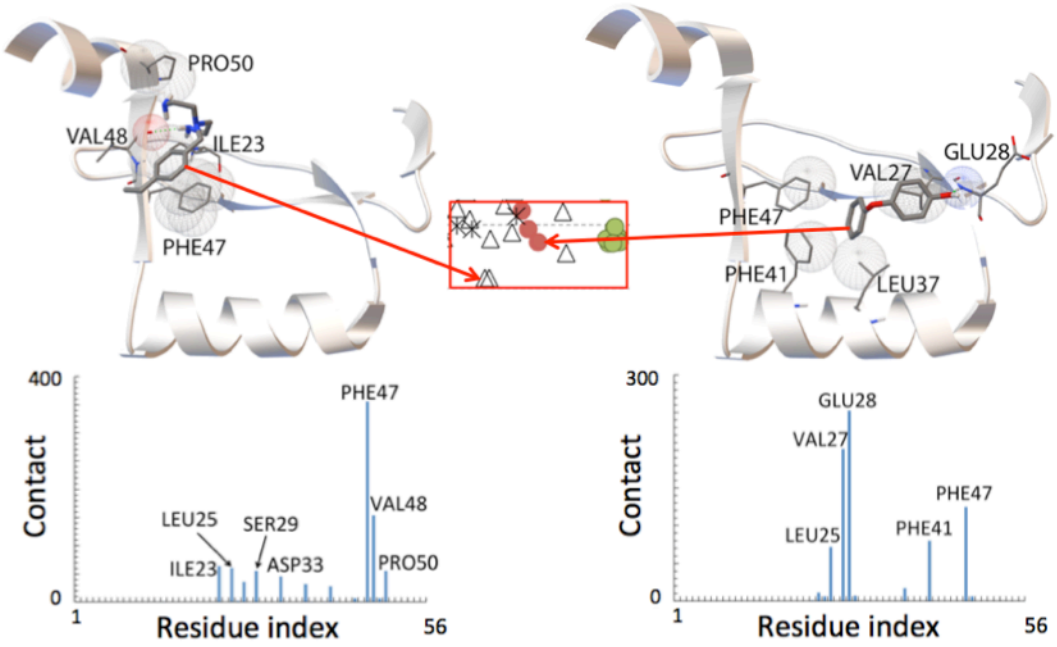

Figure 5.6 Docking details of a fMer (N'-(2-aminoethyl)-N'-[8]ethane-1,2-diamine, and a phenolic dimer (4-phenoxylphenol) on the E7 protein. Inset box: the selection outlined in Figure 5.5(A). The van der Waal distance was outlined on the residue atoms to indicate the contacts. The N and O atoms were shown in blue and red respectively. The contact count was accumulated from 100 runs of docking.

Table 5.1 The characteristics of the selected compounds.
Interface: residues marked in red. It represents more than 8% of the total contacts happened on the residue

Name	Structure	ΔG(kCal/mol)	ΔG/contact (kCal/mol)	Interface
N-(4-vinylbenzyl)im-inodiacetic acid	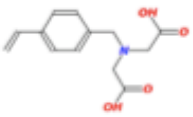	-4.34	-0.43	1 10 20 30 GSHMAEPQRHKILCVCCKCDGRIELTVESS 31 40 50 56 AEDLRTLQQLFLSTLSFVCPWCATNQ
1-[(4-vinylphenyl)-methyl]-1,4,7-triazacyclononane	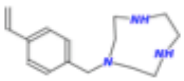	-5.01	-0.51	1 10 20 30 GSHMAEPQRHKILCVCCKCDGRIELTVESS 31 40 50 56 AEDLRTLQQLFLSTLSFVCPWCATNQ
4-vinyl-4'-methyl-2,2'-bipyridine	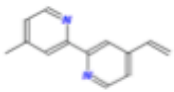	-4.98	-0.64	1 10 20 30 GSHMAEPQRHKILCVCCKCDGRIELTVESS 31 40 50 56 AEDLRTLQQLFLSTLSFVCPWCATNQ
4-(N-vinylbenzyl)diethyl-enetriamine	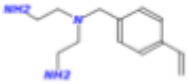	-4.37	-0.43	1 10 20 30 GSHMAEPQRHKILCVCCKCDGRIELTVESS 31 40 50 56 AEDLRTLQQLFLSTLSFVCPWCATNQ
4-vinylbenzoicacid	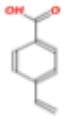	-4.50	-0.66	1 10 20 30 GSHMAEPQRHKILCVCCKCDGRIELTVESS 31 40 50 56 AEDLRTLQQLFLSTLSFVCPWCATNQ
4-vinylbenzylamine	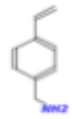	-4.38	-0.56	1 10 20 30 GSHMAEPQRHKILCVCCKCDGRIELTVESS 31 40 50 56 AEDLRTLQQLFLSTLSFVCPWCATNQ
4-vinylbenzaldehyde	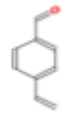	-4.21	-0.61	1 10 20 30 GSHMAEPQRHKILCVCCKCDGRIELTVESS 31 40 50 56 AEDLRTLQQLFLSTLSFVCPWCATNQ
4-Methoxystyrene	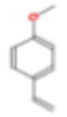	-4.10	-0.65	1 10 20 30 GSHMAEPQRHKILCVCCKCDGRIELTVESS 31 40 50 56 AEDLRTLQQLFLSTLSFVCPWCATNQ
2-(4-vinylphenyl)-1,3-propanediol	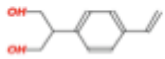	-4.56	-0.57	1 10 20 30 GSHMAEPQRHKILCVCCKCDGRIELTVESS 31 40 50 56 AEDLRTLQQLFLSTLSFVCPWCATNQ
divinylbenzene		-4.60	-0.63	1 10 20 30 GSHMAEPQRHKILCVCCKCDGRIELTVESS 31 40 50 56 AEDLRTLQQLFLSTLSFVCPWCATNQ
N-benzylacrylamide	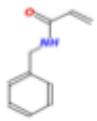	-4.23	-0.58	1 10 20 30 GSHMAEPQRHKILCVCCKCDGRIELTVESS 31 40 50 56 AEDLRTLQQLFLSTLSFVCPWCATNQ

Table 5.1 The characteristics of the selected compounds (continue).
Interface: residues marked in red. It represents more than 8% of the total contacts happened on the residue

Name	Structure	ΔG(kCal/mol)	ΔG/contact (kCal/mol)	Interface
styrene		-4.10	-0.60	1 10 20 30 GSHMAEPQRHKILCVCCKCDGRIELTVESS 31 40 50 56 AEDLRTLQQLFLSTLSFVCPWCATNQ
2-phenoxyphenol	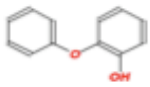	-4.64	-0.64	1 10 20 30 GSHMAEPQRHKILCVCCKCDGRIELTVESS 31 40 50 56 AEDLRTLQQLFLSTLSFVCPWCATNQ
3-phenoxyphenol	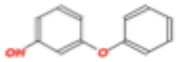	-4.69	-0.59	1 10 20 30 GSHMAEPQRHKILCVCCKCDGRIELTVESS 31 40 50 56 AEDLRTLQQLFLSTLSFVCPWCATNQ
4-phenoxyphenol	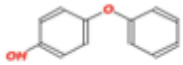	-4.78	-0.54	1 10 20 30 GSHMAEPQRHKILCVCCKCDGRIELTVESS 31 40 50 56 AEDLRTLQQLFLSTLSFVCPWCATNQ
2-(4-phenoxy-phenoxy)phenol	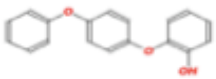	-5.43	-0.57	1 10 20 30 GSHMAEPQRHKILCVCCKCDGRIELTVESS 31 40 50 56 AEDLRTLQQLFLSTLSFVCPWCATNQ
3-(2-phenoxy-phenoxy)phenol	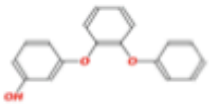	-5.35	-0.54	1 10 20 30 GSHMAEPQRHKILCVCCKCDGRIELTVESS 31 40 50 56 AEDLRTLQQLFLSTLSFVCPWCATNQ
3-(3-phenoxy-phenoxy)phenol	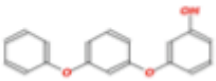	-5.41	-0.59	1 10 20 30 GSHMAEPQRHKILCVCCKCDGRIELTVESS 31 40 50 56 AEDLRTLQQLFLSTLSFVCPWCATNQ
3-(4-phenoxy-phenoxy)phenol	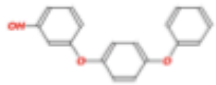	-5.34	-0.56	1 10 20 30 GSHMAEPQRHKILCVCCKCDGRIELTVESS 31 40 50 56 AEDLRTLQQLFLSTLSFVCPWCATNQ
4-(2-phenoxy-phenoxy)phenol	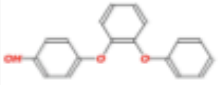	-5.45	-0.54	1 10 20 30 GSHMAEPQRHKILCVCCKCDGRIELTVESS 31 40 50 56 AEDLRTLQQLFLSTLSFVCPWCATNQ
4-(3-phenoxy-phenoxy)phenol	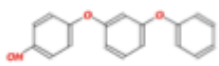	-5.41	-0.59	1 10 20 30 GSHMAEPQRHKILCVCCKCDGRIELTVESS 31 40 50 56 AEDLRTLQQLFLSTLSFVCPWCATNQ
4-(4-phenoxy-phenoxy)phenol	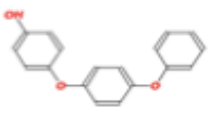	-5.39	-0.54	1 10 20 30 GSHMAEPQRHKILCVCCKCDGRIELTVESS 31 40 50 56 AEDLRTLQQLFLSTLSFVCPWCATNQ

5.7 Conclusions

A theoretical approach utilizing molecular dynamics and docking analysis can be used to efficiently examine the imprinting compounds from a chemical library by the computation of molecular interactions. For imprinting the E7 protein, the phenolic compounds produced in the electropolymerization process on the nanosensor have meritorious properties to facilitate the imprint performance. A subpopulation of compounds can also be efficiently selected from a lot of chemicals by applying the requirement of binding energy. Similar to the PPn compounds, those molecules can be the candidates to conduct rational design of imprint regarding their distinctiveness of the binding energy and binding interfaces. The average binding energy, i.e. ΔG/contact, could be a novel parameter added to the general rule for evaluating the functional compounds of protein imprint.

5.8 References

1. Yan, M., *Molecularly Imprinted Materials: Science and Technology*. 2004: CRC press.

2. Whitcombe, M.J., I. Chianella, L. Larcombe, S.A. Piletsky, J. Noble, R. Porter, and A. Horgan, *The Rational Development of Molecularly Imprinted Polymer-Based Sensors for Protein Detection.* Chemical Society Reviews, 2011. **40**(3): p. 1547-1571.

3. O'Boyle, N.M., M. Banck, C.A. James, C. Morley, T. Vandermeersch, and G.R. Hutchison, *Open Babel: An Open Chemical Toolbox.* Journal of Cheminformatics, 2011. **3**(1): p. 33.

4. Morris, G.M., R. Huey, W. Lindstrom, M.F. Sanner, R.K. Belew, D.S. Goodsell, and A.J. Olson, *Autodock4 and Autodocktools4: Automated Docking with Selective Receptor Flexibility.* Journal of Computational Chemistry, 2009. **30**(16): p. 2785-2791.

5. Trott, O. and A.J. Olson, *Autodock Vina: Improving the Speed and Accuracy of Docking with a New Scoring Function, Efficient Optimization, and Multithreading.* Journal of Computational Chemistry, 2010. **31**(2): p. 455-461.

6. Ohlenschläger, O., T. Seiboth, H. Zengerling, L. Briese, A. Marchanka, R. Ramachandran, M. Baum, M. Korbas, W. Meyer-Klaucke, and M. Dürst, *Solution*

Structure of the Partially Folded High-Risk Human Papilloma Virus 45 Oncoprotein E7. Oncogene, 2006. **25**(44): p. 5953-5959.

7. Bennion, B.J. and V. Daggett, *The Molecular Basis for the Chemical Denaturation of Proteins by Urea.* Proceedings of the National Academy of Sciences, 2003. **100**(9): p. 5142-5147.

8. Kryscio, D.R., Y. Shi, P. Ren, and N.A. Peppas, *Molecular Docking Simulations for Macromolecularly Imprinted Polymers.* Industrial & Engineering Chemistry Research, 2011. **50**(24): p. 13877-13884.

Chapter 6 Summary

Carbon-based nanomaterials have promising applications spanning areas from the oil industry to healthcare due to their special attributes to interface with molecules in their local environments. The investigation on nano-interfaces can open in-depth visions of chemical, physical and biological mechanisms that mediate the functions of the nanodevices designed for drug delivery, biodetection, etc. To study properties of the surface at nanoscales poses challenges to current detection techniques, such as infrared absorption spectroscopy (IR) and transmission electron microscopy (TEM). They are either not appropriate for detecting materials in aqueous environments or lack of ability to resolve dynamics at the interface with a sufficient temporal recording rate. The computation technology fueled by the latest progress in software and hardware has shown capabilities to accurately simulate molecular binding processes in biophysics for instance.

In this study, we seek the power of molecular dynamics simulation and computational docking to analyze the dynamics at various nano-interfaces including graphene amphiphilic Janus nanosheet (AJN), carbon nanotubes (CNTs), and CNT array biosensor. Rational design of the functional interface is explored by comparison of experimental results and the theoretical predictions.

In the study of AJN, we discovered (1) a facile, cheap, and scalable synthesis method of AJN with graphene oxide and tapioca starch, and (2) an additive poly (sodium 4-styrenesulfonate) (PSS) that improves the stability of AJN in brine.

Regarding the study of biocompatibility and biodegradation mechanism of CNTs, we found that immunoglobulin G (IgG) was susceptible to bind with CNTs that could contribute to reduce CNTs' cytotoxicity and accelerate their biodegradation.

In the biorecognition study, we identified an array of phenolic oligomers with different polymerization structures could facilitate the interaction with the protein template and self-assemble to form recognition interfaces. By establishing a cascading molecular dynamics and docking analysis, a preliminary protocol of rational design for protein imprinting was proposed and had shown an efficient screening of a chemical library.

This study provides opportunities to understand molecular interactions on the interface in atomistic details, and demonstrates the combination of molecular dynamics simulation and docking is an effective approach for the development of novel nanomaterials and nanosensors.